

THÈSE

PRÉSENTÉE A

L'UNIVERSITÉ BORDEAUX 1

ÉCOLE DOCTORALE DES SCIENCES physiques et de l'Ingénieur

Par Delphine ELBES

POUR OBTENIR LE GRADE DE

DOCTEUR

SPÉCIALITÉ : Lasers, Matière, Nanosciences

THERMOTHERAPIES PAR ULTRASONS FOCALISES ET RADIOFREQUENCES GUIDÉES PAR IMAGERIE DE RESONANCE MAGNETIQUE

**Développements méthodologiques pour le traitement du cancer du foie et des arythmies
cardiaques**

Soutenue le : 18 décembre 2012

Devant la commission d'examen formée de :

M. Jean-François Aubry,
Mme Monique Bernard,
M. Bertrand Audoin,
M. Roger Marthan ,
M. Jean-Michel Franconi,

Chargé de Recherche CNRS,
Directrice de Recherche CNRS,
Professeur Bordeaux 1,
PU-PH Université Bordeaux 2,
Professeur Bordeaux 2,

Rapporteur
Rapporteur
Examineur
Examineur
Examineur

M. Bruno Quesson,

Chargé de Recherche CNRS

Directeur de thèse

Remerciements

Comme tous les docteurs le savent, la thèse est une longue aventure, avec ses moments de joie quand la première manip réussit et ses moments de doute. Heureusement, la plupart du temps ils sont partagés, et je tiens à exprimer toute ma gratitude à ceux qui m'ont accompagnée durant ces trois années de thèse.

Je tiens tout d'abord à remercier Chrit Moonen pour m'avoir permis de commencer ma thèse au laboratoire IMF, bien que ce laboratoire n'existe plus aujourd'hui.

J'aimerais remercier Roger Marthan pour m'avoir accueilli au milieu de ma thèse, dans son laboratoire, le centre de recherche Cardio-thoracique de Bordeaux, et Michel Haïssaguerre pour m'avoir accueilli au sein de son équipe.

Je tiens également à témoigner toute ma gratitude à Jean-François Aubry, Monique Bernard, Bertrand Audouin, Roger Marthan et Jean-Michel Franconi qui m'ont fait l'honneur de constituer mon jury de thèse, et particulièrement Jean-François Aubry et Monique Bernard pour avoir accepté d'être rapporteurs de ma thèse. Je tiens également à remercier Bertrand Audouin, directeur de mon école doctorale, pour la médiation qu'il a menée lors de mon changement de laboratoire.

J'aimerais aussi remercier celui qui m'a suivie et encadrée durant ces trois années, mon directeur de thèse Bruno Quesson. Nos discussions m'ont permis de tenir le cap et d'aller au bout de cette aventure.

Je souhaiterais aussi remercier ceux qui étaient présent lors de mes premiers pas dans la recherche à l'IMF : Marc, Karine, Cyril (mes 'co-thésards'), Pierre, Sébastien, Silke,

Yasmina, Marie-France, Baudoin, Anna, Franck, Pierre Yves (Pyf), Coralie, Dimitri, Colette, Charles, Matthieu, Mario.

Et plus particulièrement, à Marc pour nos fous rires lors des manip, à Karine pour m'avoir fait découvrir les cappuccinos du RU, à Pierre qui n'est plus parmi nous et qui m'a montré la première fois comment me servir de l'IRM, à la PyfRou team pour leurs animations, à Charles ('le bucheron de Toronto') qui m'a appris à travailler à l'atelier, à Matthieu et Marie France qui ont été un soutien.

Je souhaiterais remercier ceux qui m'ont soutenus dans la deuxième partie de ma thèse : Delphine, Isabelle, Sébastien, Delphine pour les manip, Olivier, Philippe, Véronique, Ed, Rémi, Thomas merci de m'avoir écoutée un dimanche matin et de m'avoir conseillée, les post-docs : David, Rick, Fanny, Steve, Guillaume, Dominique, les ingénieurs et techniciens: Mathilde, Sébastien, Pierre et Marion, les doctorants : Mathilde, Aurélie et Virginie.

Des remerciements particuliers pour Mathilde et Aurélie 'mes co-thésardes', aussi appelées 'tic et tac', pour leur indéfectible soutien, surtout pendant la rédaction de ce manuscrit, merci de votre présence le week-end, de votre bonne humeur, de vos fous rires, de vos mikados et schoko-bons en tout genre, et de cette partie de Quidditch mémorable qui restera gravée dans ma mémoire.

Je remercie tout particulièrement ma mère, Marie-Odile, pour m'avoir toujours soutenue au cours de ces huit années d'études universitaires et d'avoir été présente dans les moments les plus difficiles.

Je voudrai exprimer mon immense gratitude à celui qui partage ma vie depuis bientôt dix ans, Nicolas. Ton amour, ton soutien, ta chaleur, ta générosité est ce qui m'a permis de me surpasser, de croire en mes rêves. Merci pour le bonheur que tu m'apportes chaque jour.

A mon amour,

A ma mère.

Résumé

La thèse s'articule autour du développement des thérapies hépatique et cardiaque guidées par Imagerie de Résonance Magnétique (IRM).

La première partie est axée sur le développement d'une méthode permettant d'augmenter la taille des lésions induites par ultrasons focalisés de haute intensité (HIFU). Le seuil de d'intensité acoustique fut déterminé par IRM de la force de radiation acoustique et l'effet caractérisé par IRM de température *ex vivo* et *in vivo* dans le foie de porc.

La deuxième partie présente le développement d'une méthode permettant une focalisation HIFU hépatique intercostale avec utilisation de la déflexion électronique du faisceau pour le suivi du mouvement respiratoire ou /et une ablation multipoint. La méthode proposée repose sur une mise à jour des éléments du transducteur HIFU à désactiver en fonction du point de focalisation sélectionné, à partir d'une projection géométrique de l'ombre des côtes sur la surface du transducteur, mesurée sur des images IRM anatomiques. Nous avons montré qu'il est possible de réduire significativement le chauffage des côtes tout en conservant une élévation de température dans le foie suffisante pour induire une lésion thermique.

La troisième partie expose la mise en place de l'IRM de température pour le monitoring des ablations par radiofréquences (RF) dans le cœur. Plusieurs aspects sont abordés, notamment la précision de la thermométrie, la possibilité de réaliser des ablations thermiques par cathéter RF sous IRM de température *in vivo* dans le cœur de brebis, ainsi que l'utilisation du cathéter comme sonde d'imagerie dans l'objectif d'accroître la précision de la thermométrie cardiaque.

Magnetic Resonance Imaging guided focused ultrasound and radiofrequency ablations.

Methodological developments for the treatment of liver cancer and cardiac arrhythmias

Abstract

My manuscript studies the development of mini and non invasive thermotherapies guided by magnetic resonance imaging (MRI) in the treatment of hepatic and cardiac diseases.

The first part was the development of a method to increase the lesion size, induced by HIFU, and based on bubble enhanced heating (BEH). The acoustic power threshold of the BEH was determined by MR acoustic radiation force imaging (MR-ARFI) and the thermal effect was characterized by MR thermometry on *ex vivo* and *in vivo* in pig livers.

The second part developed a strategy to perform HIFU through the rib cage using beam steering to track the respiratory movement or to performed multipoint ablation while avoiding heating of ribs. Transducer elements localized in the geometric projection of the shadow of ribs, relatively to the targeted focal point, were switched off.

The third part was the development of the MR thermometry on the heart for the monitoring of radiofrequency ablation (RFA). Several aspects were investigated, in particular the thermometry precision, the feasibility to perform catheter radiofrequency ablation under MR thermometry *in vivo* in a sheep heart, the possibility to use the catheter as an MR antenna to increase spatial resolution of MR thermometry images.

Résumé substantiel

Dans les pays occidentaux, le cancer et les maladies cardiovasculaires représentent les principales causes de décès (respectivement 30% vs. 28%). Parmi l'arsenal thérapeutique disponible, les méthodes de destruction thermique par la température (thermothérapie) sont de plus en plus utilisées. Différentes techniques (radiofréquences, laser, radiofréquences, ultrasons focalisés) sont utilisées pour induire une élévation de température suffisante permettant de déposer une dose thermique (intégrant temps d'exposition et température atteinte) létale dans la région pathologique ciblée pour induire une nécrose de coagulation. Les thermothérapies sont une alternative avantageuse à la radiothérapie car elles offrent la possibilité de répéter le traitement plusieurs fois sans effet de dose cumulée pour les tissus sains. Elles sont largement utilisées dans le traitement curatif du cancer du foie (ablation par radiofréquences), des fibromes utérins (ultrasons focalisés), de la prostate, du sein, etc...

La thermométrie par Imagerie de Résonance Magnétique permet de cartographier en temps réel et de manière non invasive la distribution spatiale de la température tissulaire pendant le traitement. Cette méthode d'imagerie permet de planifier précisément la zone à traiter, de suivre l'évolution de la température dans les régions pathologiques et saines, de contrôler précisément le dépôt de chaleur local (boucles d'asservissement contrôlé par thermométrie IRM) et de cartographier la dose thermique cumulée pour prédire la lésion thermique induite. L'association des méthodes de thermothérapie et d'IRM de température permet donc d'offrir une meilleure fiabilité du traitement, de sécuriser la procédure et de contrôler précisément la lésion induite.

La première partie du travail de thèse est consacrée au le développement d'une méthode d'ablation thermique par ultrasons focalisés de haute intensité (HIFU) non invasifs, dans le but de générer de larges lésions thermiques pour le traitement des tumeurs dans le foie. Cette technique, basée sur la création de bulles au niveau du point focal, présente

l'avantage d'augmenter l'efficacité de chauffage, de générer une forme de lésion quasi sphérique (ellipsoïde en absence de bulles), de protéger les structures (organes, tissus sains, peau, os) localisées en champ lointain (i.e. après le point focal). Les objectifs de cette étude *ex vivo* et *in vivo* dans le foie de porc sont 1) de déterminer le seuil en puissance acoustique pour induire ce phénomène 2) de comparer, sous IRM de température en temps réel, la distribution et les profils de température obtenus avec et sans bulles au point focal.

Dans un premier temps, l'IRM de température a permis l'observation *in vivo* du changement de la position de la valeur maximale de température (vers le transducteur) en présence de bulles, et a été utilisée pour déterminer la puissance acoustique nécessaire pour la génération de ce phénomène grâce à l'application de tirs ultrasonores (0,5 s) dont la puissance acoustique fut progressivement augmentée entre 400 et 800W. Ensuite, deux protocoles de tirs ultrasonores ont été comparés à même énergie (1800J). Le premier (« groupe control ») correspond à un tir de 15 s à puissance modérée (120W). le second (« groupe expérimental») est composé d'une impulsion de courte durée (0,5 s) à une puissance acoustique suffisante pour créer les bulles (400-800 W), immédiatement suivie d'une impulsion continue (14,5 s) dont la puissance est ajustée pour atteindre une énergie cumulée de 1800J. Pour des régions de focalisation des ultrasons localisées à une profondeur comprise entre 20 et 25 mm dans le foie de porc *in vivo*, 600 à 800 W ont été nécessaires pour atteindre le seuil de création des bulles. La distribution en température du groupe expérimental a montré une distribution quasi sphérique de la température (en forme de goutte), décalée vers le transducteur de $7 \pm 3,3$ mm et présentant un gain de 40% pour le maximum d'élévation de température comparé au groupe control (distribution de la température en ellipsoïde de révolution).

Une seconde étude présente l'utilisation de l'imagerie par IRM de la force de radiation acoustique (MR-ARFI) avec comme objectif d'affiner la détermination du seuil de création des bulles dans le foie de porc *ex vivo* sans générer de chauffage. L'augmentation progressive

de la puissance acoustique a mis en évidence un seuil de création des bulles correspondant à un déplacement local de 50 μm d'amplitude. Des courbes de calibration du déplacement en fonction de la puissance acoustique ont été réalisées à basse puissance et ont permis, compte tenu de la linéarité déplacement puissance acoustique, de prédire la puissance nécessaire pour atteindre le seuil d'amplitude de déplacement tissulaire permettant la de génération de bulles. Par la suite, deux chauffages identiques ont été comparés (20W, 30s), de manière analogue à ce qui a été développé dans la première étude, l'un étant précédé par une impulsion de courte durée (0,5s) à une puissance acoustique suffisante pour créer des bulles *in situ*. En présence de bulles, pour les deux modalités d'observation (température, déplacement) la distribution du point focal était en forme de goutte et décalé d'environ 4 mm vers le transducteur, le gain du maximum de température et de déplacement ont été de 1,5 et 2 respectivement, pour la largeur à mi-hauteur de 1,7 et 2,2 respectivement, par rapport aux expériences témoins réalisées en absence de bulles. La méthode MR-ARFI semble donc très prometteuse pour accroître la sécurité des traitements par HIFU, en visualisant la région focale avant chauffage, et pourrait être un outil intéressant dans l'exploitation des chauffages potentialisés par les bulles.

La deuxième partie présente une méthode pour éviter les dommages thermiques au niveau des côtes occasionnées lors de traitements par HIFU d'organes situés dans la cage thoracique. La méthode proposée repose sur une projection géométrique, du point de vue du point focal, de l'ombre des côtes sur le transducteur permettant ainsi d'éteindre les éléments du transducteur (système matriciel à 256 éléments distribués sur la surface active du transducteur ultrasonore) participant le plus au chauffage engendré. La faisabilité de cette méthode a déjà été démontrée *in vivo* pour un tir ultrasonore réalisé à la focale naturelle. L'innovation de cette partie a été de combiner cette méthode avec l'utilisation de la déflexion électronique du faisceau ultrasonore, technique permettant de déplacer électroniquement le

point focal pour effectuer différentes trajectoires de tir ultrasonores et/ou de suivre une cible mobile comme le cœur ou le foie. Les expériences réalisées sur du gel avec une inclusion osseuse ont montré, pour une focalisation à +/- 7 mm de la focale naturelle horizontalement, qu'en l'absence d'une actualisation de l'ombre portée de la côte sur la surface du transducteur, qu'un chauffage non négligeable était induit au niveau des côtes (17°C), et que l'élévation de température au point focal était significativement réduite (30°C → 19°C). La mise à jour de la surface active du transducteur par une désactivation des éléments du transducteur localisés dans l'ombre des côtes a permis de maintenir une élévation de température au point focal de l'ordre de 30°C et de la réduire au niveau des côtes (7°C à 9°C). Cette étude a montré que l'utilisation de la déflexion électronique (dans l'ordre de grandeur du mouvement respiratoire, 14 mm) nécessite une mise à jour de la surface active du transducteur. La simplicité de cette méthode, qui ne requière que l'acquisition préalable d'une pile d'images anatomiques, ouvre l'opportunité d'une implémentation rapide en temps réel, qui pourrait améliorer la sécurité et l'efficacité de la procédure pour l'ablation intercostale des tissus pathologiques hépatiques et cardiaques..

La troisième partie expose la mise en place de l'IRM de température pour le monitoring des ablations par radiofréquences (RF) dans le cœur. Dans un premier temps, une mesure du T2* du cœur a été réalisée afin d'estimer la précision de la thermométrie, puisque ce paramètre intervient directement sur le rapport signal sur bruit des images obtenues en écho de gradient rapide. Cette mesure a été réalisée sur 10 volontaires sains en utilisant une séquence en écho de gradient segmentée, sous apnée et synchronisée sur le rythme cardiaque. La valeur moyenne du T2* mesurée est 40,2 ms, en accord avec les données rapportées dans la littérature. Cette mesure a permis de réaliser une estimation de la précision de la température ($\sigma = 1,26^\circ\text{C}$) très proche de celle mesurée directement sur les images de température cardiaque ($\sigma = 1,5^\circ\text{C}$). Cette précision est jugée suffisante pour réaliser des

ablations radiofréquences dans le cœur sous thermométrie. Le premier test de monitoring temps réel des ablations RF a été réalisé dans un gel d'agar dopé au NaCl pour permettre le passage du courant électrique. Les résultats ont montré qu'il était possible de visualiser une élévation de température au cours du temps avec une précision suffisante pour différencier un chauffage effectué avec un cathéter avec et sans irrigation interne. La possibilité de réaliser des ablations thermiques par cathéter RF (10W, 60s) sous IRM de température sur le cœur de brebis *in vivo* a ensuite été démontrée. De plus, la bonne précision sur la mesure de température pourrait permettre d'obtenir une résolution plus fine. Néanmoins, compte tenu de l'épaisseur minimale du myocarde ~ 2 mm et de la résolution maximale actuelle $2 \times 2 \times 5$ mm³, il apparaît nécessaire de réduire la taille des pixels de l'image de température afin de mieux caractériser le chauffage induit par ablation RF et ainsi de mieux prédire la lésion résultante. L'utilisation du cathéter d'ablation lui-même comme sonde d'imagerie pourrait permettre d'accroître la résolution spatiale dans la limite des gradients de champ magnétique disponibles sur l'IRM clinique installée au sein de l'Institut hospitalo-universitaire LIRYC et permettre d'obtenir une cartographie submillimétrique de la température tissulaire. La faisabilité d'imager avec le cathéter est montrée dans la dernière partie sur une IRM opérant 4,7 Tesla et a permis d'obtenir une résolution spatiale de $0,6 \times 0,6 \times 5$ mm³.

Les études présentées dans ce manuscrit proposent de nouvelles méthodes dans le cadre des ablations thermiques guidées par IRM pour le traitement non invasif par HIFU ou mini-invasif par ablation radiofréquences. Différentes stratégies ont été développées afin d'améliorer la sécurité et l'efficacité des ablations thermique, incluant l'étude du chauffage stimulé par les bulles sous IRM de température en vue d'accroître la taille des lésion thermique dans le foie par HIFU, le développement d'une méthode réduisant les dommages sur les côtes dans le cadre de l'utilisation des HIFU à travers la cage thoracique, et enfin la mise en place de l'IRM de température pour améliorer le traitement des ablation

radiofréquence dans le cœur. Les développements effectués dans cette thèse ont pour vocation à être valorisés en application clinique, dans une démarche de recherche translationnelle, à l'interface entre la physique de l'IRM, l'instrumentation, le traitement d'images et les applications précliniques et cliniques.

| | | |
|-------------|--|-----------|
| I. | INTRODUCTION..... | 4 |
| 1. | MR THERMOMETRY..... | 5 |
| 2. | THERMAL DOSE..... | 6 |
| 3. | REFERENCES..... | 7 |
| II. | MR GUIDED HIFU ON THE LIVER..... | 11 |
| 1. | MAGNETIC RESONANCE IMAGING FOR THE EXPLOITATION OF BUBBLE ENHANCED HEATING BY HIGH INTENSITY FOCUSED ULTRASOUND. A FEASIBILITY STUDY IN EX VIVO LIVER..... | 11 |
| 1. | <i>Abstract</i> | 11 |
| 2. | <i>Introduction</i> | 13 |
| 3. | <i>Material and Methods</i> | 15 |
| 4. | <i>Results</i> | 19 |
| 5. | <i>Discussion</i> | 28 |
| 6. | <i>References</i> | 31 |
| 2. | A PRECLINICAL STUDY OF IN VIVO MR-GUIDED ENHANCED ULTRASOUND HEATING IN PIG LIVER | 35 |
| 1. | <i>Abstract</i> | 35 |
| 2. | <i>Introduction</i> | 36 |
| 3. | <i>Material and methods</i> | 38 |
| 4. | <i>Results</i> | 42 |
| 5. | <i>Discussion</i> | 52 |
| 6. | <i>References</i> | 55 |
| III. | TRANSCOSTAL HIFU | 60 |
| 1. | INTRODUCTION..... | 60 |
| 2. | MATERIAL AND METHODS..... | 64 |
| 3. | RESULTS | 67 |

| | | |
|------------|--|-----------|
| 4. | DISCUSSION | 72 |
| 5. | REFERENCES..... | 74 |
| IV. | INTERVENTIONAL CARDIOLOGY | 77 |
| 1. | INTRODUCTION..... | 77 |
| 2. | CONVENTIONAL IMAGING PLANS IN CARDIAC MRI..... | 79 |
| 3. | T2* MEASUREMENT <i>IN VIVO</i> IN THE HUMAN HEART | 82 |
| 1. | <i>Introduction</i> | 82 |
| 2. | <i>Methods and results</i> | 87 |
| 3. | <i>Discussion</i> | 93 |
| 4. | TEMPERATURE PRECISION | 94 |
| 1. | <i>Estimation of the standard deviation of the temperature</i> | 94 |
| 2. | <i>Discussion</i> | 97 |
| 5. | RADIOFREQUENCY THERMAL ABLATION UNDER MR THERMOMETRY: PRELIMINARY EXPERIMENTS | 99 |
| 1. | <i>Introduction</i> | 99 |
| 2. | <i>Material method</i> | 100 |
| 3. | <i>Results</i> | 102 |
| 4. | <i>Discussion</i> | 106 |
| 6. | CATHETER ANTENNA | 107 |
| 1. | <i>Introduction</i> | 107 |
| 2. | <i>Material and method</i> | 108 |
| 3. | <i>Result</i> | 108 |
| 4. | <i>Discussion</i> | 109 |
| 7. | DISCUSSION | 109 |
| 8. | REFERENCES..... | 110 |

V. GENERAL CONCLUSIONS.....114

VI. PUBLICATIONS LIST119

I. INTRODUCTION

Cardiovascular (CV) disease and cancer are the first cause of mortality in the whole world. In 2008, the world health organization reported. CV disease is responsible for 29% of deaths, followed by infectious diseases (16.2%) and cancers (12.6%) (WHO 2008). In the Western countries, cardiovascular disease is as deadly as cancer (28% vs. 30% respectively) (WHO 2008). Amongst cardiovascular disease, cardiac electrical diseases are a major burden for the patients (severe morbidity and poor quality of life) and the health care system. Mechanistically simple arrhythmias (involving a unique focus or circuit) can now be cured by localized energy application (catheter ablation) with a 99% success rate. For example atrial fibrillation, mainly triggered by ectopic foci from the pulmonary vein (Haïssaguerre et al. 1998), can be cured by the exclusion of venous sources by cryo or thermoablative therapy (Fuster et al. 2007). However, for 15 to 40% of the patients, the procedure remains inefficient and requiring redo the procedure. The cause is an inadequate power used to heat the tissue. For ventricular arrhythmias, radiofrequency ablation (RFA) has been proposed as an additional strategy to interrupt VT circuit (Cleland et al. 2006, Calvert et al. 2005). Magnetic resonance imaging (MRI) can help to control the heating deposition in the tissues and therefore to optimize the delivered power in space and time. MR thermometry (Quesson et al. 2000, Rieke & Butts Pauly 2008) was already used for the guidance of high intensity focused ultrasound (HIFU) ablations in different organs (uterine fibroid (Hindley et al. 2004), liver (Quesson et al. 2010) , kidney (Honeck et al. 2009), bone metastasis (Li et al. 2010) ...) and for RFA in liver (Seror et al. 2008) and heart (Kolandaivelu et al. 2010, D. Senneville et al. 2012). Currently, cancer treatments rely on surgery, chemotherapy, and radiotherapy. However, mini and non-invasive therapies like RFA and extracorporeal HIFU have found an increasing interest. In liver ablation by HIFU, one challenge is to increase thermal lesion size

for the treatment of large volumes (3 cm diameter or more), (Kohler et al. 2009, Charles Mougenot et al. 2004, Salomir et al. 2000). Another challenge is to avoid collateral damages induced to the bones of the rib cage located in the cone of the HIFU (Quesson et al. 2010, Cochard et al. 2011, Marquet et al. 2011, G elat et al. 2011).

The objectives of this work are:

- 1) to develop a method to increase the lesion size induced by HIFU based on bubble enhanced heating (BEH)
- 2) to propose a method for MR guided HIFU sonication through the rib cage using beam steering and avoiding heating of ribs
- 3) to develop MR thermometry in the heart for the monitoring of RF cardiac ablation.

1. MR thermometry

Different methods have been developed to map the temperature by using MRI (Rieke & Butts Pauly 2008, Quesson et al. 2000) based on: T_1 relaxation time of water protons, T_2 relaxation time of water protons, molecular diffusion constant of water molecules, temperature dependence of the magnetic susceptibility and water proton resonance frequency (PRF). PRF method is increasingly used for a number of applications (uterine fibroid, brain, liver, pancreas) because of the linearity between temperature change and phase variations observed in MR images and the near independence of the effect among tissues (except for fat). The relationship between temperature and the phase of MR images is:

$$\Delta T = \frac{\Delta\phi}{\alpha\gamma B_0 T_E}$$

where ΔT the temperature change, $\Delta\phi$ the phase difference between the reference image and the current image, α the temperature dependent water chemical shift equal to $0.94 \times 10^{-8} / ^\circ\text{C}$,

γ the gyromagnetic ratio of the proton equal to $2\pi \times 42.58 \times 10^6 \text{ rad T}^{-1}$, B_0 the static induction field, TE the echo time of the MR sequence. In order to map the temperature, single or multishot EPI can be used to ensure a high sampling rate of the temperature in adequacy to the heating duration (about a minute for HIFU and RF ablation) and in good agreement with the restricted time imposed by the physiological motions (respiratory motion, and cardiac contraction). At this time, studies have reported spatial resolution equal to $2.6 \times 2.6 \times 7\text{mm}$ for the heart (D. Senneville et al. 2012) and $2.2 \times 2.6 \times 6$ for the liver (Quesson et al. 2011) . The temperature precisions were about 2°C for the liver and 3°C for the heart.

2. Thermal dose

Temperature elevation can induce protein denaturation that results in cells death. This phenomenon depends on the temperature elevation and the exposure time. MR thermometry is able to measure temperature evolution and spatially map this evolution giving the possibility to estimate the lesion size due to thermal ablation (Quesson et al. 2011). Sapareto et al. introduced the concept of thermal dose (TD) (Sapareto & Dewey 1984) as followed:

$$TD = \int_0^t 2^{T(t)-43} dt \text{ if } T < 43^\circ\text{C}$$

$$TD = \int_0^t 4^{T(t)-43} dt \text{ if } T > 43^\circ\text{C}$$

The lethal thermal dose is reached for a temperature increase of 43°C during 240 min. The tissue necrosis appears for equivalent thermal dose equivalent to the lethal thermal dose. For 1°C temperature elevation over 43°C the required time to reach the lethal thermal dose was divided by 2; for examples: at 52°C the lethal thermal dose is reached after 28 s of heating, at 57°C (20°C elevation) the lethal thermal dose is reached after 1s of heating. Therefore,

temperature increases for thermal ablation remain sufficient in a range of 50 -60°C. Over this range, collateral damages could difficult to manage (C. Mougenot et al. 2011 Bruno Quesson et al. 2010).

3. References

Calvert, M.J. et al., 2005. Cost-effectiveness of cardiac resynchronization therapy: results from the CARE-HF trial. *European Heart Journal*, 26(24), p.2681-2688.

Cleland, J. G.F. et al., 2006. Longer-term effects of cardiac resynchronization therapy on mortality in heart failure [the CArdiac RESynchronization-Heart Failure (CARE-HF) trial extension phase]. *European Heart Journal*, 27(16), p.1928-1932.

Cochard, E. et al., 2011. Adaptive projection method applied to three-dimensional ultrasonic focusing and steering through the ribs. *The Journal of the Acoustical Society of America*, 130(2), p.716-723.

Fuster, V. et al., 2007. [ACC/AHA/ESC 2006 guidelines for the management of patients with atrial fibrillation--executive summary]. *Revista portuguesa de cardiologia: órgão oficial da Sociedade Portuguesa de Cardiologia = Portuguese journal of cardiology: an official journal of the Portuguese Society of Cardiology*, 26(4), p.383-446.

Gélat, P., ter Haar, G. & Saffari, N., 2011. Modelling of the acoustic field of a multi-element HIFU array scattered by human ribs. *Physics in Medicine and Biology*, 56(17), p.5553-5581.

Haïssaguerre, M. et al., 1998. Spontaneous Initiation of Atrial Fibrillation by Ectopic Beats Originating in the Pulmonary Veins. *New England Journal of Medicine*, 339(10), p.659-666.

- Hindley, J. et al., 2004. MRI guidance of focused ultrasound therapy of uterine fibroids: early results. *AJR. American journal of roentgenology*, 183(6), p.1713-1719.
- Honeck, P. et al., 2009. Magnetic resonance imaging as a technique for assessing noninvasive tissue ablation using high-intensity ultrasound: an experimental study. *Journal of endourology / Endourological Society*, 23(1), p.161-168.
- Köhler, Max O. et al., 2009. Volumetric HIFU ablation under 3D guidance of rapid MRI thermometry. *Medical Physics*, 36, p.3521.
- Kolandaivelu, A. et al., 2010. Noninvasive Assessment of Tissue Heating During Cardiac Radiofrequency Ablation Using MRI Thermography Clinical Perspective. *Circulation: Arrhythmia and Electrophysiology*, 3(5), p.521-529.
- Li, C. et al., 2010. Noninvasive treatment of malignant bone tumors using high-intensity focused ultrasound. *Cancer*, 116(16), p.3934-3942.
- Marquet, F. et al., 2011. Optimal transcostal high-intensity focused ultrasound with combined real-time 3D movement tracking and correction. *Physics in Medicine and Biology*, 56(22), p.7061-7080.
- Mougenot, C. et al., 2011. Quantification of near-field heating during volumetric MR-HIFU ablation. *Medical Physics*, 38, p.272.
- Mougenot, Charles et al., 2004. Automatic spatial and temporal temperature control for MR-guided focused ultrasound using fast 3D MR thermometry and multispiral trajectory of the focal point. *Magnetic Resonance in Medicine*, 52(5), p.1005-1015.

- Quesson, Bruno et al., 2010. A method for MRI guidance of intercostal high intensity focused ultrasound ablation in the liver. *Medical Physics*, 37(6), p.2533.
- Quesson, Bruno et al., 2011. Real-time volumetric MRI thermometry of focused ultrasound ablation in vivo: a feasibility study in pig liver and kidney. *NMR in Biomedicine*, 24(2), p.145-153.
- Quesson, Bruno, de Zwart, J.A. & Moonen, C.T.W., 2000a. Magnetic resonance temperature imaging for guidance of thermotherapy. *Journal of Magnetic Resonance Imaging*, 12(4), p.525-533.
- Quesson, Bruno, de Zwart, J.A. & Moonen, C.T.W., 2000b. Magnetic resonance temperature imaging for guidance of thermotherapy. *Journal of Magnetic Resonance Imaging*, 12(4), p.525-533.
- Rieke, V. & Butts Pauly, K., 2008. MR thermometry. *Journal of Magnetic Resonance Imaging: JMRI*, 27(2), p.376-390.
- Salomir, R. et al., 2000. Local hyperthermia with MR-guided focused ultrasound: Spiral trajectory of the focal point optimized for temperature uniformity in the target region. *Journal of Magnetic Resonance Imaging*, 12(4), p.571-583.
- Sapareto, S.A. & Dewey, W.C., 1984. Thermal dose determination in cancer therapy. *International Journal of Radiation Oncology*Biography*Physics*, 10(6), p.787-800.
- Senneville, D. et al., 2012. Feasibility of fast MR-thermometry during cardiac radiofrequency ablation. *NMR in Biomedicine*, 25(4), p.556-562.

Seror, O. et al., 2008. Real time monitoring of radiofrequency ablation based on MR thermometry and thermal dose in the pig liver in vivo. *European radiology*, 18(2), p.408-416.

WHO, 2008. WHO | The global burden of disease: 2004 update. *WHO*. Available at: http://www.who.int/healthinfo/global_burden_disease/2004_report_update/en/index.html

II. MR GUIDED HIFU ON THE LIVER

1. Magnetic resonance imaging for the exploitation of bubble enhanced heating by High Intensity Focused Ultrasound. A feasibility study in ex vivo liver.

Contribution: Delphine Elbes, Quentin Denost, Benjamin Robert, Max O. Köhler, Michaël Tanter, Quesson Bruno.

1. Abstract

- Objectives

Bubble enhanced heating (BEH) may be exploited for improving the heating efficiency of HIFU sonications in liver and for protection of tissues located beyond the focal point. The objectives of this study performed in ex vivo pig liver were 1) to determine the acoustic power threshold to induce BEH from displacement images measured by MR-acoustic radiation force imaging (MR-ARFI) 2) to compare temperature distribution with MR-thermometry for HIFU sonication protocols performed with and without BEH.

- Methods

The acoustic threshold to generate BEH was determined in *ex vivo* pig liver from MR-ARFI calibration curves of local tissue displacement resulting from sonications at different powers. Temperature distribution (MR-thermometry) resulting from “control” sonications (20W, 30 sec) were compared to “experimental” sonications performed with identical parameters but after a HIFU burst pulse (0.5 sec, acoustic power over the threshold for inducing BEH). Displacement images (MR-ARFI) were acquired between each sonication to measure

potential modifications of local tissue displacement associated with modifications of tissue acoustic characteristics induced by the burst HIFU pulse..

- Results

The acoustic threshold for inducing BEH corresponded to displacement amplitude of approximately 50 μm in ex vivo liver. The displacement and temperature images of the experimental group displayed a nearly spherical pattern, shifted by approximately 4 mm toward the transducer, in contrast with elliptical shapes centred at the natural focal position for the control group. The gain of the maximum temperature and displacement values were 1.5 and 2, and the full width at half maximum (FWHM) of the displacement data were 1.7 and 2.2 times larger than in the control group in directions perpendicular to ultrasound propagation axes.

- Conclusion

MR-ARFI is a promising method to increase the safety of HIFU treatment, by allowing the visualisation of the focus area before heating, and a useful tool to ensure a better exploitation of BEH

2. Introduction

Thermal ablation with High Intensity Focused Ultrasound (HIFU) is increasingly used for the non invasive treatment of malignant tumour (Chapman & Haar 2007, Enholm et al. 2010, S. H. Kim et al. 2010, Quesson et al. 2010). Magnetic Resonance (MR) thermometry allows online monitoring of the procedure, controlling the heating sonication in real time (Quesson et al. 2011), estimating the localization of focus, and predicting thermal lesion size through the calculation of the accumulated thermal dose (Sapareto & Dewey 1984) . Different sonication strategies have been developed to enlarge thermal lesion based on continuous sonications with electronic deflection and a design on trajectories including thermal diffusion phenomenon to create large and homogeneous ablation volumes while reducing required energy (Mougenot et al. 2004, Kohler et al. 2009) as compared to point by point sonications. Presence of bubbles cloud in the medium can be used to enlarge the heated region near the focal point by modifying the spatial distribution of the acoustic intensity (Vanhille & Campos-Pozuelo 2009, Kullervo Hynynen 1991, Sokka et al. 2003), resulting in a “tadpole” shape. Sokka *et al.* (Sokka et al. 2003) proposed to generate acoustic cavitation *in situ* at the focal point including a burst pulse in the beginning of the sonication protocol. This method is advantageous since it produces a nearly spherical lesion, increases the maximal temperature rise and the shielding effect of bubbles cloud or layer (Vanhille & Campos-Pozuelo 2009) may also reduce risks of damaging tissues in the far field (Zderic et al. 2008).

Although HIFU heating in presence of acoustic cavitation appears advantageous for increasing the heating efficiency, its applicability *in vivo* is limited due to the difficulty in precisely controlling of the phenomenon. Local acoustic pressure has to reach a threshold to induce cavitation. Local intensity at the targeted area appears hardly predictable due to

potential acoustic wave aberrations and absorption as the ultrasound beam passes through inhomogeneous structures (skin, subcutaneous fat layers, bones, bowels).

In Sokka's experiments (Sokka et al. 2003), the acoustic threshold was detected by analyzing the backward acoustic spectrum due to bubble activity (Kullervo Hynynen 1991, Lele 1967). More recently, acoustic mapping of broadband and harmonic emission (Jensen et al. 2012) was proposed to improve this technique. However, the analysis of such a signal for the treatment of liver tumors may be complicated because of the attenuation of the signal reflected from the focal area by soft tissue that can interfere with scattered emissions from structures located in the near field (e.g. bones). A recent study (T. D. Khokhlova et al. 2009) reported that boiling may be the main cause of the bubble. Independently of the physical cause of local changes of acoustic properties of tissues, resulting lesion and heating pattern remained similar in terms of shape and localization (shift toward the transducer). Furthermore, this change, related to bubble enhanced heating (referred as "BEH" in the following text), could be correlated with an acoustic power threshold. Beside already established applications of MR-ARFI (Marsac et al. 2012, Kaye et al. 2011, Larrat et al. 2010), this non invasive imaging method appears as a suitable candidate to investigate focal pattern of ultrasound distribution through imaging of local tissue displacement in the range of few micrometres induced by HIFU pulses, and reduces the risks of creating unwanted thermal damages associated with conventional test shot observed under MR-thermometry (pulsed mode versus continuous sonication) (Sinkus et al. 2008, McDannold & Maier 2008, Chen et al. 2010).

The objectives of this study performed in ex vivo pig liver were 1) to determine the acoustic power threshold to induce BEH from displacement images measured by MR-acoustic radiation force imaging 2) to compare temperature distribution with MR-thermometry for HIFU sonication protocols performed with and without BEH

3. Material and Methods

- Experimental setup

Experiments were performed at 1.5 Tesla with the Sonalleve MR-HIFU platform (Philips Healthcare, Vantaa, Finland) designed for the treatment of uterine fibroids (see Kohler et al. 2009) for technical description of the device). All sonications were performed at a frequency of 1.2 MHz in ex vivo porcine liver samples at room temperature. The liver was immersed in degassed water in a cylindrical plastic tank (20 cm in diameter) equipped with a membrane on the bottom part. This holder was positioned on top of the platform at the center of the acoustic window. A mixture of ultrasonic gel and degassed water was applied between the two membranes to ensure acoustic coupling. MR images were acquired with a circular single element surface coil located on top of the cylindrical container

- MR-ARFI measurements

The MR-ARFI acquisition sequence was a modified spin-echo sequence with two motion sensitive bipolar gradients added symmetrically from the refocusing pulse to encode into the phase of the MR image the tissue displacement associated with HIFU pulses. Each bipolar gradient (10 ms in length and 40mT/m in amplitude) was applied in the vertical direction (aligned with the ultrasound propagation axis) to encode tissue displacement in the MR phase image. Emission of ultrasound pulses were triggered on the motion encoding gradients and their duration were adjusted to cover a lobe of each bipolar gradient (twice 5 ms in duration). The acquisition parameters of the MR-ARFI sequence were TE/TR=53/1000 ms, 128 x 128 mm FOV, 128x128 acquisition matrix 90° flip angle and 3 contiguous slices of 2 mm thickness positioned in along the vertical HIFU beam axis, 2 averages, for a total acquisition

time of 4 min 16 sec. The positioning of these slices was adjusted from scout views images and by performing one MR-ARFI sequence in horizontal orientation to precisely identify the location of the maximal displacement.

MR-ARFI displacement images were computed from phase images with in-house developed software written in IDL (ITT, Visual Information Solutions). A reference phase image acquired without applying ultrasound was subtracted to each phase image to remove potential phase offsets related to imperfect refocusing. This difference phase image ($\Delta\phi$) was then spatially unwrapped (Denis De Senneville et al. 2006) and converted into displacement maps (Δd) with the following formula:

$$\Delta d = \frac{\Delta\phi}{2\tau\gamma G}$$

[1]

where γ is the gyromagnetic ratio ($\gamma/2\pi = 42,58$ MHz/T), G is the gradient amplitude and τ its duration. The factor 2 accounts for the double application of the bipolar gradients.

- MR thermometry

MR thermometry was performed using the Proton Resonant Frequency (PRF) shift method using a multishot Echo Planar Imaging (EPI) sequence, with the following acquisition parameters : echo train length of 11, TE/TR=18/300 ms, 128 x 128 mm FOV, 77x96 acquisition matrix, 40 ° flip angle, 3 adjacent slices of 2.5 mm thickness positioned in vertical orientation. Temperature images were calculated (PRF constant of 0.0094 ppm.°C⁻¹) and displayed with in-house developed software (“RealTI”) written in C++ and IDL (ITT, Visual Information Solutions).

- Experimental protocol

In these experiments, ultrasound pulses, with acoustic power ranged from 0 to 800 Wac, and depth in the liver ranging from 12 mm to 33 mm, were performed under MR-ARFI. Displacement shape, position and maximum displacement value were measured to identify potential changes of tissue acoustic properties for the determination of the BEH acoustic threshold.

In the first batch of experiments, displacement maps were acquired by progressively applying an increasing acoustic power. Calibration curve was plotted reporting the maximal value extracted on each displacement map as a function of acoustic power. The displacement threshold was determined by observing change of shape on displacement maps at the focus from elliptical to ‘tadpole’ shape. Calibration curves were then performed at low acoustic power ranging from 0 to 250 W. The acoustic power threshold was estimated by reporting the displacement value threshold, obtained in the ex vivo liver, on the fitted linear function (least square minimization) of the curve in the same range of depth.

In the second set of experiments, a protocol (see Figure II.1) was applied to compare displacement maps and heating characteristics in absence/presence of BEH. Experiments were divided in two groups:

- the control group consisted of a continuous and moderate sonication (20W, 30s) surrounding by MR-ARFI measurements to verify that no substantial modifications of tissue acoustics properties could be related to heating.
- the experimental group was composed of a burst pulse (250-800W, 0.5s) followed by a continue sonication (20W, 30s) surrounded by MR-ARFI measurements. Acoustic power of the burst pulse was deduced from calibration curve. The continuous sonication was identical to that used for the control group.

In order to illustrate the potential of exploiting BEH, additional experiments (N=3) performed on ex vivo liver consisted in targeting two spots at distinct locations distant from 6 mm in the horizontal plane. For each position, MR-ARFI calibration measurements were performed with 5 different acoustic power values (0 to 180 Wac). From these data, the power threshold values were determined and two sonications of 0.2 s in duration were performed above this acoustic threshold for inducing BEH. Then, displacement images were acquired to confirm modification of tissue acoustic properties. A sonication at 60 Wac during 30s was applied with alternative switching between both positions by +/-3 mm electronic deflection every 0.25 s, with the transducer positioned at the vertical median position between the two targeted points.

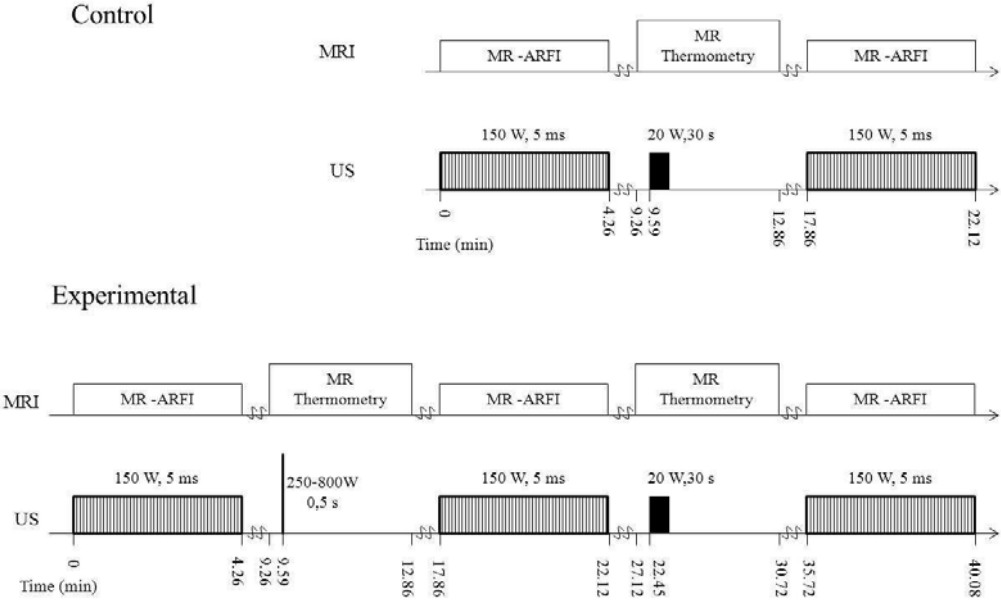


Figure II.1: Protocol describes MR sequences and sonication characteristics (duration and power) for the control group first part and for the experimental group, second part. In each part, the first line shows MR acquisition, the second line the ultrasound (US) as a function of time. Black rectangles indicate continuous sonications. Striped rectangles indicate pulsed sonications.

4. Results

- Calibration curve and BEH threshold determination

Figure II.2 presents a typical calibration data set that plots (figure II.2 a) the maximum displacement value at the focal spot induced by radiation pressure as a function of the acoustic power. A discontinuity in the displacement map shape at the focus from elliptical (2c) to tadpole (2b) was observed for a displacement amplitude of 50 μm , corresponding to 350Wac. Below 50 μm , the displacement varied linearly with the acoustic power. Above 50 μm , the experimental value deviated from a linear behaviour, with displacement values, at the natural focal point position, being lower than expected. The location of the maximal displacement value was shifted 4 mm toward the transducer. In the subsequent experiments, the acoustic power corresponding to a displacement of 50 μm was therefore selected as the threshold for inducing BEH in the second batch of experiments.

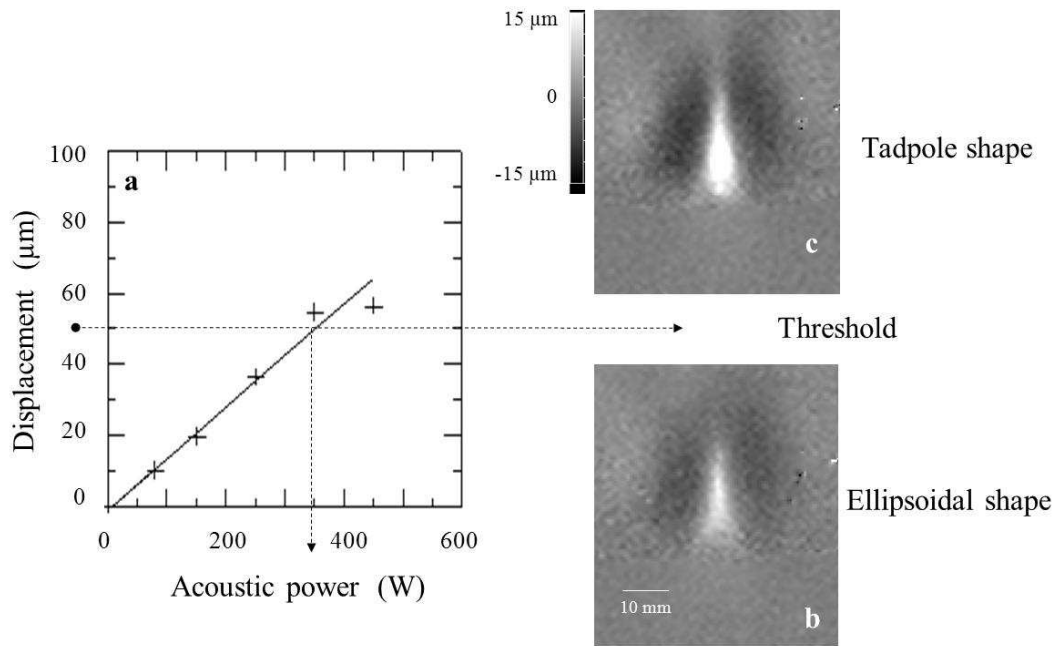


Figure II.2: MR-ARFI calibration set on ex-vivo liver. The graph (a) displays tissue displacement versus acoustic power. The solid line represents the linear fit of experimental data (cross) at low acoustic power (<300Wac). The horizontal dashed arrow in (a) symbolizes the threshold of tissue displacement corresponding to modification of the pattern on displacement images and the vertical dashed arrow indicates the corresponding acoustic power. Images in the right column are displacement maps obtained from MR-ARFI measurements, below (b) and above (c) the threshold

- Analysis of displacement and temperature images in control and experimental groups

Acquisition of several displacement images were performed with power ranging from 0 to 250 Wac. From these data, a linear fit of the displacement values measured at the natural focal point versus acoustic power was performed. The slope of the fit was used to calculate the acoustic power threshold corresponding to a local displacement of 50 µm at the same location, .

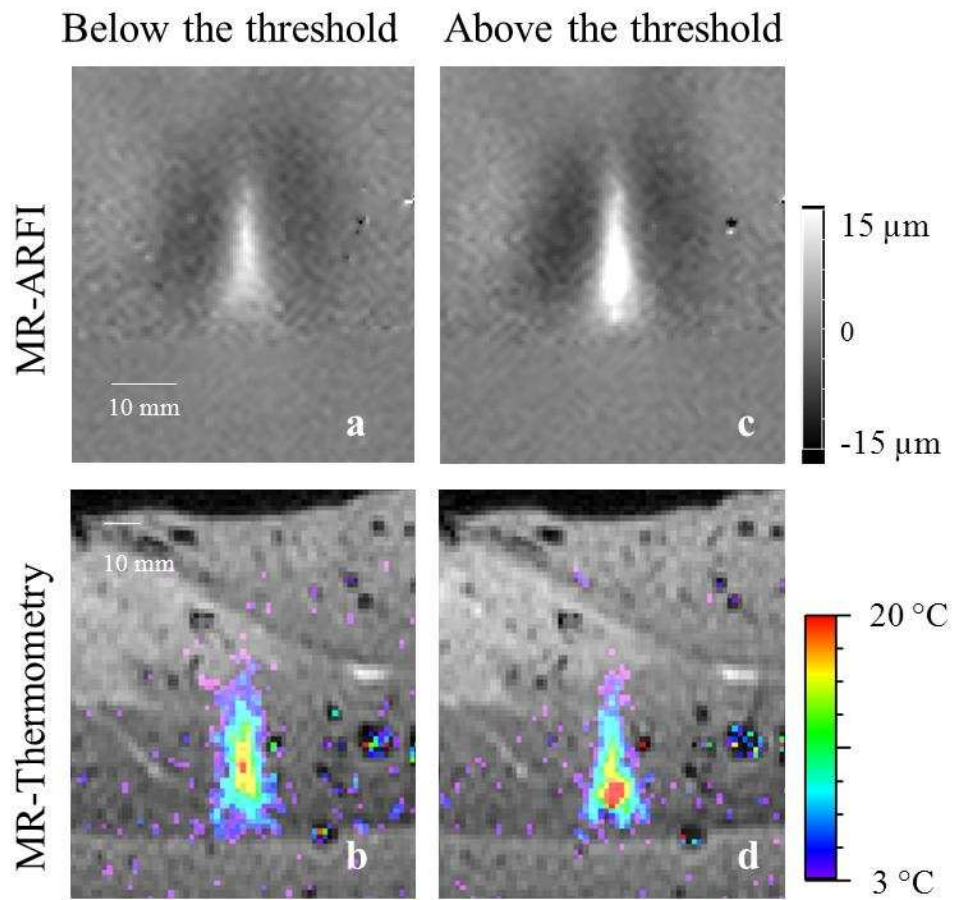


Figure II.3 Comparative results of local displacement maps (a and b) and temperature images (c and d) for control group (left column) and experimental group (right column). Displacement images were obtained at acoustic power of 150 Wac, and temperature images at the end of identical sonications performed at 20Wac during 30 sec. Displacement and temperature scales are indicated on the right.

Figure II.3 shows MR-ARFI displacement images on the top row and MR-Thermometry images overlaid on MR magnitude images on the bottom row, for the control (left column) and experimental (right column) groups. The power threshold corresponding to 50 μm displacement was 500 Wac for this dataset. Displacement images acquired before (fig 3a) the sonication performed at 20W during 30 sec under MR-thermometry (fig 3b) display a near elliptical shape at the focus. MR-ARFI images acquired after the continuous sonication showed identical displacement characteristics (shape, maximal amplitude and location) as in figure II.3a (data not shown). The displacement map acquired after the burst pulse (fig 3c) shows a modification of the spatial distribution of the displacement induced by HIFU and the heating sonication (fig 3d) performed at 20 W during 30 s resulted in a tadpole shaped heating.

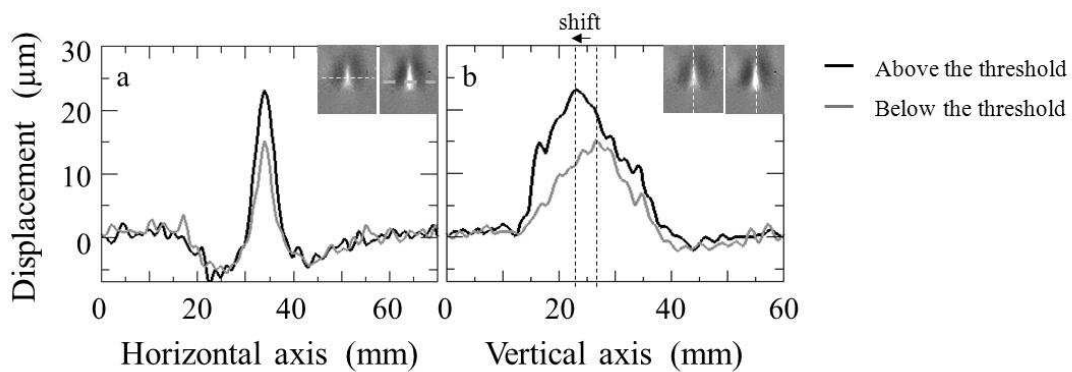


Figure II.4: Horizontal (a) and vertical (b) profiles of displacement maps for control (grey) and experimental (black) group. Profiles were selected at the maximal displacement value on each displacement map (see dashed lines on inserts at the right part of the corresponding graph).

Figure II.4 compares displacement map below and above the threshold, plotting horizontal (fig II.4a) and vertical (fig II.4b) profiles intersecting the pixel of the maximum displacement for each group. The maximal displacement value was increased by 55% in the experimental group and the transverse FWHM was 60% larger than in the control group. Positions of the maxima were identical in the ultrasound propagation direction. However, in the experimental group, the maximum was shifted by 4mm toward the transducer. The FWHM in the vertical direction remained unchanged.

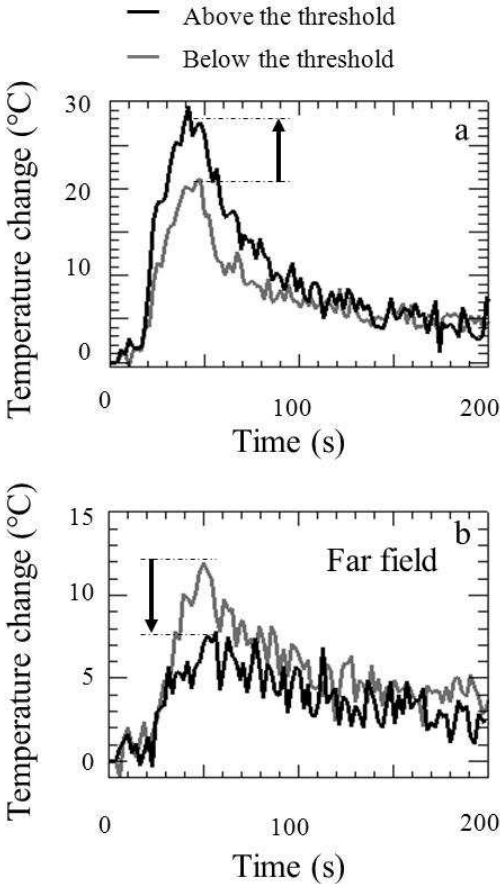


Figure II.5: Temperature evolution for identical sonications (20Wac, 30 sec). Graph (a) plots temperature evolution in the pixel displaying the maximal temperature increase for control (grey line) and experimental (black line) groups. Graph (b) plots temperature evolution in the same pixel located 2 mm beyond the natural focal point.

Figure II.5 displays the comparative analysis (figure II.5) of temperature data from the same experiment shown in Figure II.4. The experimental group showed a 55% increase in the maximum temperature rise at the hottest pixel (figure II.5a), but a reduction of nearly 50% of the maximum temperature increase 2mm beyond the natural focal point (figure II.5b) compared to the control group.

Table II.1 summarizes results obtained from the analysis of displacement and temperature maps, in terms of shift in position, increase in the transverse size and in amplitude at the focus. The shift of the maximum was observed for both modalities and reached 4.3 ± 1.7 mm in displacement maps and 4.6 ± 2.7 mm in temperature data. Over the threshold, the focal spot spread out in the transverse direction with an increase of the FWHM in the horizontal direction by a factor 2.2 ± 0.5 and 1.7 ± 0.6 for displacement maps and temperature data, respectively. At the focus, an increase of maximum by a factor of 2.0 ± 0.6 was observed in displacement maps, and by a factor of 1.5 ± 0.2 for the maximum temperature increase.

| | MR-ARFI (N=13) | Thermometry (N=7) |
|-----------------------|-------------------|----------------------|
| Shift (mm) of maximum | 4.3 ± 1.7 | 4.6 ± 2.7 |
| Gain on FWHM | 2.2 ± 0.5 | 1.7 ± 0.6 |
| Gain on amplitude | 2.0 ± 0.6 | 1.5 ± 0.2 |

Table II. 1: Shift in position, gain in size in the transverse direction (FWHM) and gain in amplitude observed in MR-ARFI and MR thermometry in presence of BEH as compared to data measured in absence of BEH.

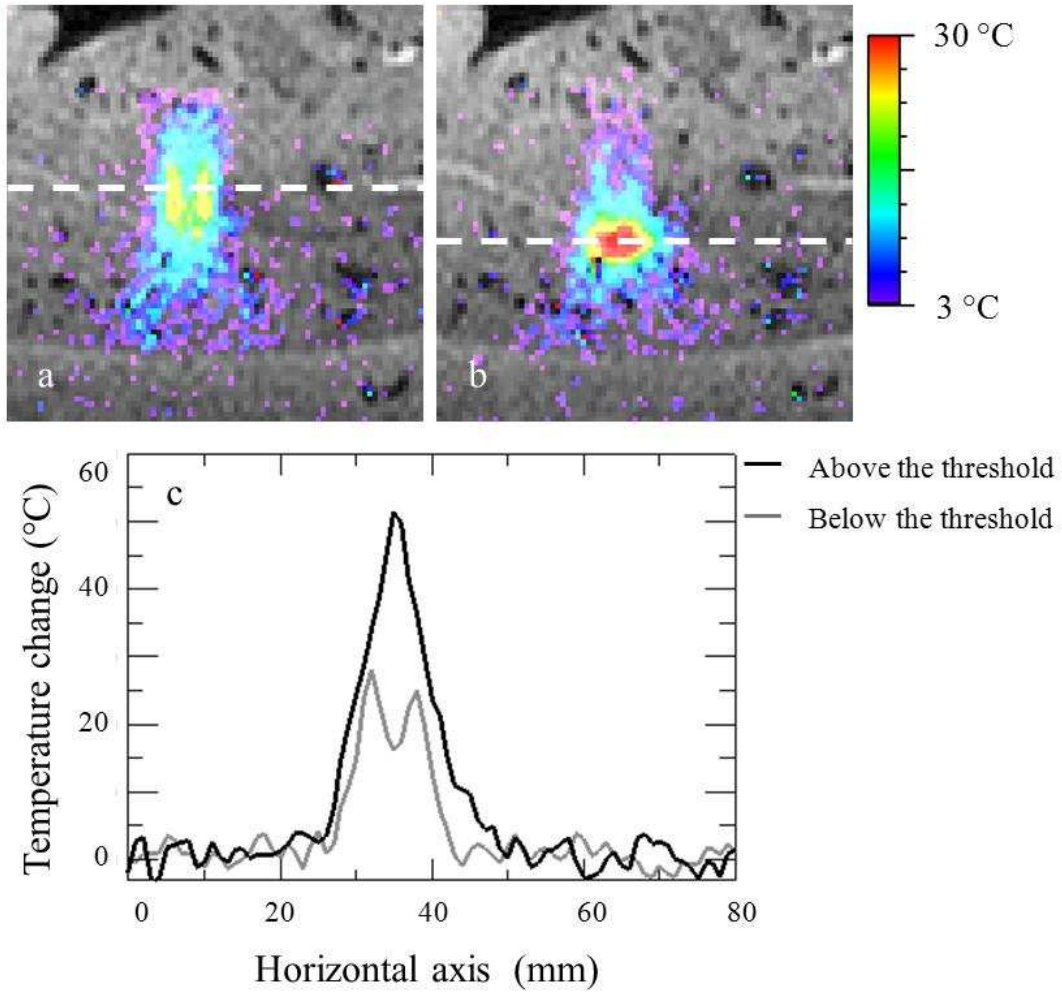


Figure II.6: Example of temperature data, control (left) and experimental (right) conditions, for sonications performed with 2 targeted points. Image (a) and (b) display temperature distributions at the end of the sonication for both conditions. The graph in (c) displays the horizontal temperature profiles at the end of each sonication, centered on the maximal temperature increase as indicated by the white dashed line.

Figure II.6 compares temperature data from dual spot heating without (Figure II.6a) and with (Figure II.6b) BEH. Both targeted positions were spaced of 6mm. The first condition generated two elliptical individual spots elongated in the direction of ultrasound propagation, whereas the latter condition resulted in an elliptic heating shape elongated in the horizontal direction and shifted toward the transducer. Comparative analysis of the horizontal temperature profiles located for each plot at focus level and at the end of each sonication (Figure II.6c) revealed a much higher temperature increase (50°C maximal value *versus* 25°C for the control condition) for the case where the tissue was previously sonicated with a burst pulse at each targeted location.

5. Discussion

In this study, MR-ARFI was used to visualize the local displacement induced by HIFU sonications in *ex vivo* liver, in order to determine the acoustic power threshold to induce BEH. Similar approach could have been performed with MR thermometry by observing modifications of the temperature distribution as a function of the delivered ultrasound power. However, MR-ARFI offers the advantage of lowering the deposited acoustic energy inherent to the low duty cycle (3% in our implementation) emission of ultrasound pulses. Therefore, MR-ARFI offers a more secure approach than conventional heating tests, reducing the risks of creating unwanted damages. The total acoustic energy deposition during the spin-echo based sequence used in the present work may also be reduced by parallel imaging techniques or by the use of rapid gradient echo based acquisitions (Auboiroux et al. s. d.) with alternated bipolar gradients or spin echo-echo planar imaging (Kaye et al. 2011) with shifting of the readout echo. Both methods were developed to make the sequence sensitive to both local tissue displacement and temperature change. Whatever the sequence, the central objective of this study was to evaluate the required acoustic power to further exploit BEH. In the literature (Sokka et al. 2003, T. D. Khokhlova et al. 2009), the threshold for inducing BEH has been related to acoustic power emitted by the transducer or local pressure value at the focus, the link between both being dependent on transducer characteristics in homogeneous media. However, the effective local pressure at the focus in biological tissue is difficult to assess since it depends on attenuation and diffraction of ultrasound wave in heterogeneous media (skin, subcutaneous fat, muscle, liver, bones). Displacement maps, calculated from MR-ARFI phase images, allow for the rapid determination of the threshold across any types of transducer and independently of sonication depth. This approach is advantageous since it provides a practical solution to estimate the acoustic power threshold to deliver without requiring precise prior

knowledge of tissue composition. The displacement threshold was found to be around 50 μm in ex vivo liver. This value was selected to estimate the minimal acoustic power required for inducing BEH. At each targeted location, only a limited number of calibration data were required, since measurement of the first points of the curve at low acoustic energy was sufficient to estimate the acoustic power of the threshold. Each sonication performed after the burst pulse with acoustic power higher than the threshold resulted in modification of the displacement map and a tadpole shape heating, with an improvement of approximately 50% in maximum temperature increase and a broader heating distribution in the horizontal direction. These results are in a good agreement with results reported by Sokka et al (Sokka et al. 2003), who attributed the local change at the focal point to acoustic cavitation based on the analysis of ultrasound measurements. In another recent study (T. D. Khokhlova et al. 2009) performed on gel samples, boiling was presented as the main physical phenomenon explaining tadpole heating. In the present study, no evidence of boiling could be established since temperature measurements were far below 100°C and no millimetre size bubble could be visualized near the focus region on the MR images (ARFI and temperature), as reported by Khokhlova *et al.* (T. D. Khokhlova et al. 2009). Partial volume effect of the MR thermometry sequence may alter the visibility of the bubble and underestimate maximal temperature increase. However, a millimetre scale bubble would have been visible on magnitude images of the MR-ARFI sequence, if present. Moreover, a delay of 5 minutes was kept between each MR acquisition sequence to ensure complete thermal relaxation. We observe that the BEH effect in liver tissue is persistent over this delay. The displacement maps acquired after the HIFU burst pulse indicate a change in maximal displacement value that may be related to change in tissue elasticity. Sapin et al have analysed the change of elasticity in tissues as a function of temperature (Sapin-de Brosses et al. 2010). They reported a hysteresis curve of the shear modulus as a function of the temperature, with a decrease inversely proportional to

temperature below 50°C followed by an increase above 60°C. After, irreversible thermal denaturation of tissue has occurred. Therefore, in case of irreversible thermal damage induced by the burst pulse, a reduction of the maximal displacement value would have been expected. On the contrary, a two fold increase in maximal displacement value has been observed (fig 4b), indicative of a reduction of tissue stiffness near the focal region.

Therefore, our results suggest that irreversible thermal tissue damage has not been induced by the burst pulse in *ex vivo* liver sample for the selected acoustic power values used in our experimental protocol. Further studies should investigate the precise mechanism BEH in biological tissue, namely the relative influence of non-linear propagation effects, cavitation and boiling and if the observed persistence in time of the effect is reproducible *in vivo*. This may be accomplished by combining for example MR-ARFI/MR-thermometry data and ultrasound measurements. Such an approach could not be performed in our current experimental setup and these objectives were clearly out of the scope of the present work.

The position of the maximal displacement and temperature increase were shifted toward the transducer by approximately 4.4 mm for both modalities, in the same range as already reported in the literature (T. D. Khokhlova et al. 2009, Kullervo Hynynen 1991). We confirm that BEH can be exploited to create in *ex vivo* liver near spherical thermal lesions of larger dimensions than conventional sonications, which may be beneficial for hepatic tumour ablation. Moreover, prediction of local change in tissue characteristic as a function of acoustic power could be further exploited in the design of new sonication strategies, with the objectives of 1) protection of structures located beyond the natural focal point (Figure II.5) and 2) minimization of the output acoustic power in order to reduce energy deposition in the near field and maximization the heating efficiency at the targeted area.

One challenge in HIFU thermal ablation is to enlarge lesion dimensions. A number of strategies have been proposed, such as spiral⁷ and concentric⁸ trajectories using rapid

electronic deflection of the HIFU beam, and exploiting thermal diffusion to generate homogeneous volumetric heating. However, despite these strategies reduce the treatment duration as compared to point by point sonications, the resulting lesions remain anisotropic and elongated in the ultrasound propagation direction. This, in turn, restricts the maximal dimension of achievable ablation size in the transverse direction. Exploitation of BEH based on MR-ARFI calibration at low acoustic power, as shown from data presented in Figure II.6, assuming a persistence of the effect over several minutes after the burst pulse could open new possibilities to create thermal lesions of desired shape and size, while reducing the energy deposition in tissues located in the near field.

As a conclusion, MR-ARFI offers an elegant and non invasive imaging method to predict acoustic power over which BEH effect appear.

6. References

- Auboiroux, V. et al., ARFI-prepared MRgHIFU in liver: Simultaneous mapping of ARFI-displacement and temperature elevation, using a fast GRE-EPI sequence. *Magnetic Resonance in Medicine*.
- Chapman, A. & Haar, G., 2007. Thermal ablation of uterine fibroids using MR-guided focused ultrasound-a truly non-invasive treatment modality. *European Radiology*, 17(10), p.2505-2511.
- Chen, J., Watkins, R. & Pauly, K.B., 2010. Optimization of encoding gradients for MR-ARFI. *Magnetic Resonance in Medicine*, 63(4), p.1050-1058.

- Denis De Senneville, B. et al., 2006. Robust spatial phase unwrapping for on-line MR-temperature monitoring. In *Proceedings - International Conference on Image Processing, ICIP*. p. III137-III140.
- Enholtm, J. et al., 2010. Preliminary Results: MR Guided Volumetric HIFU Ablation of Uterine Fibroids with Binary Feedback Control Kullervo Hynynen & J. Souquet, éd. *AIP Conference Proceedings*, 1215(1), p.12-14.
- Hynynen, Kullervo, 1991. The threshold for thermally significant cavitation in dog's thigh muscle in vivo. *Ultrasound in Medicine & Biology*, 17(2), p.157-169.
- Jensen, C.R. et al., 2012. Spatiotemporal Monitoring of High-Intensity Focused Ultrasound Therapy with Passive Acoustic Mapping. *Radiology*, 262(1), p.252-261.
- Kaye, E.A., Chen, J. & Pauly, K.B., 2011. Rapid MR-ARFI method for focal spot localization during focused ultrasound therapy. *Magnetic Resonance in Medicine*, 65(3), p.738-743.
- Khokhlova, T.D. et al., 2009. Magnetic resonance imaging of boiling induced by high intensity focused ultrasound. *Journal of the Acoustical Society of America*, 125(4), p.2420-2431.
- Kim, S.H. et al., 2010. The potential role of dynamic MRI in assessing the effectiveness of high-intensity focused ultrasound ablation of breast cancer. *International Journal of Hyperthermia*, 26(6), p.594-603.
- Köhler, M.O. et al., 2009. Volumetric HIFU ablation under 3D guidance of rapid MRI thermometry. *Medical Physics*, 36, p.3521.
- Larrat, B. et al., 2010. MR-guided transcranial brain HIFU in small animal models. *Physics in Medicine and Biology*, 55(2), p.365-388.

- Lele, P., 1967. Production of deep focal lesions by focused ultrasound-current status. *Ultrasonics*, 5(2), p.105-112.
- Marsac, L. et al., 2012. MR-guided adaptive focusing of therapeutic ultrasound beams in the human head. *Medical Physics*, 39(2), p.1141-1149.
- McDannold, N. & Maier, S.E., 2008. Magnetic resonance acoustic radiation force imaging. *Medical Physics*, 35(8), p.3748.
- Mougenot, C. et al., 2004. Automatic spatial and temporal temperature control for MR-guided focused ultrasound using fast 3D MR thermometry and multispiral trajectory of the focal point. *Magnetic Resonance in Medicine*, 52(5), p.1005-1015.
- Quesson, Bruno et al., 2010. A method for MRI guidance of intercostal high intensity focused ultrasound ablation in the liver. *Medical Physics*, 37(6), p.2533.
- Quesson, Bruno et al., 2011. Real-time volumetric MRI thermometry of focused ultrasound ablation in vivo: a feasibility study in pig liver and kidney. *NMR in Biomedicine*, 24(2), p.145-153.
- Sapareto, S.A. & Dewey, W.C., 1984. Thermal dose determination in cancer therapy. *International Journal of Radiation Oncology*Biology*Physics*, 10(6), p.787-800.
- Sapin-de Brosses, E. et al., 2010. Temperature dependence of the shear modulus of soft tissues assessed by ultrasound. *Physics in Medicine and Biology*, 55(6), p.1701-1718.
- Sinkus, R. et al., 2008. Potential of MRI and Ultrasound Radiation Force in Elastography: Applications to Diagnosis and Therapy. *Proceedings of the IEEE*, 96(3), p.490 -499.
- Sokka, S.D., King, R. & Hynynen, K, 2003. MRI-guided gas bubble enhanced ultrasound heating in vivo rabbit thigh. *Physics in Medicine and Biology*, 48(2), p.223-241.

Vanhille, C. & Campos-Pozuelo, C., 2009. Nonlinear ultrasonic waves in bubbly liquids with nonhomogeneous bubble distribution: Numerical experiments. *Ultrasonics Sonochemistry*, 16(5), p.669-685.

Zderic, V. et al., 2008. Prevention of post-focal thermal damage by formation of bubbles at the focus during high intensity focused ultrasound therapy. *Medical Physics*, 35(10), p.4292.

2. A Preclinical Study of in vivo MR-guided Enhanced Ultrasound Heating in Pig Liver

Contribution: Delphine Elbes, MD Quentin Denost, Christophe Laurent, Hervé Trillaud, Anne Rullier, Bruno Quesson.

1. Abstract

Bubble enhanced heating (BEH) can be exploited for increased heating efficiency for the non-invasive High Intensity Focused Ultrasound treatment of liver tumours. The objectives of this *in vivo* study on the pig liver were (i) to calibrate the acoustic intensity to determine the BEH threshold, (ii) to compare with real-time MR-thermometry the heating patterns obtained with sonications performed with and without BEH. The threshold in acoustic power for the generation of BEH in the liver of pigs *in vivo* was determined using sonications of 0.5 sec duration (“burst pulse”) under real-time MR-thermometry. In a second step, experimental sonications composed by a burst pulse followed by continuous sonication (14.5 sec) were compared to control sonications (15sec) of identical energy (1.8 kJ). 600-800 acoustic watts were required to observe a modification of the heating pattern at the targeted region located between 20 to 25 mm depth in the liver. The experimental group revealed near spherical heating with a mean enhancement of 40% in the maximal temperature rise as compared to the control group, a mean shift of 7 ± 3.3 mm toward the transducer and reduction of the post focal temperature increase. MR-thermometry can be exploited for controlling BEH *in vivo* in the liver. Using experimental sonications, more efficient heating can be achieved while protecting the tissues located beyond the focal point.

2. Introduction

Magnetic Resonance (MR) guided High Intensity Focused Ultrasound (HIFU) is a promising non-invasive method for the treatment of liver tumours (Quesson et al., 2011, Rieke and Butts Pauly, 2008, Quesson et al., 2010). Although the clinical feasibility of hepatic tumours treatment with HIFU has been demonstrated (Wu et al., 2004), this technique is not yet considered as routine. MR thermometry in mobile tissues remains challenging and requires fast acquisition sequences in combination with real time motion compensation algorithms (Quesson et al., 2011, Rieke and Butts Pauly, 2008, de Senneville et al., 2007, Hazle et al., 2002). The blood perfusion in the liver acts as a “heat-sink” that reduces the efficiency of the treatment. As a consequence, short duration sonication protocols with high acoustic intensity are preferable to ensure sufficient tissue heating at the targeted region (Quesson et al., 2000, Liu et al., 2005, Wu et al., 2004). However, such sonications result in substantial energy deposition that may induce collateral damages in tissues located in the near field (skin, fat, muscle, bones) of the HIFU beam and/or beyond the focal point, at interfaces with air filled structures (stomach, bowels) (Zderic et al., 2008). Sonication strategies exploiting non linear acoustic propagation have been proposed (Holt and Roy, 2001, Clarke and ter Haar, 1997, Hynynen, 1991) based on injection of pressure sensitive microbubbles (Chen et al., 2003, Tu et al., 2006), on two ultrasound beams operating at different frequencies (Owen et al., 2010, Sokka et al., 2005, Liu et al., 2006), on a long duration sonication inducing boiling (Khokhlova et al., 2009) or on a monochromatic sonication of sufficient acoustic intensity (Sokka et al., 2003). A study of Sokka et al. (Sokka et al., 2003) compared sonications at constant intensity with sonication that included an initial burst pulse of sufficient power to induce acoustic cavitation followed by a sonication at lower constant intensity. They reported a higher temperature increase in thigh muscles of rabbit by

application of the latter strategy than compared with standard sonication. Moreover, the temperature distribution was shown to be near spherical (so called “tadpole shape” Coussios et al., 2007) instead of ellipsoidal. However, the temperature values measured by MR-thermometry were spatially averaged, making the quantitative comparison between both experimental conditions difficult to assess. More recently, Inaba (Inaba et al., 2011) have exploited a similar approach in gel sample and chicken breast, applying burst pulses immediately followed by a continuous sonication at three different locations using electronic deflection. The resulting lesion was enlarged perpendicularly to the ultrasound propagation direction, merging the three initial foci, which was not observed in absence of acoustic cavitation. Increasing the heating efficiency by exploiting non linear HIFU propagation approaches constitutes a step forward for the development of non invasive treatments in the liver where large volumes have to be treated. Imaging techniques based on ultrasound (Ebbini et al., 2006, Hockham et al., 2010, Gyongy and Coussios, 2010), detector phase array, shear wave imaging (Macé et al., 2011) and MR (Macé et al., 2011) have been suggested to visualize either the local tissue displacement or the temperature increase during test sonications performed at low energy.

The objectives of the present work were: (i) to demonstrate the feasibility of increasing the heating efficiency of enhanced sonications exploiting BEH in the liver of pig *in vivo* using a clinical platform (ii) to determine the acoustic threshold for such effects with real time, motion compensated MR-Thermometry and (iii) to compare the resulted heating patterns and thermal lesion characteristics resulting from continuous sonications and sonications including a burst pulse.

3. Material and methods

- Animal preparation

Animal experiments were performed under experimental conditions approved by the local Animal Care and Use Committee (agreement #02092009). Four pigs (approximately 65 kg) were sedated by intramuscular injection of 0.1mg.kg⁻¹ of acepromazine (Calmivet, Vetoquinol, Lure, France) and anesthetized by intravenous injection of 0.1 mL kg⁻¹ of pentobarbital (CEVA Santé Animale, Libourne, France). The analgesia was introduced by an intramuscular injection of ketoprofen (Ketofene, Merial, Lyon, France) at a dose of 3mg.kg⁻¹. The anesthesia was maintained by continuous intravenous injection through the ear vein of pentobarbital at a rate of 7.2mgkg⁻¹.h⁻¹. The abdomen was carefully shaved and depilatory cream was applied for removing residual hairs in order to ensure correct propagation of the ultrasound beam through the skin. The animals were transferred to the 1.5 Tesla MRI (Achieva/Intera, Philips, The Netherlands) suite and installed in prone position on top of a Sonalleve MR-HIFU platform (Philips, Vantaa, Finland, see Kohler et al., 2009 for a detailed description of the platform). A solid gel was inserted between the membrane located on top of the water tank containing the HIFU transducer and the animal skin, and a mixture of liquid gel and degassed water was applied to avoid presence of air bubbles in the beam path. The animals were maintained under assisted ventilation (400 mL at 45% O₂ at a frequency of 20 bpm) during the procedure (respirator paraPac; ResMed SA, Saint priest, France). The cardiac frequency of the animal was continuously monitored and the rectal temperature was controlled every 30 minutes. After completion of the MR-guided HIFU experiments, the animals were transferred to the experimental surgery laboratory (DETERCA, Université Bordeaux Segalen, Bordeaux, France), euthanized by intravenous injection of Dolethal

(CEVA Santé Animale, Libourne, France) and dissected for histological analysis of the liver (see below for details).

- *Sonication protocol*

The position of the transducer was carefully adjusted under MR anatomical images to avoid the presence of ribs or cartilage in the beam path, selecting an acoustic window inferior to the sternum. For this purpose, T1-weighted images were acquired using fast three-dimensional gradient-echo sequences, with TE/TR=4.6/8.6 ms, 15° flip angle, bandwidth of 990 Hz, field of view of 350x350x180mm³, matrix of 256x256x60 and slice thickness of 3 mm, leading to a voxel size of 1.37x1.37x3 mm³. All the sonications were performed at a frequency of 1.2 MHz and local temperature increase was assessed by rapid, multi-slice MR thermometry (see below for detailed description of the MR thermometry protocol). The protocol was designed in two parts:

- First, the determination of the acoustic power threshold for the depth range of investigation in the liver: from 20 mm to 25 mm. At 20 mm and 25 mm depth in the liver five consecutive sonications of 0.5 sec (referred to ‘burst’ in the following text) duration were performed at the same location and the acoustic power was increased (from 400 to 800 acoustic watts (W_{ac})) until a modification could be observed on the temperature distribution (see paragraph “data analysis” for details). A minimum delay of 5 minutes was observed between each sonication to ensure complete thermal relaxation of tissues (Quesson et al., 2010).
- Then, two sonication protocols were compared:

- Control sonication (N=10) consisted of sonications performed at 120 Wac for 15 seconds (1800 J total energy). The sonication depth in the liver was set to 20 mm (N=6), 25 mm (N=4).
- Experimental sonication (N=16) was designed associating a burst pulse of 0.5 sec in duration at an acoustic power higher than the predetermined acoustic power threshold with a continuous sonication of 14.5 sec duration. The acoustic power of the latter sonication was adjusted to emit identical total acoustic energy (1800 J) as in the control sonication.

Additional experiments (N=2) were performed to compare control and experimental sonication at two locations separated by a distance of 10 mm in the direction perpendicular to the ultrasound propagation (Inaba et al., 2011).

- MR-thermometry

MR temperature images were acquired prior, during and after each HIFU sonication using multi-slice, RF-spoiled, single shot echo-planar imaging (EPI) (TE/TR = 29 ms/84ms, FOV = 300×300 mm, RFOV = 45%, flip angle = 45°, 4 parallel horizontal adjacent slices and 1 vertical slice, thickness = 7 mm, matrix size = 128 x 128) to analyse temperature evolution in space and time in the liver and skin. Temperature maps were calculated in real-time with the proton resonant frequency (PRF) method, including motion compensation with the multi-reference baseline technique (the first 40 acquired volumes) (see Quesson et al., 2011) for details). A non-heated circular region (typical size of 7 pixels in diameter) located within the liver but outside the heated region was selected on each slice for compensation of the temporal drift of the magnet field. The standard deviation of the thermometry was measured at each sonication location. For this purpose, a standard deviation map was computed on the acquired volumes between the first 40 data samples used for motion compensation and the

beginning of the sonication. Thermal dose maps were computed according to the Sapareto equation (Sapareto and Dewey, 1984) that reported a lethal threshold corresponding to constant heating at 43°C during 240 min (denoted as 240CEM43), adding the rectal temperature (taken as the reference temperature) to the MR temperature images.

- *Data analysis*

Evaluation of BEH threshold: the presence of BEH was assessed on MR temperature images by detecting a shift toward the transducer of the maximal temperature increase (as reported in (Zderic et al., 2008, Khokhlova et al., 2009, Sokka et al., 2003)).

Heating pattern analysis for control and experimental sonications : on the sagittal slice, the shape of the temperature distribution was visually identified as ellipsoid or tadpole. On the coronal slices, the hottest pixel in the stack was identified and the temperature evolutions at the same in-plane coordinates were plotted for all slices. The maximal temperature increase on each curve was measured. The size of the apparent lesion was estimated on the thermal dose image obtained at the end of the cooling period.

Histological analysis

Immediately after sacrifice of the animal, the liver was surgically extracted, flushed with physiologic fluid at room temperature through the main portal trunk and their ramifications, and then fixed with 10% formalin fluid using the same procedure. After at least 7 days of fixation, each liver was cut in its entirety in 3 mm slices. Each slice displaying a lesion was photographed and the lesion dimensions were measured. Each lesion was then selected for histological analysis by an experienced pathologist under light microscopy, using haematoxylin-eosine-saffron preparations.

4. Results

The body temperature of the anaesthetized animals ranged between 34.5 and 37°C. For all the investigated animals, no skin burns were observed after completion of the MR-HIFU experiments. One liver sample could not be analyzed for histology due to a technical problem at the surgery laboratory. The standard deviation of motion corrected MR temperature data was typically 1°C for all the sonicated areas.

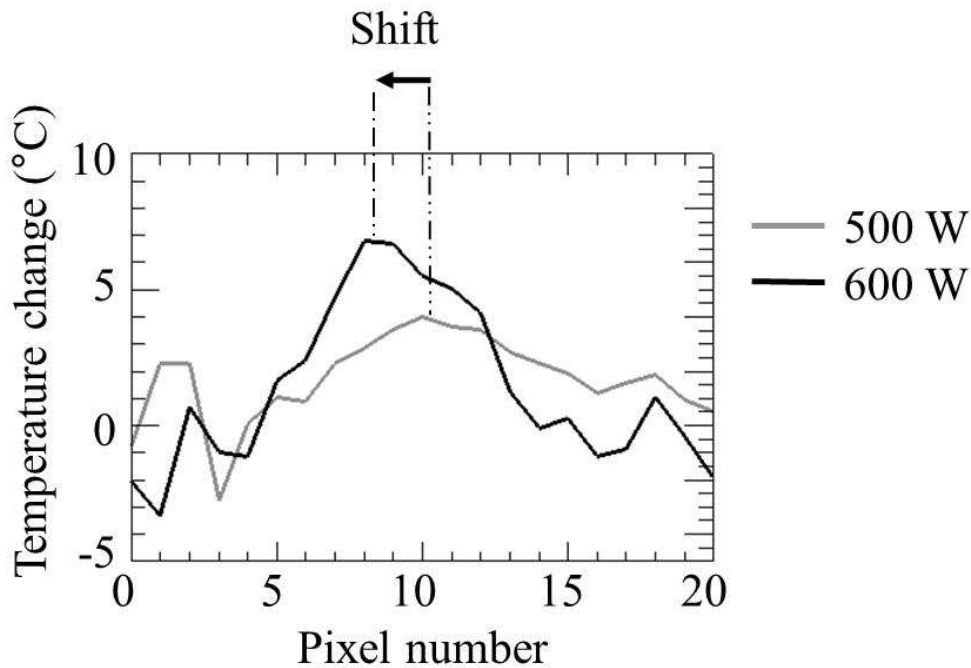


Figure.II.7: MR-Temperature profiles in the vertical direction crossing the focal point for two burst pulse sonications of 500 W (grey curve) and 600 W (black curve) acoustic power. The sonication depth was 20 mm in the liver. The horizontal arrow on top of the graph indicates the shift in position of the maximum temperature increase (location are indicated by the vertical dashed lines) toward the transducer.

- Threshold determination

Figure II.7 displays vertical profiles of temperature intersecting the hottest pixel for two sonications (0.5 sec duration) performed at 20 mm in the liver using acoustic powers of 500 W and 600 W, respectively. At 500W, the maximal temperature increase was approximately 4°C, and the temperature distribution in the vertical imaging slice remained ellipsoid (data not shown). The temperature rose up to 7 °C for the sonication performed at 600 W and the location of the maximal temperature increase was shifted toward the transducer by 2 pixels (4.7 mm). For sonications performed at 30 mm depth in the liver (data not shown), the acoustic power required to observe a modification of the position of the maximal temperature rise was 800 W. The mean shift ($\pm\sigma$) of the maximum was 7.0 (± 3.3) mm across all sonication depths.

- Sonication protocols comparison

Figure II.8 presents comparative temperature data sets for two sonications (control and experimental groups) performed at a depth of 20 mm in the liver. The temperature distribution at the end of the sonication for the control group (fig 2a) is elliptic whereas it appears circular for the experimental group (fig 2b) and has a shift toward the transducer of 6 mm. The number of pixels with temperature higher than 15°C was 3 and 9 for each condition, respectively. The temperature evolution (fig 2c) of the pixel showing the maximal temperature rise reveals maximal values of 18°C for the control condition and 24°C for the experimental condition, respectively. During the cooling period, the temperature returned to half of the maximal value in 10 and 20 sec for control and experimental sonications, respectively.

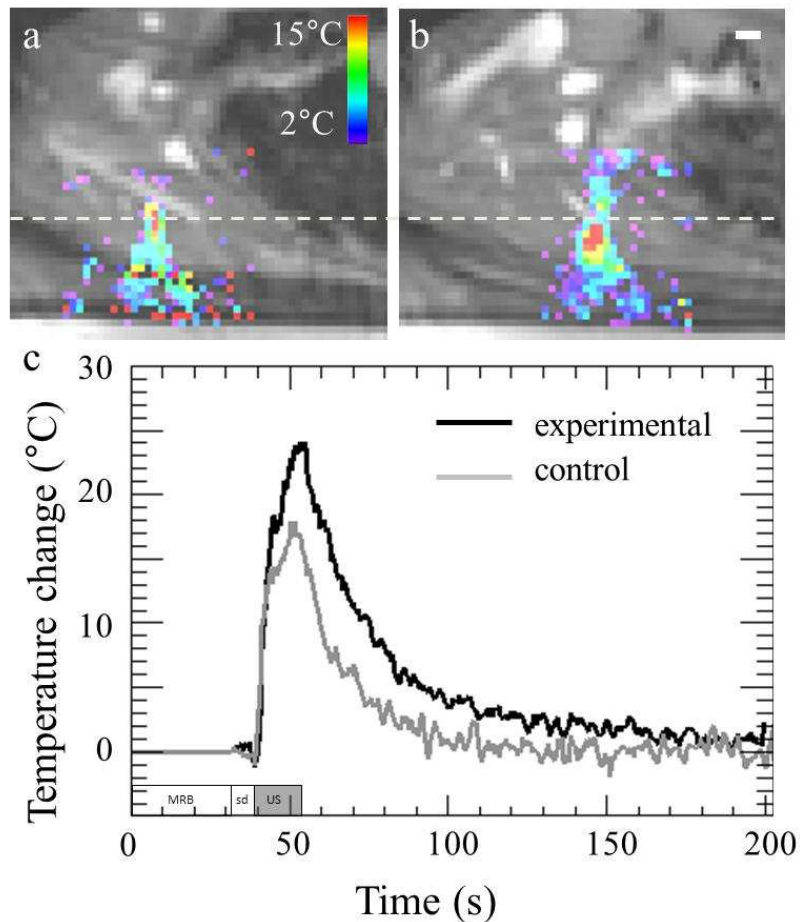


Figure II.8: representative MR-thermometry data for the control and experimental groups. MR-thermometry images displayed in (a) and (b) show the temperature distributions (color coded and overlaid on magnitude grey scale image) at the end of the sonication for both conditions. The color scale for temperature values is indicated in (a). The horizontal white dashed lines indicate the targeted depth. The white line on the top right part of image (b) represents 10 mm. Graph (c) plots the temperature evolution in the pixel displaying maximal temperature increase for the control (grey curve) and experimental (black curve) sonications. The images selected for motion correction with the multi-reference baseline (MRB rectangle), for the estimation of the temperature standard deviation (sd rectangle) and the duration of the HIFU sonication (US grey rectangle) are indicated on (c).

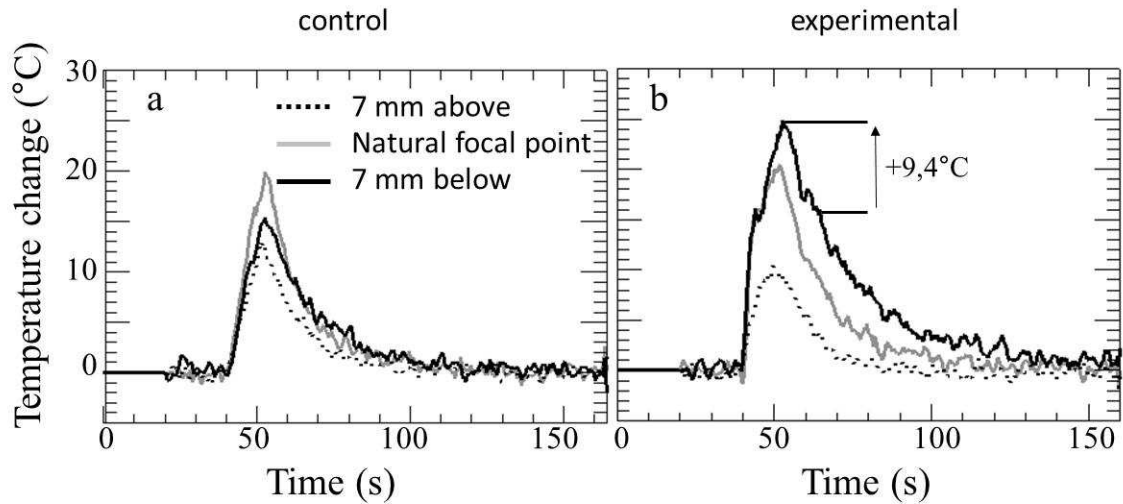


Figure II.9: Comparison of temperature evolution for control (a) and experimental (b) sonications. For each condition, the temperature evolution at natural the focal point (solid grey line), 7mm below (solid black line) and 7mm above (black dashed line) are plotted. The black vertical arrow in (b) shows the increase in temperature in the near field.

Figure II.9 plots the temperature evolution in three voxels centred on the natural focal point for both groups. For the control group (Figure II.9a), the maximal temperature increase reached 20°C and was located at the natural focal point. For the experimental group (Figure II.9b), the temperature at the focal point was similar, but the maximal temperature increase reached 25°C (+9.4°C as compared to the same voxel in the control experiment) 7mm below the natural focal point, whereas the maximal temperature increase at 7 mm above the focal point was 10°C (-2.7°C as compared to the same voxel in the control experiment).

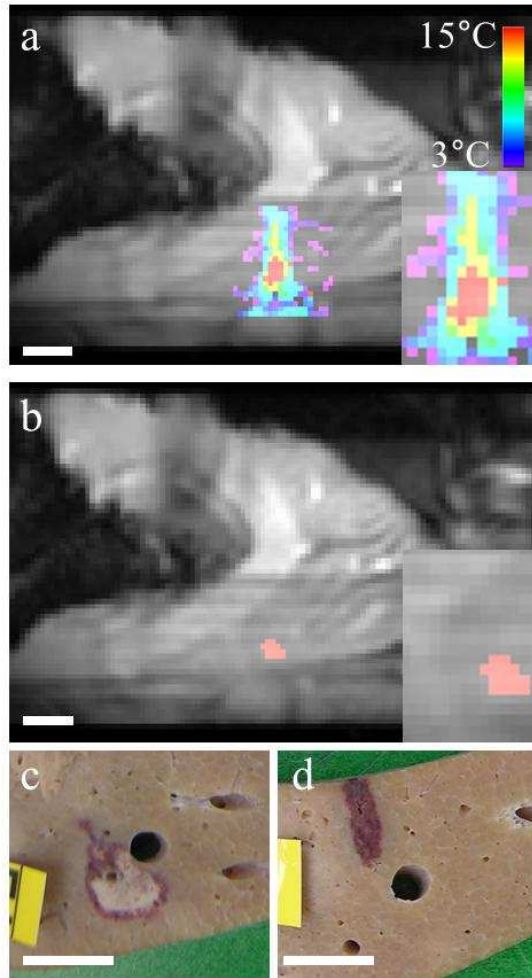


Figure II.10: Representative MR temperature data sets of the experimental group and comparative macroscopic analysis of explanted livers for both conditions. Colour coded MR-temperature image (a) obtained at the end of the sonication overlaid to magnitude image (grey scale). The colour scale is indicated on the top right. The insert in the bottom right part shows a zoomed (x2) view centred on the heated region. The accumulated thermal dose image obtained after cooling of the tissue is displayed in (b). The pixels for which the thermal dose is higher or equal to the CEM43 are coloured in red. The insert shows the zoomed (x2) view centred on the same pixel as in (a). Photographs of the macroscopic slices after fixation of the liver tissues for sonications of the experimental (c) and control (d) groups. The horizontal white bar on each image represents 10 mm.

Figure II.10 displays the complete data set using sonication protocol of the experimental group, including the temperature image at the end of the sonication (a), the accumulated thermal dose after tissue cooling (b) and a photograph of the macroscopic view of the tissue sample after fixation (c). Temperature increases of 15°C or more (red colour) show a nearly circular pattern, whereas the temperature increase of 12°C (in yellow) shows a tadpole shape with the tail located in the far field. The accumulated thermal dose shows a near circular lesion comprising of 14 pixels (8.3 mm maximal width and height), without an apparent tail. The corresponding liver lesion after fixation (Figure II.10c) showed macroscopically a circular white zone of 8 mm diameter surrounded by a thin purple rim extending at one-end by a small tail. The control sonication resulted in an exclusively purple elliptic lesion (Figure II.10d) with long and short axis lengths of 10 and 3 mm, respectively. The microscopic analysis of both samples (data not shown) confirmed the presence of a sharp boundary between treated and untreated tissues. The control sonication led to a diffusely haemorrhagic area with little architectural distortion but without liver cell necrosis. In contrast, the experimental sonication led to a central necrotic area (white macroscopic zone previously described) characterized by ghost-cell islands. A haemorrhagic strip with viable hepatocytes surrounded the central area.

Table II.2 summarizes the maximal temperature increases values measured by MR thermometry for sonications at 20 mm depth in the liver, for control and experimental sonications performed with a burst pulse of 600Wac (E_{600}). For the control group, the temperature increase ranged between 15 and 22°C with a mean (\pm standard deviation) value of 17.6 ± 2.8 °C. For the experimental group, the temperature increase ranged between 18 and 32°C (24.3 ± 4.3 °C). The mean gain in temperature increase at constant energy deposition was 40 ± 14 %. Lesions were identified on the macroscopic slices and revealed a white central part surrounded by a thin red region, similar to the data presented in Figure II.10c. The shape

of the lesions appeared nearly circular, with a length and width of 6.25 ± 1.26 mm (ranging from 5 to 8 mm) and 5.5 ± 1.29 mm (ranging from 4 to 7 mm).

| Tmax [°C] | | Gain |
|-------------------|------------------------|--------------------|
| Control | E₆₀₀ | |
| 21 | 32 | 1.52 |
| 22 | 29 | 1.32 |
| 16.5 | 26 | 1.58 |
| 15 | 18 | 1.2 |
| 15 | 21 | 1.4 |
| 16 | 24 | |
| | 23.5 | |
| | 21 | |
| 17.6 ± 2.8 | 24.3 ± 4.3 | 1.40 ± 0.14 |

Table II.2: Maximal temperature increases for the 14 sonications at acoustic energy of 1800 J performed in the liver at a depth of 20 mm for the control (N=6) and experimental (E₆₀₀ stands for 600 W acoustic power of the 0.5 sec pulse, N=8) groups, respectively. The first 5 lines compare sonications performed sequentially at close locations in the liver (less than 1 cm distance in the horizontal direction), whereas the last 5 experiments were not paired in position with the other condition. The column Gain gives the ratio between maximal temperatures of groups (E) and (C). The last line of the table indicates the mean and standard deviation for each corresponding column.

Table II.3 presents the maximal temperature increases measured by MR-thermometry in the liver at a sonication depth of 25 mm. Control and E₆₀₀ sonications resulted in similar temperature increases (mean values of 12.3°C and 13°C, respectively), resulting in negligible

gain (less than 10%). Sonications performed with a burst pulse of 800 W (E_{800}) led to substantial temperature increases (75% and 155%) with a mean temperature increase of 27.5 ± 1.5 °C, a shift of the maximal value toward the transducer and circular shape on the sagittal MR temperature slice. The macroscopic analysis of the liver samples for the three sonications of the E_{800} group revealed a near circular thermal lesion (displaying white and red zones) with lengths and widths of 8.33 ± 1.53 mm and 8 ± 1 mm, respectively.

The mean ($\pm\sigma$) shift in position of the maximal temperature increase between the control and experimental sonication pairs at equivalent depth (5 first rows in Table II.2 for E_{600} , and rows 3 and 4 in Table II.3 for E_{800}) was 7.4 ± 1.9 mm.

| Tmax [°C] | | | Gain |
|----------------------------------|--------------------------------|----------------------------------|-----------------------------------|
| Control | E_{600} | E_{800} | |
| 7 | 8 | | 1.14 |
| 15 | 15 | | 1 |
| 16 | 16 | 28 | 1 (1.75) |
| 11 | 13 | 28 | 1.18 (2.55) |
| | | 25 | |
| | | 29 | |
| 12.3 ± 3.6 | 13 ± 3.1 | 27.5 ± 1.5 | 1.08 ± 0.08 |

Table II.3: Maximal temperature increases for the 11 sonications at acoustic energy of 1800 J performed in the liver at a depth of 25 mm for the control (N = 4) and experimental groups, with 0.5 sec pulse power of 600W (E_{600} , N = 4) and 800W (E_{800} , N = 4), respectively. The column Gain gives the ratio between maximal temperatures of groups (E_{600}) and (C), with the last two values given in parenthesis corresponding to ratio (E_{800}/C). The last line of the table indicates the mean and standard deviation for each corresponding column. For the gain, only the ratio E_{600}/C were considered in the statistics (N=4).

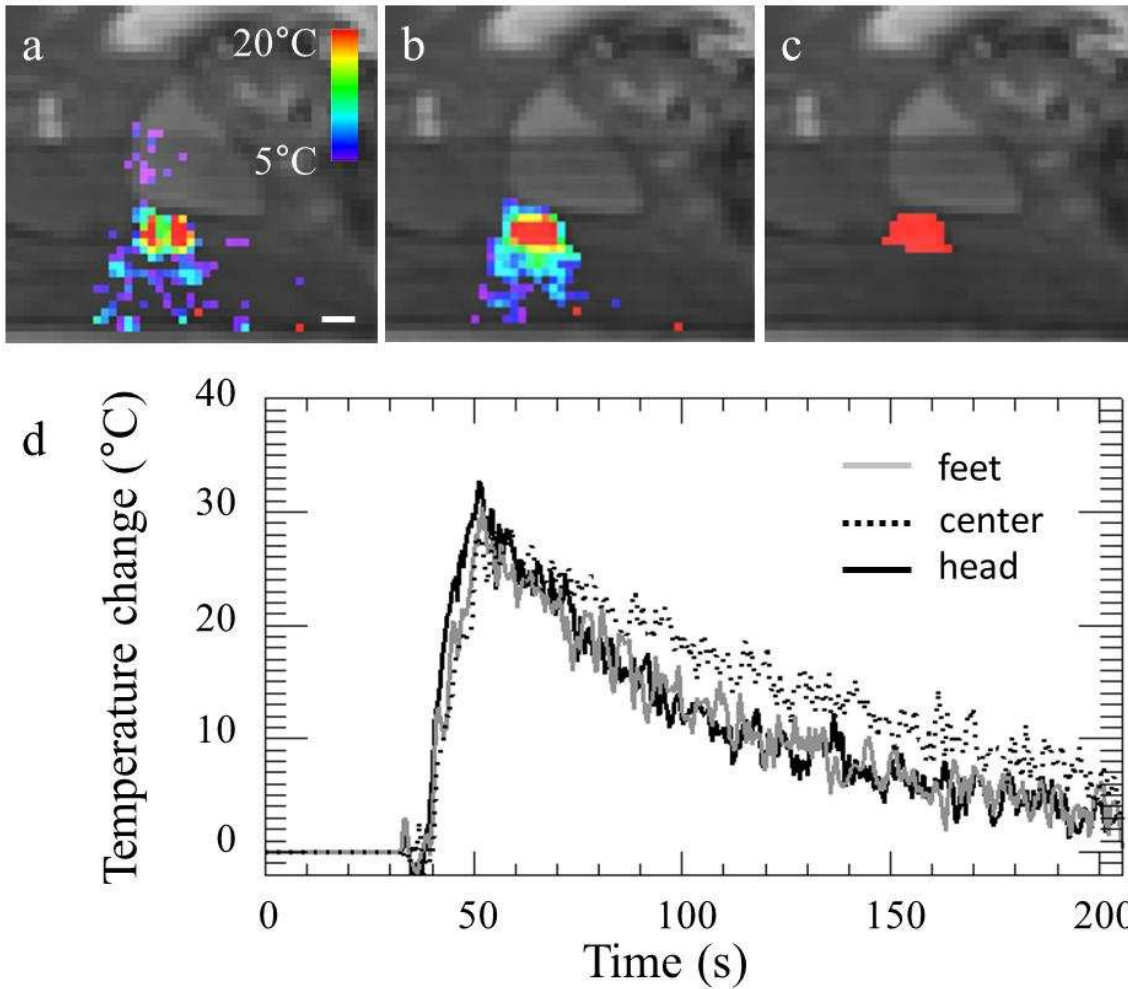


Figure II.11: MR temperature data for sonication performed in the liver with dual targeted points. Temperature images obtained after 15 sec (a) HIFU exposition and at the end of the sonication (b). The 10 mm scale (horizontal white line) and colour code for temperature are indicated in (a). The accumulated thermal dose image at the end of the MR-thermometry acquisition (150 sec after the end of the sonication) is displayed in (c). The graph in (d) plots the temperature evolution in the hottest pixels corresponding to each focal point position (solid grey curve -feet position- and black solid curve -head position-, respectively) and in the pixel located at the central position (dashed dot).

Figure II.11 shows temperature data set corresponding to a sonication performed at two positions separated by a horizontal distance of 10 mm that were targeted by electronic deflection of the HIFU beam in the head-feet direction, at 20 mm depth in the liver. The 0.5 sec pulse was split into 100 individual pulses and each location was alternatively targeted every 5 ms at 600 W acoustic power. The second pulse was iteratively targeted (each 5 ms) toward the same locations for a total duration of 13.5 sec at an acoustic power of 200 W, leading to a total energy deposition of 3 kJ. The two distinct temperature spots visible on Figure II.11a progressively merged to a spatially uniform temperature distribution (Figure II.11b), displaying a nearly elliptic shape with the long axis oriented perpendicular to the HIFU propagation direction. The resulting thermal dose map (Figure II.11c) was also elliptic with horizontal and vertical lengths of 16.5 and 11.5 mm, respectively. The macroscopic analysis of the liver sample showed an elliptic lesion with length and width of 15.5 and 9 mm. The graph in Figure II.11d shows the temperature evolution at the hottest point for each targeted location and at the central position. The maximal temperature increase was nearly identical at each location (30°C). The cooling time required to return to half of this value was 40 sec for each targeted point and 60 sec for the central position.

5. Discussion

In our study, we propose to exploit online, motion-compensated MR thermometry for the evaluation of the acoustic power threshold required for observing modification of the temperature distribution at the vicinity of the focal point. With this non invasive method, acoustic power threshold values of 600 to 800 W were determined for sonication depths ranging between 20 to 25 mm in the liver parenchyma. This increase in acoustic power with sonication depths was expected to compensate for the attenuation of the ultrasound intensity by tissues. More precise calibration of pulse characteristics (duration and power) as a function of the tissue type and sonication depth appeals for more sophisticated methods, such as acoustic spectral analysis (Hsieh et al., 2011, McLaughlan et al., 2010), ultrasound imaging of cavitation (Gyongy and Coussios, 2010) or ultrasound- or MRI-based Acoustic Radiation Force Imaging methods (Nightingale et al., 2002, McDannold and Maier, 2008, Chen et al., 2010).

In this current study, the temperature distribution changed from an ellipsoid to a nearly circular shape ('tadpole') using burst pulse with sufficient acoustic power, as already reported in previous studies (Khokhlova et al., 2009, Sokka et al., 2003, Chavier et al., 2000). The shift of the location of the maximal temperature was 7 mm toward the transducer (with similar values for threshold determination and for the experimental group), in strong agreement with previously published data (Zderic et al., 2008, Khokhlova et al., 2009) (Sokka et al., 2003). With regards to the spatial resolution of the in-plane MR acquisition sequence (2.34 mm), the precision of the determination of the shift should be interpreted as ranging between 5 to 9 mm (approximately 2 to 4 pixels). The macroscopic analysis of the explanted liver samples revealed haemorrhagic lesions for sonications of the control group and confirmed the presence of tadpole shaped thermal lesions from sonications in the

experimental group. The near circular temperature distribution is beneficial in terms of thermal dose accumulation since the heat diffusion is more isotropic than for conventional sonications, slowing down the cooling of tissues. To enlarge thermal lesions (greater than the size scale of focal point), strategies based on continuous sonications with electronic deflection of the focal point have been proposed using different trajectories (e.g. spiral (Mougenot et al., 2004) and concentric circles (Kohler et al., 2009)), exploiting the thermal diffusivity for creating a homogenous volumetric heating while reducing the total energy deposition. However, the resulting lesions remain ellipsoidal in shape with the long axis aligned with the ultrasound propagation. As a consequence, the maximal transverse size of the trajectory must be carefully selected to avoid expansion of thermal damages in the near field and far field. Sonications with enhanced heating, combined with multiple targeted points using fast electronic deflection of the HIFU beam may be exploited (Inaba et al., 2011). This is suggested by data presented in Figure II.11, where the resulting thermal lesion was more elongated in the direction orthogonal to the ultrasound propagation axis. These results are in a good agreement with those reported by Inaba (Inaba et al., 2011).

More sophisticated sonications could be planned where a number of selected locations may be pre-defined and targeted with short burst sonications at sufficient acoustic power in order to delineate the desired outer limit of the sonication field (shielding effect, mentioned Zderic (Zderic et al., 2008)).

The maximal temperature rise in the experimental group was increased by approximately 40% as compared to the control group. Sokka *et al* (Sokka et al., 2003) reported shorter temperature rise times within the first 4 seconds of sonication following a short 0.5 sec burst ultrasound pulse, resulting in a net increase in maximal temperature up to a factor of 2 as compared to control sonications. However, the temperature curves presented in their article were spatially averaged over 9 voxels, which may affect the precision of the estimate of the

gain in temperature since the spatial distribution of heating was different for both conditions. Moreover, tissue perfusion is expected to be higher in the liver than in the muscle, leading to a more efficient heat evacuation and lower gain in temperature increase. Experimental sonications performed below the threshold (e.g. results from E_{600} experiments in Table II.3) resulted in maximal temperature increases and elliptical shapes identical to those of the control group. This result was expected since both sonications had identical total energy.

Besides the gain in temperature, another beneficial effect of experimental sonications is the reduction of the temperature increase (~30%) in the post focal region. This effect is particularly advantageous for the treatment of abdominal organs where air-filled structures (stomach, bowels, lungs...) or heart may be at the vicinity of the targeted region. Zderic et al (Zderic et al., 2008) also reported attenuated temperature increases in post focal regions at tissue-air interface of rabbit muscle and liver using similar strategies. Therefore, thermal ablation of pathological tissues using sonication closer to sensitive structures may be considered, improving the treatment capabilities of current clinical applications of MR guided HIFU such as for uterine fibroid.

In conclusion, the present study demonstrates *in vivo* in the liver the feasibility of using MR thermometry for 1) planning the acoustic power threshold to induced BEH, 2) characterizing the gain in heating efficiency in presence of BEH.

6. References

- Chavrier, F., Chapelon, J.Y., Gelet, A., Cathignol, D., 2000. Modeling of high-intensity focused ultrasound-induced lesions in the presence of cavitation bubbles. *The Journal of the Acoustical Society of America* 108, 432.
- Chen, J., Watkins, R., Pauly, K.B., 2010. Optimization of encoding gradients for MR-ARFI. *Magn. Reson. Med.* 63, 1050–1058.
- Chen, W.-S., Matula, T.J., Brayman, A.A., Crum, L.A., 2003. A comparison of the fragmentation thresholds and inertial cavitation doses of different ultrasound contrast agents. *The Journal of the Acoustical Society of America* 113, 643.
- Clarke, R.L., ter Haar, G.R., 1997. Temperature rise recorded during lesion formation by high-intensity focused ultrasound. *Ultrasound in Medicine & Biology* 23, 299–306.
- Coussios, C. C., Farny, C.H., Ter Haar, G., Roy, R.A., 2007. Role of acoustic cavitation in the delivery and monitoring of cancer treatment by high-intensity focused ultrasound (HIFU). *Int J Hyperthermia* 23, 105–120.
- de Senneville, B.D., Mougenot, C., Moonen, C.T.W., 2007. Real-time adaptive methods for treatment of mobile organs by MRI-controlled high-intensity focused ultrasound. *Magnetic Resonance in Medicine* 57, 319–330.
- Ebbini, E.S., Yao, H., Shrestha, A., 2006. Dual-mode ultrasound phased arrays for image-guided surgery. *Ultrason Imaging* 28, 65–82.

- Gyöngy, M., Coussios, C.-C., 2010. Passive cavitation mapping for localization and tracking of bubble dynamics. *The Journal of the Acoustical Society of America* 128, EL175.
- Hazle, J.D., Diederich, C.J., Kangasniemi, M., Price, R.E., Olsson, L.E., Stafford, R.J., 2002. MRI-guided thermal therapy of transplanted tumors in the canine prostate using a directional transurethral ultrasound applicator. *Journal of Magnetic Resonance Imaging* 15, 409–417.
- Hockham, N., Coussios, C.C., Arora, M., 2010. A real-time controller for sustaining thermally relevant acoustic cavitation during ultrasound therapy. *Ultrasonics, Ferroelectrics and Frequency Control, IEEE Transactions on* 57, 2685 –2694.
- Holt, R.G., Roy, R.A., 2001. Measurements of bubble-enhanced heating from focused, mhz-frequency ultrasound in a tissue-mimicking material. *Ultrasound in Medicine & Biology* 27, 1399–1412.
- Hsieh, C., Probert Smith, P., Mayia, F., Ye, G., 2011. An Adaptive Spectral Estimation Technique to Detect Cavitation in HIFU With High Spatial Resolution. *Ultrasound in Medicine & Biology* 37, 1134–1150.
- Hynynen, K., 1991. The threshold for thermally significant cavitation in dog's thigh muscle in vivo. *Ultrasound in Medicine & Biology* 17, 157–169.
- Inaba, Y., Tatsuya, M., Yoshizawa, S., Umemura, S., 2011. Ultrasonic coagulation of large tissue region by generating multiple cavitation clouds in direction perpendicular to ultrasound propagation. *Japanese Journal of Applied Physics* 50.

- Khokhlova, T.D., Canney, M.S., Lee, D., Marro, K.I., Crum, L.A., Khokhlova, V.A., Bailey, M.R., 2009. Magnetic resonance imaging of boiling induced by high intensity focused ultrasound. *Journal of the Acoustical Society of America* 125, 2420–2431.
- Köhler, M.O., Mougnot, C., Quesson, B., Enholt, J., Le Bail, B., Laurent, C., Moonen, C.T.W., Ehnholm, G.J., 2009. Volumetric HIFU ablation under 3D guidance of rapid MRI thermometry. *Medical Physics* 36, 3521.
- Liu, H.-L., Chen, W.-S., Chen, J.-S., Shih, T.-C., Chen, Y.-Y., Lin, W.-L., 2006. Cavitation-enhanced ultrasound thermal therapy by combined low- and high-frequency ultrasound exposure. *Ultrasound in Medicine & Biology* 32, 759–767.
- Liu, H.-L., McDannold, N., Hynynen, K., 2005. Focal beam distortion and treatment planning in abdominal focused ultrasound surgery. *Medical Physics* 32, 1270.
- Macé, E., Cohen, I., Montaldo, G., Miles, R., Fink, M., Tanter, M., 2011. In Vivo Mapping of Brain Elasticity in Small Animals Using Shear Wave Imaging. *IEEE Transactions on Medical Imaging* 30, 550–558.
- McDannold, N., Maier, S.E., 2008. Magnetic resonance acoustic radiation force imaging. *Med. Phys.* 35, 3748.
- McLaughlan, J., Rivens, I., Leighton, T., ter Haar, G., 2010. A Study of Bubble Activity Generated in Ex Vivo Tissue by High Intensity Focused Ultrasound. *Ultrasound in Medicine & Biology* 36, 1327–1344.
- Mougnot, C., Salomir, R., Palussière, J., Grenier, N., Moonen, C.T.W., 2004. Automatic spatial and temporal temperature control for MR-guided focused ultrasound

using fast 3D MR thermometry and multispiral trajectory of the focal point. *Magnetic Resonance in Medicine* 52, 1005–1015.

Nightingale, K., Soo, M.S., Nightingale, R., Trahey, G., 2002. Acoustic radiation force impulse imaging: in vivo demonstration of clinical feasibility. *Ultrasound in Medicine & Biology* 28, 227–235.

Owen, N.R., Chapelon, J.Y., Bouchoux, G., Berriet, R., Fleury, G., Lafon, C., 2010. Dual-mode transducers for ultrasound imaging and thermal therapy. *Ultrasonics* 50, 216–220.

Quesson, B., de Zwart, J.A., Moonen, C.T.W., 2000. Magnetic resonance temperature imaging for guidance of thermotherapy. *Journal of Magnetic Resonance Imaging* 12, 525–533.

Quesson, B., Laurent, C., Maclair, G., de Senneville, B.D., Mougnot, C., Ries, M., Carteret, T., Rullier, A., Moonen, C.T.W., 2011. Real-time volumetric MRI thermometry of focused ultrasound ablation in vivo: a feasibility study in pig liver and kidney. *NMR in Biomedicine* 24, 145–153.

Quesson, B., Merle, M., Köhler, M.O., Mougnot, C., Roujol, S., de Senneville, B.D., Moonen, C.T., 2010. A method for MRI guidance of intercostal high intensity focused ultrasound ablation in the liver. *Med. Phys.* 37, 2533.

Rieke, V., Butts Pauly, K., 2008. MR thermometry. *Journal of Magnetic Resonance Imaging* 27, 376–390.

- Sapareto, S.A., Dewey, W.C., 1984. Thermal dose determination in cancer therapy. *International Journal of Radiation Oncology*Biology*Physics* 10, 787–800.
- Sokka, S.D., Gauthier, T.P., Hynynen, K., 2005. Theoretical and experimental validation of a dual-frequency excitation method for spatial control of cavitation. *Physics in Medicine and Biology* 50, 2167–2179.
- Sokka, S.D., King, R., Hynynen, K., 2003. MRI-guided gas bubble enhanced ultrasound heating in in vivo rabbit thigh. *Phys Med Biol* 48, 223–241.
- Tu, J., Matula, T.J., Brayman, A.A., Crum, L.A., 2006. Inertial cavitation dose produced in ex vivo rabbit ear arteries with optison® by 1-mhz pulsed ultrasound. *Ultrasound in Medicine & Biology* 32, 281–288.
- Wu, F., Wang, Z.-B., Chen, W.-Z., Wang, W., Gui, Y., Zhang, M., Zheng, G., Zhou, Y., Xu, G., Li, M., Zhang, C., Ye, H., Feng, R., 2004a. Extracorporeal high intensity focused ultrasound ablation in the treatment of 1038 patients with solid carcinomas in China: an overview. *Ultrasonics Sonochemistry* 11, 149–154.
- Wu, F., Wang, Z.-B., Chen, W.-Z., Wang, W., Gui, Y., Zhang, M., Zheng, G., Zhou, Y., Xu, G., Li, M., Zhang, C., Ye, H., Feng, R., 2004b. Extracorporeal high intensity focused ultrasound ablation in the treatment of 1038 patients with solid carcinomas in China: an overview. *Ultrasonics Sonochemistry* 11, 149–154.
- Zderic, V., Foley, J., Luo, W., Vaezy, S., 2008. Prevention of post-focal thermal damage by formation of bubbles at the focus during high intensity focused ultrasound therapy. *Med. Phys.* 35, 4292.

III. TRANSCOSTAL HIFU

Contribution: Delphine Elbes, Sébastien Roujol, Bruno Quesson

1. Introduction

One of limitation in focusing ultrasound in the heart or liver remains the presence of rib cage (Figure III.1). Firstly, the rib cage acts as an aberrator reducing the focusing quality. Secondly, the high value of absorption of the bones (Goss et al. 1979) induces undesirable heating of bones and in surrounding tissues (Quesson et al. 2010). Thirdly, reflexions of ultrasound by bones can result in constructive interferences in the surrounding tissues and energy deposition on the transducer surface.

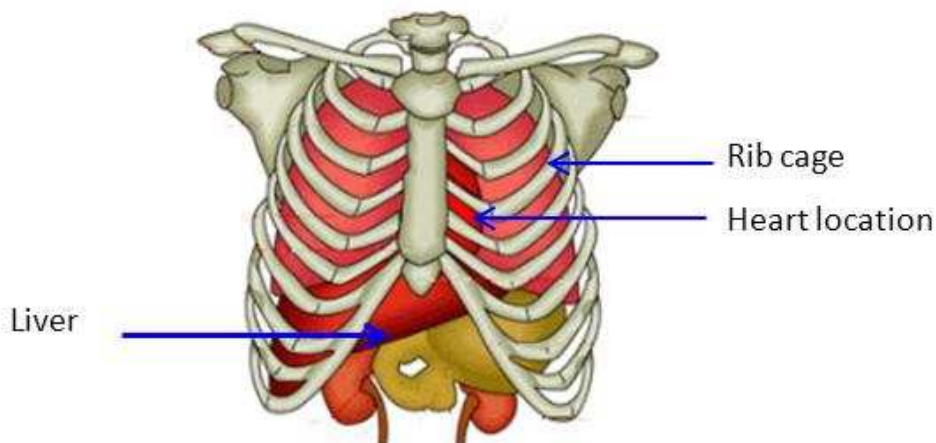


Figure III.1: anatomical diagram of organs located inside the rib cage

Several groups have investigated the possibility to perform liver ablation by HIFU. Daum (Daum et al. 1999) reported a temperature increase on the ribs five times higher than in intercostals tissues. Wu (Wu et al. 2004) reported skin burn at locations close to the rib cage. As they were using a single element transducer, they proposed to remove a section of rib above the liver to overcome this problem. However, this solution makes ineffective non invasive aspect of HIFU treatment.

The development of transducer arrays was a step forward to develop new strategies to perform HIFU in the liver while reducing heating of the ribs (McGough et al. 1996, Botros et al. 1997, Botros et al. 1998). An efficiency solution to reduce the overheating of the rib cage and to improve the focusing quality is time reversal focusing (Fink 1992, Aubry et al. 2008). A hydrophone was placed at the focal point of the transducer arrays. The ultrasound emission of each transducer elements was recorded by the hydrophone. If there was a small source at the focal point, the set of data received by each element would be the same recorded at the focal point from each element by the hydrophone according to the spatial reciprocity. As a consequence, the wave front received by the hydrophone was time reversed and reemitted by the transducer arrays. The advantage of this method is an instantaneous measurement of the wave front. However, this technique remained invasive because of the hydrophone had to be placed at the focal point. Aubry *et al.* (Aubry et al. 2008) have demonstrated the feasibility and the efficiency of time reversal imaging on *ex vivo* rib cage. They improved focusing quality by 1.73 dB and reduced significantly the heating near the ribs 0.3°C instead of 5.9°C. They also showed that in absence of sparing ribs the defocusing was negligible. For transcranial application, a non invasive version of time reversal focusing has been developed by Marquet *et al.* (Marquet et al. 2009) *ex vivo*. The data set recorded by the hydrophone was replaced by acoustic simulations. These simulations were obtained from CT images which gave the possibility to simulate the acoustic propagation taking into account the skull. The

simulation signals were time reversed and emitted by the arrays. In term of efficiency, this technique maintained about 80 % of the acoustic energy obtained with the hydrophone guided time reversal focusing. Without any correction, this ratio was near 75%. Although this technique is non invasive and efficient, it remained difficult to be translated to transcostal focusing *in vivo* because of the potential movement of rib cage during the respiration, the required duration of simulations, and resuirement of 3D Xray data. Other methods based on simulations have been proposed (Pinton et al. 2012), but the computational time (30 hours) remained incompatible with real time correction. For transcranial application, a non invasive method, based on MR-ARFI at the focal point, has been develop (Marsac et al. 2012). Phase arrays were adapted to maximise the acoustic intensity at the focal point. The adaptation was based on the measurement of the local displacement at the focal point induced by pulsed HIFU. Again, the acquisition duration 2 hours remained too long for practical application to the rib.

Another family of methods to spare ribs during HIFU treatment was switching off transducer elements located in front of the rib so called binarized apodization law, initially proposed numerically by Liu et al (Liu et al. 2007) and demonstrated experimentally *in vivo* by Quesson et al. (Quesson et al. 2010). Cochard et al (Cochard et al. 2011) have developed a technique based on the analysis of the backscattered signal toward the transducer to identify the list of transducer elements to deactivate. Although this method was non invasive and required only one back-scattered echo from the ribs, experiments realized in water tank has not yet evaluated *in vivo*. More recently, Marquet *et al.* (Marquet et al. 2011) have studied a deactivation method on *ex vivo* liver in presence of simulated respiratory motion. Using beam steering, heating became more efficient with motion correction adapted to the respiratory movement. Moreover, the lesion was enlarged by using spiral trajectory (Salomir et al. 2000). According to their simulation, an update of the apodization law was not necessary below a

distance from the natural focal of 1 cm. Simulations showed that heating remained in the rib, but below the lethal thermal dose. This method resulted in large lesion with motion correction and no lesion in absence of ultrasound target tracking. However, for steering amplitude higher than 1cm, the method appeared ineffective and justified improvements. Then, the lethal thermal dose was not measured at the rib location, and, no lesion could be observed, in area surrounded ribs, when 1 or 1.5 cm beam steering was employed, because of ribs were in a gel. Moreover, in *in vivo* experiments, the acoustic power required for to induce the same type of lesion will be higher because of perfusion, and therefore the temperature increase at the ribs location could reach more easily the lethal thermal dose. Recently, a technique that consisted to insert reflective strips between the transducer and the rib cage was developed. Although this method remained equivalent to binarized apodization law in terms of temperature increase at the focal point and at the rib location, the practical application on humans seems more difficult and longer than binarized apodization law. Moreover, the impact of reflective strips on the transducer was not investigated. The aims of the following study were 1) to investigate the beam steering through the ribs cage under MR thermometry, 2) to quantitatively study the usefulness of updating the binarized apodization law when beam steering was used in the same range as respiratory motion amplitude.

2. Material and methods

Experiments were performed at 1.5 T MRI (Achieva, Philips, The Netherlands) with the Sonalleve MR-HIFU platform (Philips Healthcare, Vantaa, Finland) designed for the treatment of uterine fibroids (see (Kohler et al. 2009) for technical description of the device). All sonications were performed at a frequency of 1.2 MHz on a phantom : a cylindrical agarose-silicon gel (2% agarose 3% silicon) gel with an inclusion of two pig ribs removed from meat (figure III.2).

a. MR Sequences

The localisation of the targeted focal point and bones were performed by using a 3D proton-density weighted fast gradient echo sequence acquired prior to sonications. The sequence characteristics were TE/TR =4.6/8.57 ms, 350 x 350 x 180 mm³ FOV, matrix 192 x 192 x 60, 1.82 x 1.82 x 3 mm³ voxel size, a 15° water selective binomial pulse. The reconstructed volume was analyzed via home made software allowing multiplanar visualization in the transverse, sagittal and coronal orientations, for : localization and segmentation of bones, the location of the targeted focal point, and calculation of the list of transducer elements to deactivate using geometric projection of the shadow of the bones at the surface viewed from the focal point.

MR thermometry was performed by using the Proton Resonant Frequency (PRF) shift method using a multishot Echo Planar Imaging (EPI) sequence, with the following acquisition parameters : echo train length of 7, TE/TR=12/200 ms, 200 x 200 mm FOV, matrix 100 x 98, 20 ° flip angle, 3 adjacent slices of 2.5 mm thickness positioned in vertical orientation. Temperature images were calculated (PRF constant of 0.0094 ppm.°C⁻¹) and displayed with

in-house developed software (“RealTI”) written in C++ and IDL (ITT, Visual Information Solutions).

b. Sonication protocol

The binarized apodization law, used in this study, consisted on the deactivation of transducer elements covered by minimum 50% of the shadow of the rib.

First batch of experiments were similar to those presented by Quesson (Quesson et al. 2010). The targeted heating area was located at the natural focal point. The case with all elements activated and binarized apodization law were compared. When all transducer elements were activated, the acoustic power was 100 W and the sonication duration was 30 s.

Secondary, electronic deflection was used to focus at 7 mm left and right around the focal point (figure III.2) since 15 mm was considered in the range of the amplitude of respiratory movement. Two binarized apodization laws were compared for the new location. The first binarized apodization law consisted in keeping the same elements deactivated as for the natural focal point. For the second binarized apodization law, the geometric projection of the ribs on the transducer from the new targeted location was calculated to update the list of elements to deactivate. In the manuscript the first law is called initial law and the second law updated law. Target points, focused by using electronic deflection, were localized at the same depth.

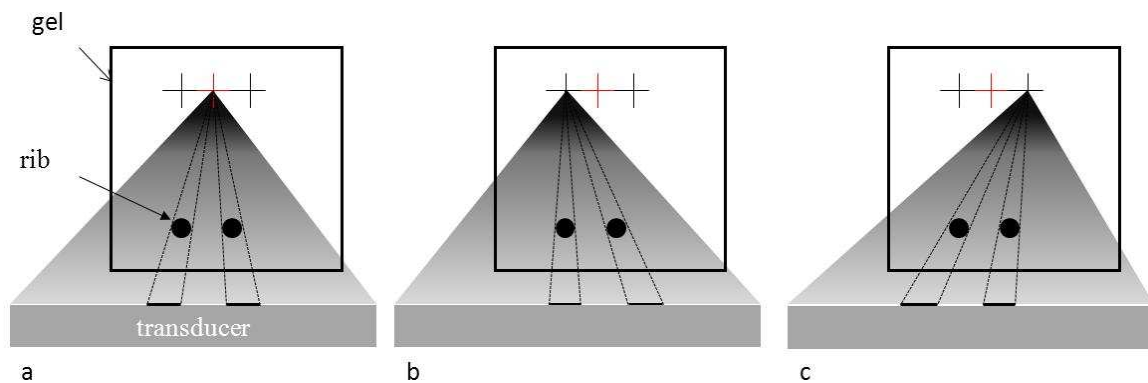


Figure III.2: binerazed apodization law combined with beam steering for three positions: at the natural focal point (a), 7 mm left of the focal point, 7 mm right of the natural focal point. Crosses symbolise the three targeted locations, the red one the natural focal point. The grey triangle symbolizes the ultrasound cone. Dashed lines indicate the projection cone of the shadow of the ribs on the transducer. The horizontal black lines show the shadow of bones projected on the transducer surface.

c. Data analysis

MR temperature maps were computed and temperature images at the end of sonication were displayed. Pixels, with a low SNR on modulus images in the ribs, were masked out in temperature images. Temperature evolutions, at the targeted focal point and near the ribs, were analysed.

3. Results

Figure III.3 compares data sets obtained for a sonication at the natural focal point. With all elements turned on, the maximal temperature increase was 36°C at the focal point and 24°C close to the ribs. With the initial law, the maximal temperature increase at the focal point was 31°C and 8°C close to the ribs.

Figure III.4 compares initial law and updated law for ultrasounds focused 7 mm at the right of the natural focal point, using electronic deflection. With the initial law, maximal temperature increase at the focal point was 19°C and 17°C close to the ribs. With the updated law, maximal temperature increase at the focal point was higher (28°C) and lower close to the ribs (9°C).

Figure III.5 compares initial law and updated law for ultrasounds focused 7 mm at the left of the natural focal point, using electronic deflection. With the initial law, maximal temperature increase at the focal point was 20°C and 8°C close to the ribs. With the updated law, maximal temperature increase at the focal point was higher (26°C) and in the same range close to the ribs (7°C).

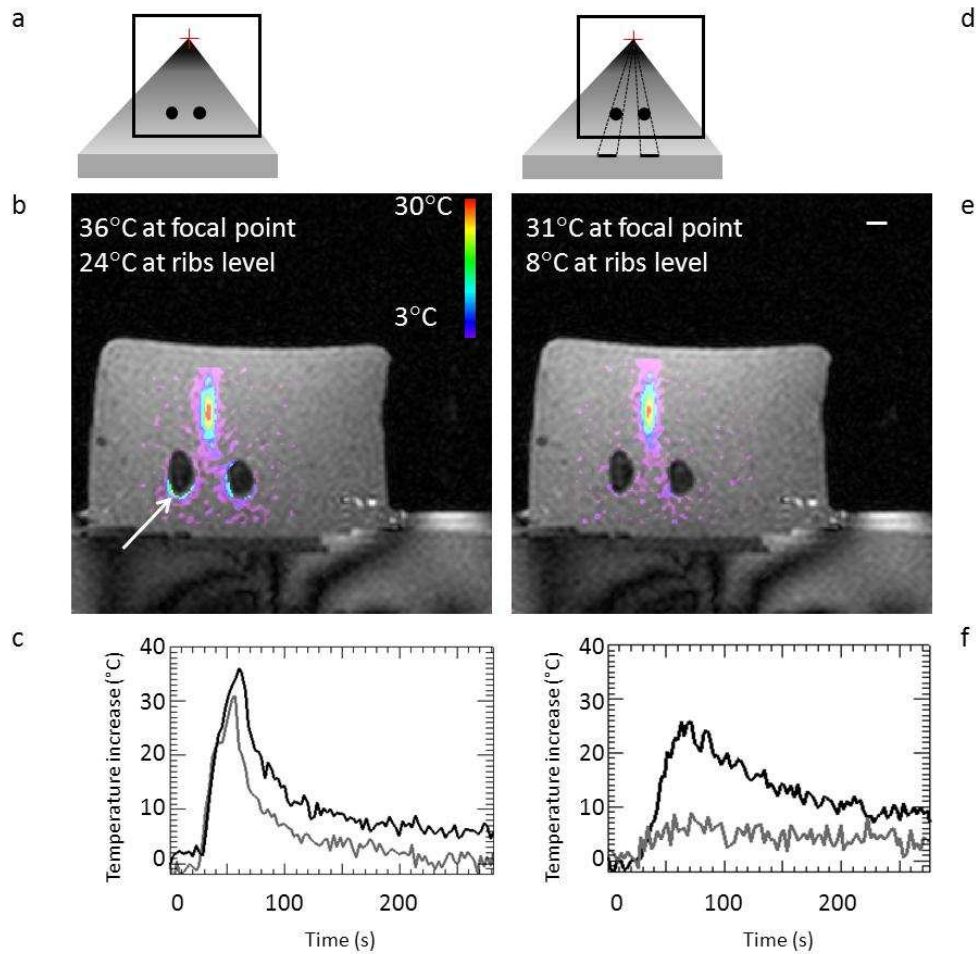


Figure III.3: Comparison of heating sonication through the ribs at the natural focal point without (a) (b) and with a binarized apodization law (d) (e). Diagram at the top represents the method used to focus ultrasound with the corresponded temperature maps overlaid on modulus images below. The horizontal white bar on image (e) represents 10 mm. The colour scale for the temperature maps is indicated in b. Graph (c) compares the temperature evolution at the focal point and graph (f) at the ribs level (see white triangle image(c)). Black curves correspond to sonication with all elements activated, grey curves to the case with initial law. The white arrow (b) indicates the maximal temperature increase at the rib cage level.

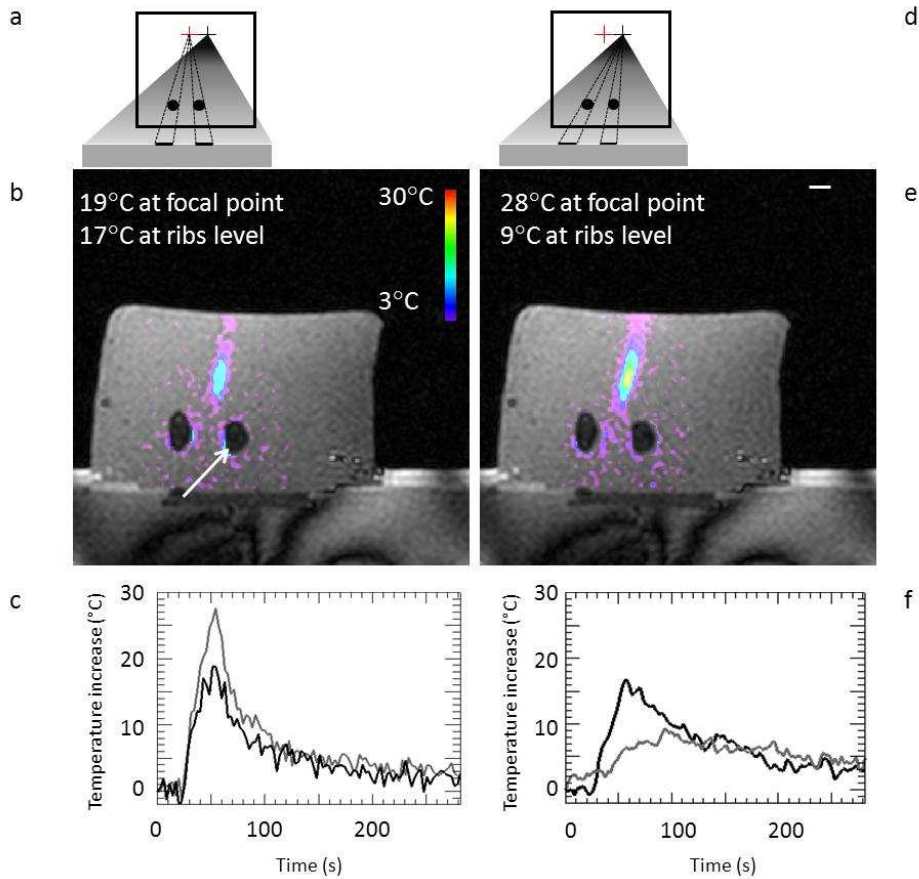


Figure III.4: Comparison of heating sonication through the ribs 7 mm right of the natural focal point with initial law (a) (b) and with updated law (d) (e). Diagrams at the top row (a, d) represents the method used to focus ultrasound with the corresponded temperature maps overlaid on modulus images below. The horizontal white bar on images (e) represents 10 mm. The colour scale for the temperature maps is indicated in b. Graph (c) compares the temperature evolution at the focal point and graph (f) at the ribs level (see white triangle (b)). Black curves correspond to sonication with initial law, grey curves to the case with updated law. The white arrow (b) indicates the maximal temperature increase at the rib cage level.

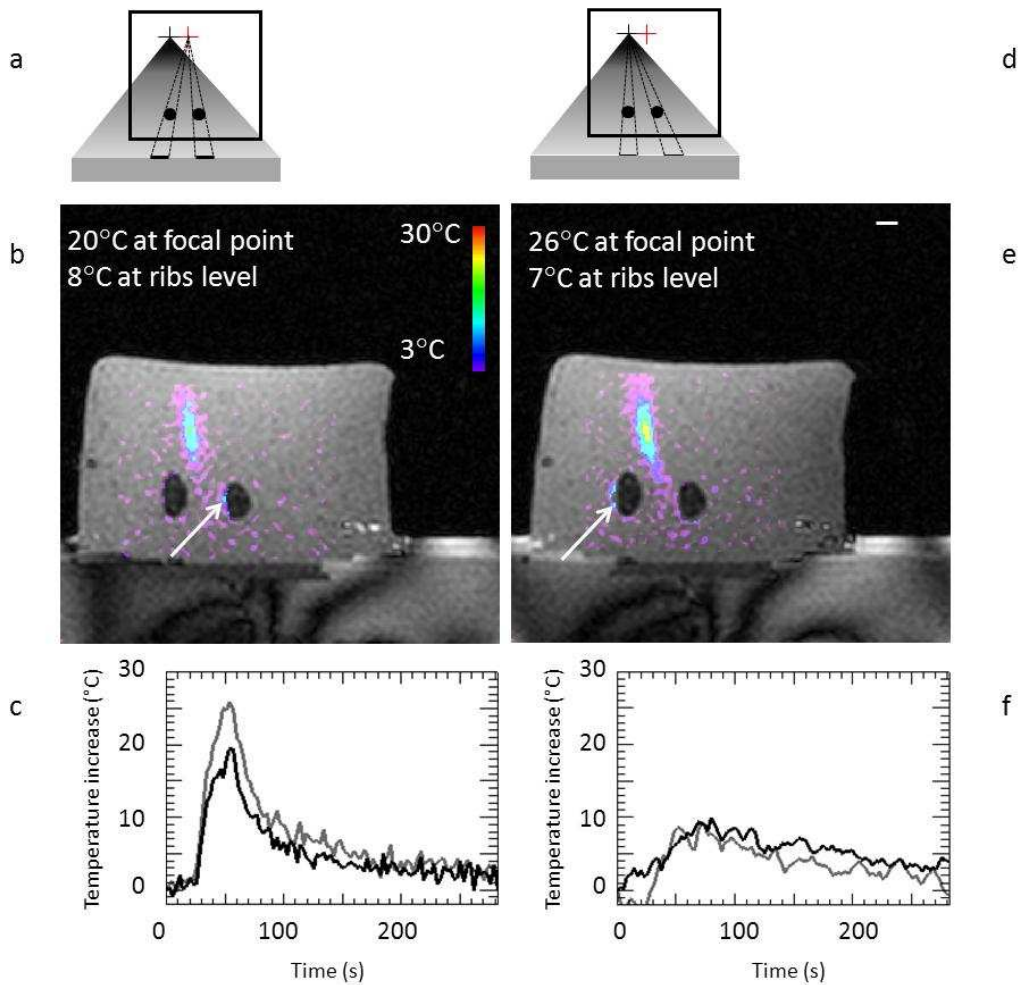


Figure III.4: Comparison of heating sonication through the ribs 7 mm right of the natural focal point initial law (a) (b) and with updated law (d) (e). Diagram at the top row (a, d) represents the method used to focus ultrasound with the corresponded temperature maps overlaid on modulus images below. The horizontal white bar (e) represents 10 mm. The colour scale for the temperature maps is indicated in (b). Graph (c) compares the temperature evolution at the focal point and graph (f) at the ribs level (see white arrow on (b)). Black curves correspond to sonication with initial law, grey curves to the case with updated law. The white arrow (b) indicates the maximal temperature increase at the rib cage level.

Table III.1 summarizes the results obtained for the different locations and binarized apodization laws. In this experiment, updated law increased slightly the numbers of activated elements: 142 for the right and the left compared to 131 for the initial law. Therefore, total emitted acoustic powers were in the same range for both conditions (see Table III.1).

| Location | Deactivation mode | Switch on/total | Effective acoustic power (W) | Maximal temperature increase (focal point) | Maximal temperature increase (ribs) |
|---------------------|-------------------|-----------------|------------------------------|--|-------------------------------------|
| Natural focal point | None | 256/256 | 100 | 36°C | 24°C |
| Natural focal point | Initial law | 131/256 | 51 | 31°C | 8°C |
| Right | Initial law | 131/256 | 51 | 19°C | 17°C |
| Right | Updated law | 142/256 | 55 | 28°C | 9°C |
| Left | Initial law | 131/256 | 51 | 20°C | 8°C |
| Left | Updated law | 142/256 | 55 | 26°C | 7°C |

Table III.1: Sonications characteristics. The first column indicates the localisation of the focal point, the second the type of binarized apodization law, the third the number of transducer elements activated compared to the total transducer elements, the fourth the maximal temperature increase at the focal point, the fifth the maximal

4. Discussion

In our study, the results obtained around the ribs showed maximal temperature decrease of ~70% was in accordance with literature (Quesson et al. 2010). The maximal temperature increase at the focal point was lower with the initial law. This small difference (36°C vs 31°C) could be explained by the fact that rib segmentation was manually drawn and may be overestimated from MR images. Development of automatic or semi automatic algorithm may reduce this potential bias. The cases where the deactivation was adapted to the targeted focal point were in the same range (26-31°C). However for the cases with beam steering the temperature increase was slightly lower. This could be explained by a loss of energy due to the higher absorption induced by the longer distance to cover to reach the deflected focal point than the natural focal point.

Marquet et al have simulated the temperature behaviour around the ribs for beam steering amplitude of 1cm and 1.5 cm, keeping the same binarized apodization law as for the natural focal point (initial law). Simulation results showed, for a focal point localized up to 1 cm laterally from the natural focal point, that the lethal thermal dose was not reach. However, no temperature measurement was realised. In our experiment when electronic deflection was used at 7 mm right of the natural focal point, and initial law was kept, the maximal temperature increase around the ribs remained high (17°C) and in the same range as the value measured at the focal point (19°C). In biological tissues, due to the long cooling duration of the ribs compared to the soft tissues (Quesson et al. 2010), the lethal thermal dose may be reached easily in spite of the temperature increase remained small. Then, an update of the binarized apodization law resulted in a 35% increase of the temperature at the focal point. Therefore, it could be interesting to mesh the area of possible electronic deflection every

millimetre and to pre-calculate and update record the binarized apodisation law for each location of focal point for further real time applications.

Another bias could be the deactivation of transducer element located at the frontier of the shadow. Until now, transducer elements covered by more than 50% of shadow were deactivated. There is no proof that this limitation is optimal. However, by using this simple method, Quesson (Quesson et al. 2010) reported no loss of heating efficiency *ex vivo* and *in vivo* in pig liver. An improvement could be deactivate all elements partially covered by the shadow, or maybe modulate the acoustic power for frontier elements as a function of partial coverage.

In conclusion, we showed that using beam steering performed without updating the binarized apodization law generated sufficient temperature increase around the ribs to reach lethal thermal dose. We overcame this limitation by updating the binarized apodization law for each new focal point location. Moreover, in this method, one acquisition of anatomical images and one segmentation of the ribs were sufficient to calculate for each targeted focal point, the corresponding combinations of transducer elements to deactivate. The simplicity of the method based on a geometrical approach make compatible real time applications. Therefore temperature at the focal point was increased and decreased around the ribs. This non invasive simple and practical method could provide an appropriate solution for real time HIFU treatment in mobile organs located in the rib cage by increasing the safety of patient.

5. References

- Aubry, J-F et al., 2008. Transcostal high-intensity-focused ultrasound: ex vivo adaptive focusing feasibility study. *Physics in Medicine and Biology*, 53(11), p.2937-2951.
- Botros, Y.Y. et al., 1997. A hybrid computational model for ultrasound phased-array heating in presence of strongly scattering obstacles. *IEEE Transactions on Biomedical Engineering*, 44(11), p.1039 -1050.
- Botros, Y.Y., Ebbini, E.S. & Volakis, J.L., 1998. Two-step hybrid virtual array ray (VAR) technique for focusing through the rib cage. *IEEE Transactions on Ultrasonics, Ferroelectrics and Frequency Control*, 45(4), p.989 -1000.
- Cochard, E. et al., 2011. Adaptive projection method applied to three-dimensional ultrasonic focusing and steering through the ribs. *The Journal of the Acoustical Society of America*, 130(2), p.716-723.
- Daum, D.R. et al., 1999. In vivo demonstration of noninvasive thermal surgery of the liver and kidney using an ultrasonic phased array. *Ultrasound in Medicine & Biology*, 25(7), p.1087-1098.
- Fink, M., 1992. Time reversal of ultrasonic fields. I. Basic principles. *IEEE Transactions on Ultrasonics, Ferroelectrics and Frequency Control*, 39(5), p.555 -566.
- Goss, S.A., Frizzell, L.A. & Dunn, F., 1979. Ultrasonic absorption and attenuation in mammalian tissues. *Ultrasound in Medicine & Biology*, 5(2), p.181-186.
- Köhler, M.O. et al., 2009. Volumetric HIFU ablation under 3D guidance of rapid MRI thermometry. *Medical Physics*, 36, p.3521.

- Liu, H.-L. et al., 2007. Feasibility of transcrib focused ultrasound thermal ablation for liver tumors using a spherically curved 2D array: A numerical study. *Medical Physics*, 34(9), p.3436-3448.
- Marquet, F. et al., 2009. Non-invasive transcranial ultrasound therapy based on a 3D CT scan: protocol validation and in vitro results. *Physics in Medicine and Biology*, 54(9), p.2597-2613.
- Marquet, F. et al., 2011. Optimal transcostal high-intensity focused ultrasound with combined real-time 3D movement tracking and correction. *Physics in Medicine and Biology*, 56(22), p.7061-7080.
- McGough, R.J. et al., 1996. Treatment planning for hyperthermia with ultrasound phased arrays. *IEEE Transactions on Ultrasonics, Ferroelectrics and Frequency Control*, 43(6), p.1074 -1084.
- Pinton, G.F., Aubry, J.-F. & Tanter, M., 2012. Direct phase projection and transcranial focusing of ultrasound for brain therapy. *IEEE Transactions on Ultrasonics, Ferroelectrics and Frequency Control*, 59(6), p.1149 -1159.
- Quesson, B. et al., 2010. A method for MRI guidance of intercostal high intensity focused ultrasound ablation in the liver. *Medical Physics*, 37(6), p.2533.
- Salomir, R. et al., 2000. Local hyperthermia with MR-guided focused ultrasound: Spiral trajectory of the focal point optimized for temperature uniformity in the target region. *Journal of Magnetic Resonance Imaging*, 12(4), p.571–583.

Wu, F. et al., 2004. Extracorporeal High Intensity Focused Ultrasound Ablation in the Treatment of Patients with Large Hepatocellular Carcinoma. *Annals of Surgical Oncology*, 11(12), p.1061-1069.

IV. INTERVENTIONAL CARDIOLOGY

1. Introduction

The aim of this study is the development of cardiac MR thermometry on the heart for the monitoring of thermal radio frequency ablations (RFA). MR cardiac imaging is restricted by respiratory (amplitude about 20mm and period about 3 seconds) and cardiac motions (period about 1 second).

There are basically four methods to deal with the motion:

- 1) To block the movement: impossible for the cardiac motion, under breath-hold for the respiratory motion. Usually, maximum breath-hold duration of 20 s is used practically for patients. The main disadvantage is the short duration that limits acquisition time.
- 2) Retrospective gating: the motion is recorded during a continuous acquisition to reorganise and sort the data during the reconstruction. The respiratory motion is recorded by using respiratory belt or a navigator. The ECG is used to detect the cardiac motion. The main disadvantage remains long acquisition duration.
- 3) Prospective gating: the acquisition is allowed for a short duration of the motion cycle. The main disadvantage is long acquisition duration.
- 4) Slice tracking: used for respiratory motion, the stack of slices is dynamically adjusted in real time to observe the same part of the body. The main advantage is the reduced acquisition time.

All of these techniques are routinely used in cardiac MRI. For MR thermometry, another constraint is the temperature precision. The standard deviation of the temperature depends on the SNR of modulus images and the T2* of the tissue as follow (Salomir 2001):

$$\sigma_T \approx \frac{400}{SNR B_0 T_E(ms)} \quad [1]$$

$$SNR = SNR_0 e^{\frac{-T_E}{T_2^*}} \quad [2]$$

$$\sigma_T \approx \frac{400}{SNR_0 e^{\frac{-T_E}{T_2^*}} B_0 T_E(ms)} \quad [3]$$

with the initial signal to noise ratio SNR₀ corrected for the rician distribution of the noise on MR magnitude images, B₀ the static magnetic field in Tesla, and T_E the echo time. The minimum of the standard deviation is the minimum of the function, equation [3], for TE=T2*. Measurements of SNR on thermometry magnitude images and T2* of the heart are required to calculate the SNR₀ according to the equation [2] and therefore the standard deviation of the temperature.

In this purpose, this chapter presents: 1) the reference planes for imaging the heart due to its oblique orientation in the body, 2) a study of the T2* on *in vivo* volunteer hearts 3) an estimation of the standard deviation of the temperature and minimum spatial resolution, 4) a thermal RF ablation experiment *in vivo* on the sheep heart under MR thermometry, 5) a pilot experiment of imaging with the catheter as an antenna.

2. Conventional imaging plans in Cardiac MRI

Conventional representations for MR-images of patients are in coronal, sagittal and transversal orientations. The double oblique orientation of the heart in the body justifies a change of imaging reference system adapted to the anatomy of the organ structure (4 cavities, 2 cavities, short axis). The following images show the method to retrieve these orientations from conventional orientations.

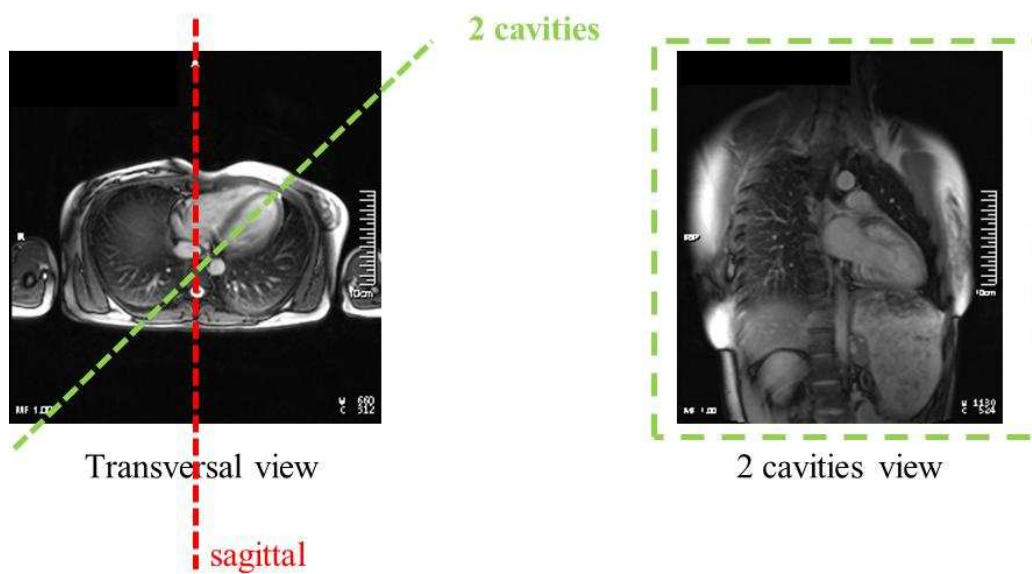


Figure IV.1: Localisation of 2 cavities view

From transversal image, the two cavities slice is oriented parallel to the septum, placed at the middle of the left ventricle and crosses the apex and the middle of the left atrium (Figure IV.1).

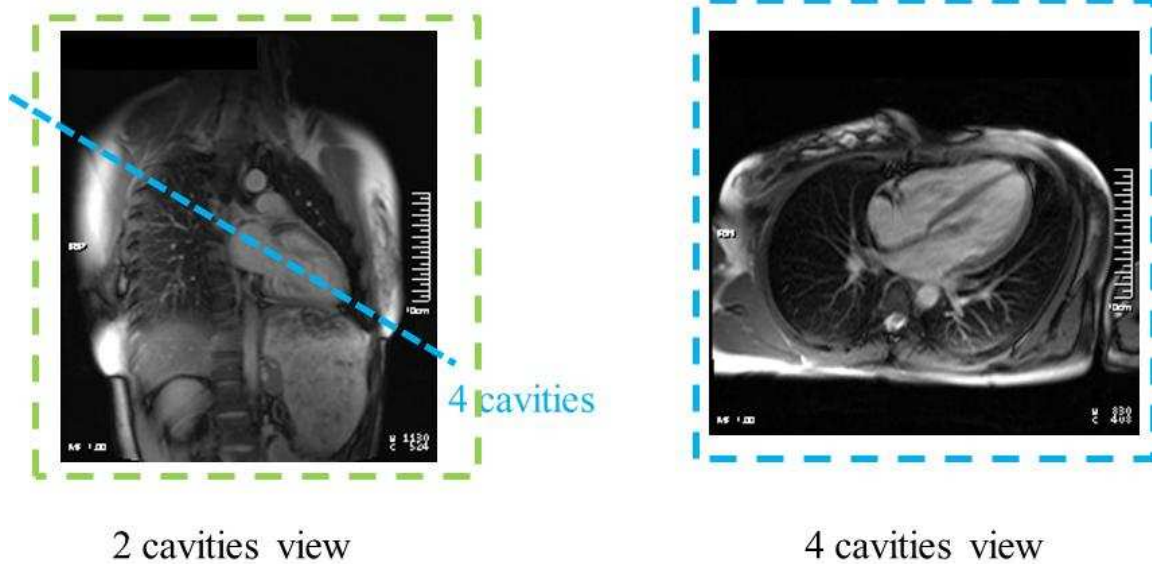


Figure IV.2: Localisation of 4 cavities view

The orientation of the four cavities slice is determined from the two cavities image. The slice is perpendicular to the two cavities view, placed at the middle of the left ventricle and oriented to cross the middle of the left atrium and the apex (Figure IV.2).

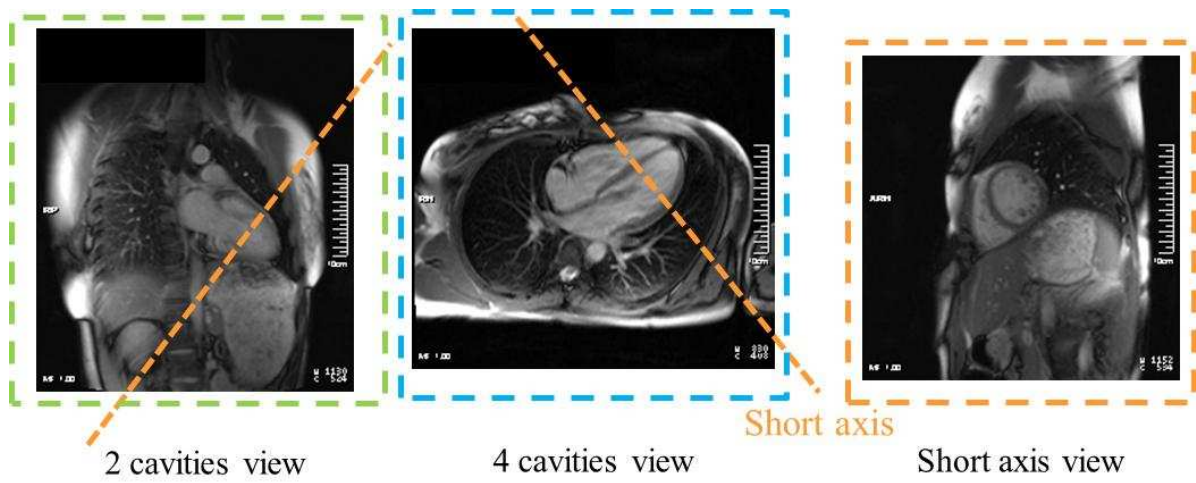


Figure IV.3: Localisation of short axis view

The short axis view is placed perpendicular to the two cavities view and the four cavities view and covers entirely the left ventricle (Figure IV.3).

3. T2* measurement *in vivo* in the human heart

1. Introduction

In MRI, two relaxation times T1 and T2 are involved in the contrast of images. T1 and T2 are tissue specific. T1, called longitudinal relaxation time, is induced by spin lattice relaxation. T1 is the time that corresponds to 63% of recovery of the original longitudinal magnetisation. T2, called transverse relaxation time, is due to spin-spin relaxation. T2 is the time that corresponds to 63% loss of the initial amplitude of the transverse magnetisation. Transverse relaxation time is shorter than longitudinal relaxation time. In gradient echo sequence, a new transverse relaxation time called T2* has been introduced to take into account the magnetic field heterogeneities. The relationship between T2 and T2* is described as follow:

$$\frac{1}{T_2^*} = \frac{1}{T_2} + \frac{1}{T_2'} = \frac{1}{T_2} + \gamma\Delta B$$

where γ is the gyromagnetic ratio and ΔB the magnetic field inhomogeneity across a voxel (Chavhan et al. 2009).

The optimal echo time to minimise the standard deviation of the temperature measurement and maximise the signal to noise ratio on temperature images is equal to T2* (Quesson et al. 2000). T2* is tissues, patient and scanner dependent, since local field heterogeneities depends on the patient's anatomy and magnet quality. Different techniques have been proposed to measure T2* in the heart at 1.5 T. The aim of these studies was to estimate the iron concentration in the patient's heart with thalassaemia disease through T2*

measurement. Three types of techniques have been used to measure the $T2^*$ in the heart: two were based on gradient echo sequence and, one on spin echo sequence.

Segmented gradient echo sequence, triggered on the heart and under breath-hold, have been used (Reeder et al. 1998, L. J. Anderson et al. 2001, Westwood et al. 2003). For these studies, the breath-hold duration (see table IV.1) ranged between 8 s and 42 s. This method gave the possibility to sample the exponential $T2^*$ decay curve between 2 ms and 21 ms. The TR was limited by the heart beat period (800 – 1200 ms). The echo time was limited by the repetition time (TR). An increase of the echo time led to a decrease in signal to noise ratio and an increase of the sequence duration, as in Reeder's study (Reeder et al. 1998), where breath-hold duration ranged between 37 and 42 s. Such apnea duration is very long and remains difficult to hold for patients and even for volunteers. In the other studies (L. J. Anderson et al. 2001)(Westwood et al. 2003) the TR was adapted at each chosen TE, inducing a bias in the estimation of $T2^*$ due to different T1 saturation values

The second method consisted in a segmented multiecho gradient sequence (Westwood et al. 2003) (Positano et al. 2007) (Ramazzotti et al. 2009)(Ou et al. 2012). Using a fixed TR, measurements for all TE were realised in a single breath-hold. For the same reasons, the range of TE value remained limited under 21 ms. This method is the most popular and has the advantage to generate all data to measure the $T2^*$ in only one acquisition.

Another method has been developed based on fast spin echo imaging in conjunction with black blood preparation (Heinrichs et al. 2009). Fast spin echo imaging is not sensitive to image distortion due to B_0 inhomogeneity observed in fast GE-based images. The sequence called displaced U-FLARE (Figure IV.4) was based on U-FLARE sequence. In order to introduced $T2^*$ weighting on image intensity, a delay τ was introduced before the refocusing

by the RF pulse. A gradient was added in the readout direction to avoid unwanted interferences with other echoes than those produced by the RF pulse α and displaced them out the reading of the signal. This technique enlarged the range of sampling the $T2^*$ exponential curve. This sequence did not require breath-hold and was realised on free breathing volunteers under cardiac triggering (ECG). Table IV.1 summarizes these methods, their characteristics and the $T2^*$ values measured for the cardiac muscle. These studies were performed at 1.5 T, with a sampling time ranged between 2.5 ms and 25 ms except for Reeder (Reeder et al. 1998) and Heinrichs (Heinrichs et al. 2009). Over these studies performed at 1.5T, the $T2^*$ value was estimated between 29.9 ms and 52 ms (see table V.1).

In our study, the initial method chosen to estimate the $T2^*$ was a gradient echo sequence triggered on the heart and gated on the respiration. Then, in order to reduce the total scan duration, a segmented gradient echo sequence triggered on the heart and under breath-hold was chose. This study was performed on 10 healthy volunteers.

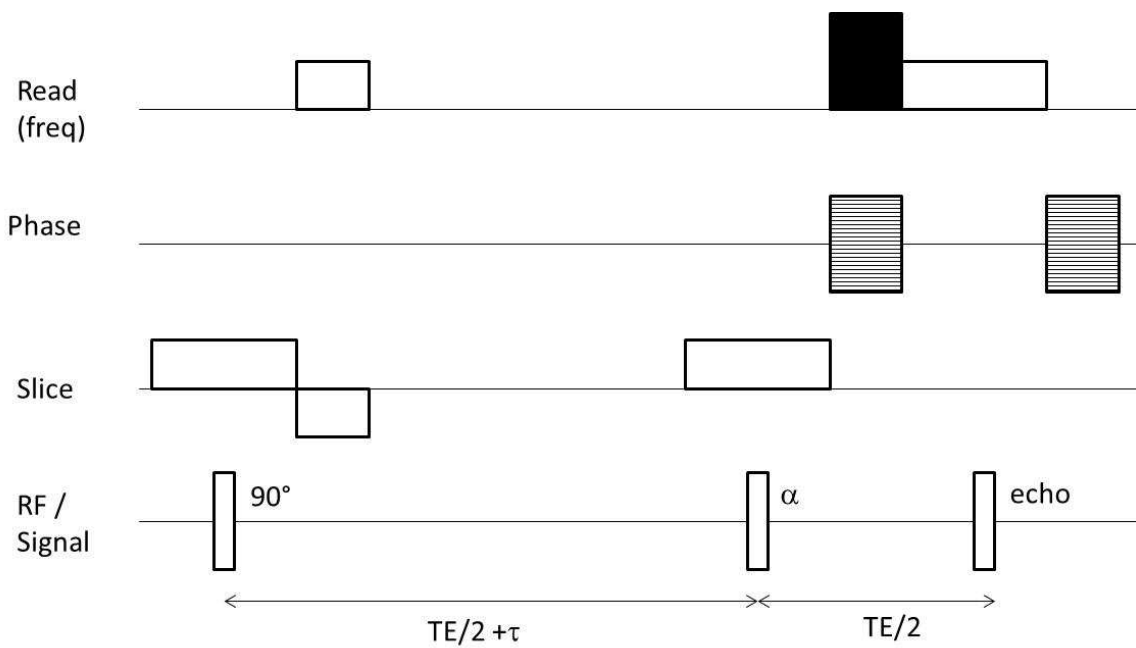


Figure IV.4: Diagram of displaced U-FLARE sequence

| Author | Year | Number of healthy volunteers | Time range (ms) | Repetition time TR (ms) | T2* (ms) | Sequence | Material |
|-----------------|------|------------------------------|-----------------|-----------------------------|------------|---|---------------------------|
| Reeder et al | 1998 | 5 | 2.4 – 45 | 50 | 38 ± 6 | spoiled gradient-echo, breath-hold 37 – 42 s | GE Signa 1.5 T Horizon |
| Anderson et al | 2001 | 15 | 5.6 – 17.6 | 11.8 – 23.8 | 52 ± 16 | Gradient echo breath-hold 8 – 13 s | Picker 1.5 T Edge Scanner |
| Westwood et al | 2003 | 10 | 5.6 – 18 | TR = TE + 2.58 | 33.3 ± 7.8 | Segmented spoiled gradient-echo Breath-hold ~ 20 s | Siemens Sonata 1.5 T |
| | | 10 | 2.6 – 16,74 | 20 | 30.1 ± 7.1 | Multiecho gradient Breath-hold | |
| Positano et al | 2007 | 15 | 2 – 20.3 | - | 36 ± 5 | Segmented fast-gradient-echo multi-echo Breath-hold 10 – 18 s | GE Signa 1.5 T |
| Heinrichs et al | 2009 | 6 | 0 – 40 | 1.6 – 2,4 2 R-R interval | 29.9 ± 6.6 | Displaced U-FLARE Free breathing | 1.5 T Achieva Philips |
| Ramazotti et al | 2009 | 30 5/site | 2 - 20.3 | - | 36 ± 5 | Segmented fast-gradient-echo multi-echo Breath-hold 10 – 18 s | GE Signa 1.5 T |
| Ou et al | 2012 | - | 2 – 17.4 | 19 | > 20 | Segmented multiecho gradient Breath-hold | 1.5 T Achieva Philips |

Table IV.1: Summary of the literature: MRI sequence and method for T2* measurement

2. Methods and results

a. Gradient echo sequence

Gradient echo sequence was performed under free breathing and triggered on respiration motion by a navigator, and on the heart beat by ECG. Data were acquired on a Siemens Avanto 1.5T scanner (Erlangen Germany) with 32 channels cardiac coil. For the first volunteer the following parameters were applied: 128 x 128 mm FOV, 64 x 64 acquisition matrix, 76° flip angle, 1 slice of 5 mm thickness positioned in short axis orientation, acquisition time 4 minutes and 43 seconds. The septum region was manually segmented by using Osirix software for the estimation of T2* and the mean of the signal intensity was plotted as a function of the TE values (Figure IV.6). The curve was fitted by an exponential function ($K e^{-TE/T2^*}$) using least square method. The estimated T2* value was 38.4 ms.

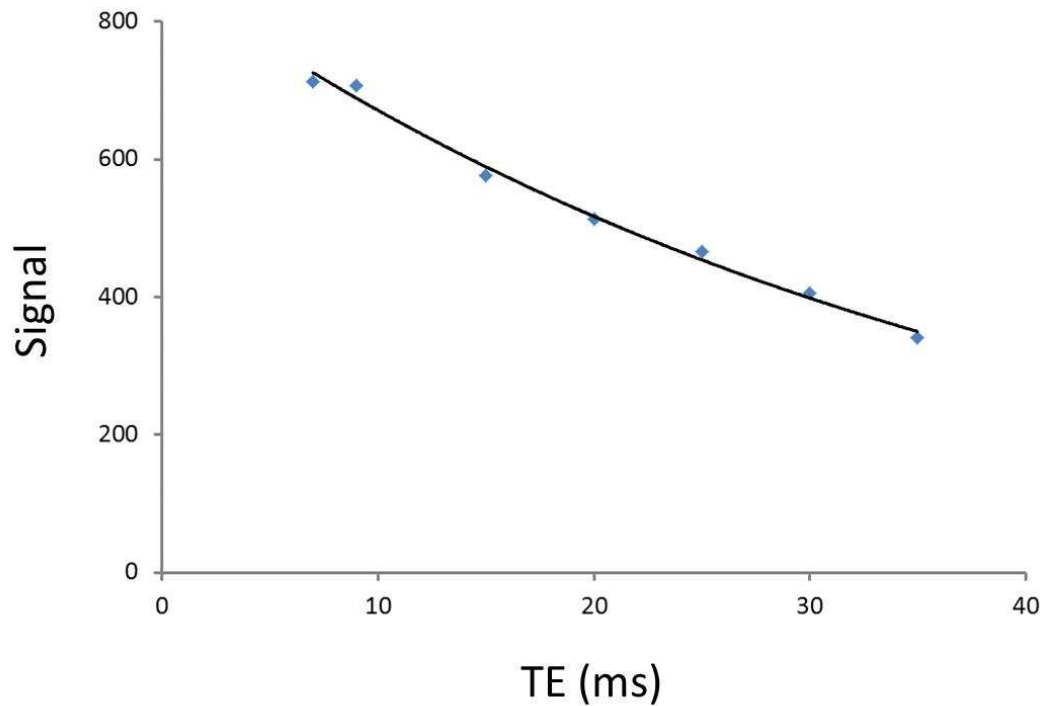


Figure IV.6: Regression curve between signal and TE. Experimental data are displayed in blue. The curve in black is the fit according to the equation $Ke^{-TE/T2^*}$. The determination coefficient is $R^2=0.99$

The same experiment was performed on the heart of another volunteer. The following parameters were applied: 143 x 170 mm FOV, 54 x 64 acquisition matrix, 87° flip angle, 1 slice of 6 mm thickness positioned in short axis orientation, acquisition time 6 minutes and 58 seconds.

Unfortunately, the image quality was too poor to properly estimate the T2* value. During this acquisition, the respiratory motion detected by the navigator was recorded and showed a very irregular motion. The Figure IV.7 compares images of the first acquisition (top row) and the second (bottom row) for TE.

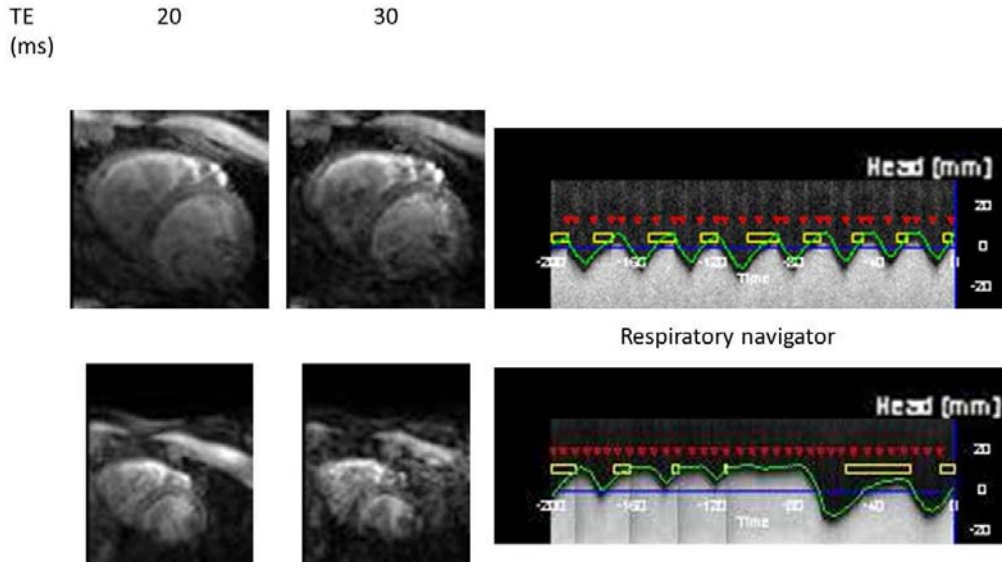


Figure IV.7: the impact of the irregularity of the respiratory motion on the image quality. The figure show gradient echo image for TE of 20ms and 30ms and the image registered by the respiratory navigator. The first line is for the first volunteer and the second line for the second volunteer.

This sequence presented the advantages to be simple and gave the possibility to have a large range in echo time values. However, the acquisition time remained long. We consequently chose to accelerate this sequence to perform the protocol under breath-hold to avoid respiratory motion.

b. Segmented gradient echo sequence

The segmented gradient echo sequence was performed under breath-hold and triggered on the heart beat by ECG. The following parameters were applied: TR: 141 ms, 128 x 128 mm FOV, 64 x 64 acquisition matrix, 25° flip angle, 1 slice of 5 mm thickness positioned in

short axis orientation, 5 segments, breath-hold 10-17s depending on the heart rate. This study was performed on 9 healthy volunteers.

The figure IV.8 shows a representative data set obtained by using the segmented GE sequence. Images acquired at different TE (top row figure IV.8) shows a decrease in image quality as a function of TE increase. The graph plots the mean signal of the septum as a function of TE and revealed an exponential decrease.

The table IV.2 presents T2* values obtained for the 10 volunteers septum and the determination coefficient of the curve fit. T2* values were ranged between 31.1 ms and 47.3 ms. The mean of T2* value over the ten volunteers was 40.2 ± 6.7 ms in good agreement with value already reported. The determination coefficient was ranged between 0.84 and 0.99. the last value was obtained with the first method.

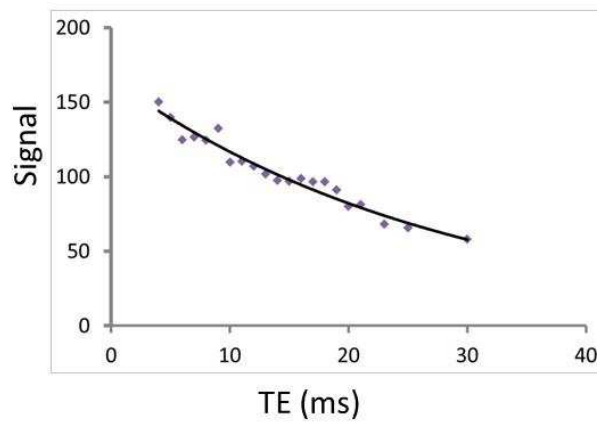
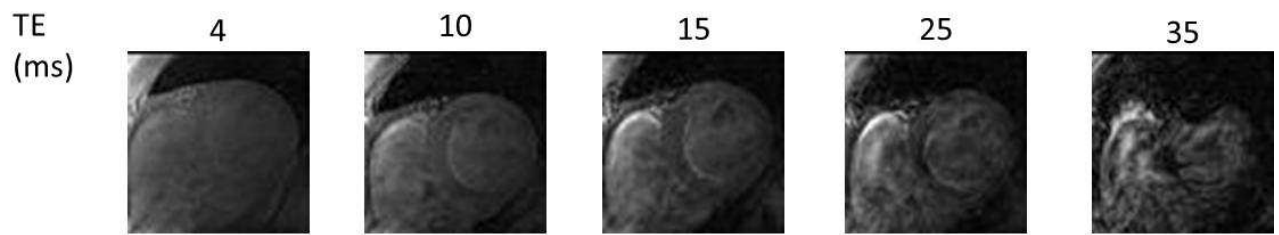


Figure IV.8: T2* estimation by using a segmented gradient echo sequence. At the top, modulus images obtained for different TE. The graph at the bottom displays the signal as a function of TE. On the graph the black curve is an exponential fit.

| Volunteer | T ₂ [*] | Determination coefficient R ² |
|---------------------------|-----------------------------|--|
| 1 | 45.8 | 0.95 |
| 2 | 43.4 | 0.84 |
| 3 | 46.7 | 0.93 |
| 4 | 47.3 | 0.98 |
| 5 | 45.4 | 0.98 |
| 6 | 43 | 0.94 |
| 7 | 32.7 | 0.98 |
| 8 | 28.5 | 0.97 |
| 9 | 31.1 | 0.94 |
| 10 | 38.4 [*] | 0.99 |
| Mean ± standard deviation | 40.2 ± 6.7 | |

Table IV.2: summary of the T₂^{*} estimation on the heart. The value with the * is obtained from a gradient echo sequence was performed under free breathing.

3. Discussion

With the segmented gradient echo sequence, an estimation of $T2^*$ of the heart was realized with a short acquisition time. The mean value of $T2^*$ was in agreement with the literature. However, the sampling time used to evaluate the $T2^*$ time appears too restrictive for precise $T2^*$ determination. In this study like in the others in the literature the maximum TE value was limited because of the decrease in image quality. This limit appeared usually for TE around 25 ms. The Figure IV.8 illustrates this limitation showing the poor image quality obtained above TE of 25 ms. The small range of TE time made difficult the interpretation of the fit with data showing almost linear behaviour. The aim of most of studies on $T2^*$ heart involved short $T2^*$ due to the presence of iron in the tissue with $T2^* < 20\text{ms}$. Under these conditions, the range of sampling remained sufficient to accurately estimate small $T2^*$ values. In the case of healthy volunteers with higher $T2^*$, increase the range of sampling using displaced U-FLAIRE method may improve the precision of the $T2^*$ estimation. However, at the time of this project, it was not possible to implement sequence like displaced U-FLARE which can provide a larger range of sampling time. Nevertheless, the estimated $T2^*$ (40.2ms) was in good agreement with the literature and was used in the evaluation of the precision of MR thermometry.

4. Temperature precision

The temperature precision for MR thermometry has been already study in abdominal organs (Roujol et al. 2010, Holbrook et al. 2010, Rieke & Butts Pauly 2008, Quesson et al. 2000). They showed a temperature precision in the range of 1°C in mobile organs. A recent study has reported an evaluation of temperature precision of the heart (D. Senneville et al. 2012). They found a precision of 3°C under free breathing with motion correction. In the following study, the experiments were realized without any motion correction and under breath-hold.

1. Estimation of the standard deviation of the temperature

In order to estimate the SNR_0 , thermometry sequences were performed on four volunteers in absence of heating (Figure IV.9) on a Siemens Avanto 1.5T scanner (Erlangen Germany) with 32 channels cardiac coil. The four data sets were acquired with different TE and resulted in 15 images with identical parameters. A region of interest (ROI) of the septum in the heart and a ROI in a region without signal were used to calculate the SNR on each image. The SNR_0 was calculated according to the equation [2] and $T2^*$ equal to 40.2 for the heart and found equal to 30. In order to avoid potential bias in the estimation of the SNR that may vary spatially because of coil design and/or parallel imaging, noise images (Figure IV.9) were acquired with the same sequence but with a 0° flip angle RF pulse. Noise images were divided in 15 ROI (figure IV.10). The averages and standard deviation values were calculated for each ROI. The noise distribution was found homogeneous (averages: 11 and standard deviation: 1.5).

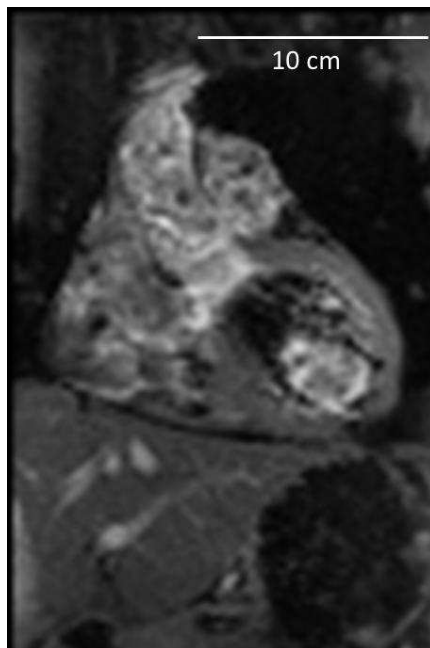
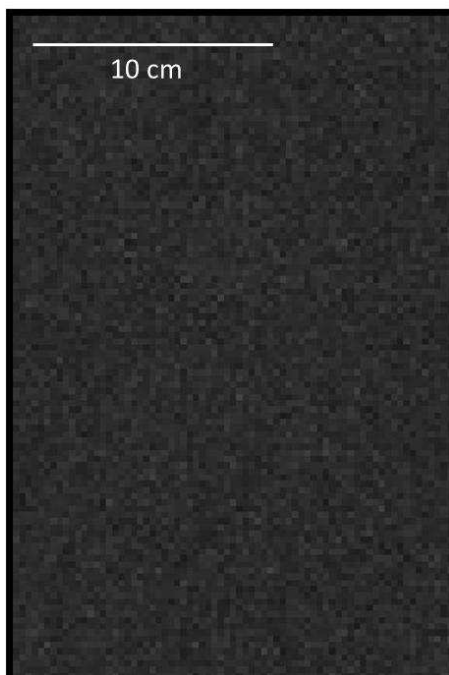


Figure IV.9: SNR of MR thermometry modulus images. Modulus image of MR thermometry in volunteer's heart is displayed in coronal view. Sequence has the following parameters : single shot EPI, acceleration factor : GRAPPA 2, TE= 25 ms TR=1200 ms (heart beats period), 187.67 x 280 mm FOV, matrix 72 x 108, 65 ° flip angle, slice thickness :7 mm.



| | | |
|-------------|---------------|-------------|
| 11 ± 1.5 | 11 ± 1.5 | 11 ± 1.5 |
| 11 ± 1.5 | 11 ± 1.5 | 11 ± 1.4 |
| 11 ± 1.5 | 11 ± 1.6 | 11 ± 1.6 |
| 11 ± 1.5 | 11 ± 1.4 | 11 ± 1.5 |
| 11 ± 1.5 | 10.5 ± 1.5 | 11 ± 1.5 |

Figure IV.10: Noise image (left) and spatial distribution of noise (right) from MR thermometry sequence with the following parameters : single shot EPI, acceleration factor : acceleration factor = GRAPPA 2, TE= 25 ms TR=1200 ms (heart beats period), 187.67 x 280 mm FOV, matrix 72 x 108, 0 ° flip angle, slice thickness :7 mm.

The graph (figure IV.11) shows the simulation of standard deviation of the temperature for the $T2^*$ of the heart and the initial SNR_0 extracted from MR temperature images (Figure IV.10). The minimum of the standard deviation of the temperature was expected at $TE=T2^*$, and was equal to 0.60°C . The error bars took account of $T2^*$ and SNR_0 standard deviation values from measured values. The standard deviation of the temperature measured on thermometry images was 1.26°C at a $TE=17\text{ms}$ and 0.8°C for the simulation.

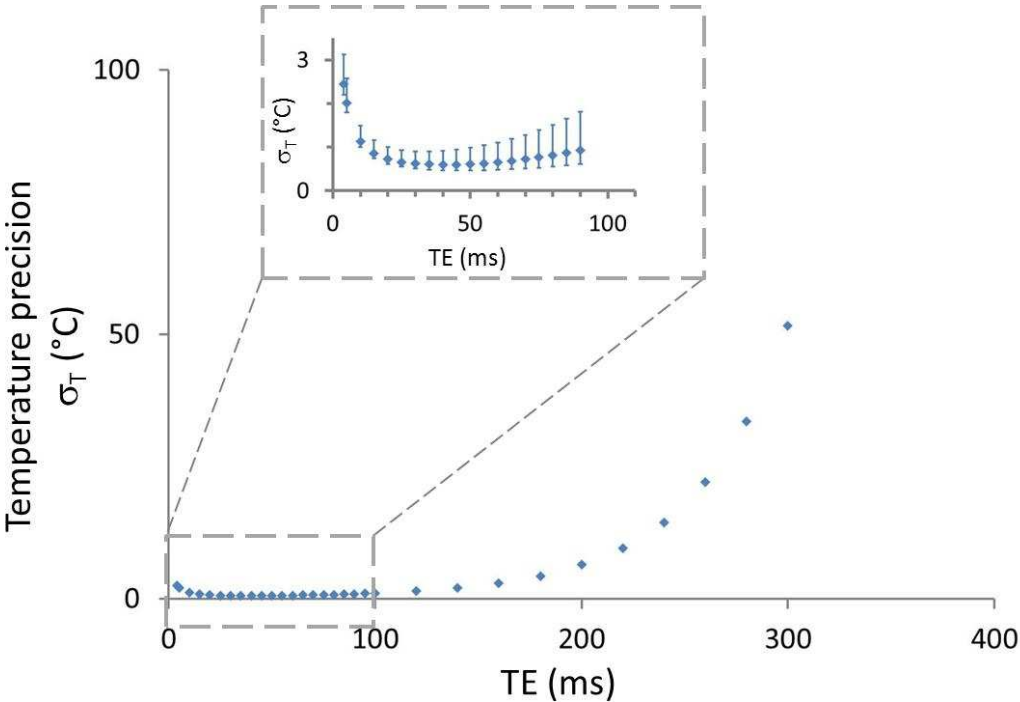


Figure IV.11: Theoretical precision of the temperature as a function of TE according to the equation [3]. Simulation was performed for a temperature increase of 1°C . The inset shows a zoom of the graph between $TE=0-90$ ms.

2. Discussion

The estimation of the standard deviation measured on thermometry images was slightly higher than those from simulation. The difference with the simulation could be explained by

the lack of motion correction for the cardiac and respiratory residual motion although the acquisition was performed under breath-hold and triggered on the heart beat.

Compared to the previous study (D. Senneville et al. 2012), the standard deviation of the temperature was lower in our experiments. It can be explained by the relatively reduced motion amplitude due to the breath-holding in our study compared to the free breathing in the other study. Moreover, the SNR on our modulus images was higher (30) than in the other study (20) which directly impacts on the standard deviation of the temperature. This difference can be related to the MR-cardiac coil used in the study: 32 channels in our study and 5 channels in the other study. Usually the TE used in cardiac MR thermometry was ranged between 10 to 40 ms. According to the simulation, for a standard deviation of the temperature equal to 3°C, the minimum required SNR, for the range of TE described above, was ranged between 6 and 11. At the moment, for the same range of TE our SNR is range between 11 and 23. Therefore, the voxel size may be reduced by a factor 1.26^3 , for example 2 x 2 x 5 in order to improve the spatial resolution. Although the SNR was increased, compared to the literature, the gain in spatial resolution remained limited and justified the use of dedicated coils such as the catheter tip to overcome this limitation. However, the large range of FOV, used in this present method, may ensure a better control of eventual collateral heating that may happened (Tsuchiya et al. 2007) and therefore increases the safety of the procedure.

5. Radiofrequency thermal ablation under MR thermometry: preliminary experiments

1. Introduction

Cardiac catheter ablation procedures are usually performed under fluoroscopy guidance. In order to increase the safety of the procedure several parameters can be measured via the catheter tip: impedance of the tissues at the tip of the catheter, electrode temperature, local electrocardiogram changes. However, all these parameters resulted in poor prediction of lesion extent. Clinical feasibility of MR thermometry has been demonstrated for mobile organs like liver and kidney (Seror et al. 2008, Ishihara et al. 1995). The measurement of the lethal thermal dose has been demonstrated highly correlated with the resulted lesion (Quesson et al. 2011).

Studies have shown the feasibility of MR thermometry during cardiac radiofrequency ablation on animals (Kolandaivelu et al. 2010, D. Senneville et al. 2012). Both studies used PRF based MR thermometry. In the first study (Kolandaivelu et al. 2010), MR thermometry was performed on dog heart by using high-resolution segmented GRE imaging with 10 to 20 s per slice under ECG and respiratory triggering.

A precise estimation of thermal dosimetry can not be performed because of the limited temporal resolution of the MR thermometry sequence. The second study used a faster sequence ~800 ms (one heart beat) for 5 slices and proposed navigator-based slice tracking and image processing for compensation of motion to improve the temperature precision that remained under 3°C. Both studies were realised by using non irrigated catheter.

However, the use of irrigated-tip catheter has shown improvements by increasing lesion depth (H. Nakagawa et al. 1995, Skrumeda & Mehra 1998, Scaglione et al. 2012), reducing embolism risks (Scaglione et al. 2012, Blanc et al. 2008), limiting collateral heating due to

possible currents in the catheter induced by RF pulse from the MR antenna (Haines 2011). The following experiment shows the feasibility of RF ablation under MR thermometry by using an irrigated catheter, first in a gel, and then, in a sheep heart *in vivo*.

2. Material method

- Gel preparation

Phantom was an agarose gel doped with NaCl (0.9%) to allow electrical propagation. The concentration of NaCl was chosen at the same osmolarity than blood. The impedance of the gel measured by the generator via the catheter was 120Ω in the same range as values measured in patients.

- Animal preparation

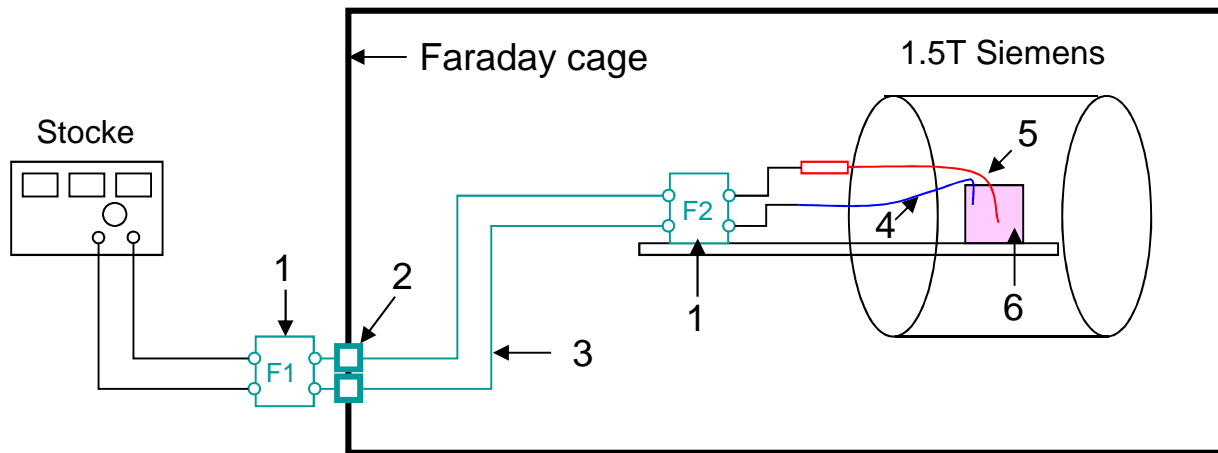
One sheep (approximately 60 kg) was sedated by intramuscular injection of $0.1 \text{ mg} \cdot \text{kg}^{-1}$ of acepromazine (Calmivet, Vetoquinol, Lure, France) and ketamine ($0.1 \text{ mL} \cdot \text{kg}^{-1}$) and anesthetized by intravenous injection of $0.1 \text{ mL} \cdot \text{kg}^{-1}$ of pentobarbital (CEVA Santé Animale, Libourne, France). The analgesia was introduced by an intramuscular injection of ketoprofen (Ketofene, Merial, Lyon, France) at a dose of $3 \text{ mg} \cdot \text{kg}^{-1}$. The anesthesia was maintained by continuous intravenous injection through the jugular vein of pentobarbital at a rate of $7.2 \text{ mg} \cdot \text{kg}^{-1} \cdot \text{h}^{-1}$. The chest was carefully shaved and depilatory cream was applied for removing residual hairs in order to ensure correct contact between MR compatible ECG electrodes and skin. The MRI compatible RF-ablation catheter was placed in the left ventricle under fluoroscopic guidance. The animal was transferred to the 1.5 Tesla MRI (Avanto, Siemens, Erlangen, Germany) scanner and installed in supine position. The animals were maintained under assisted ventilation (400 mL at 100% O₂ of 2% isoflurane in pure oxygen, at a frequency of 20 bpm) during the procedure (respirator Aestive /5 MRI, Datex Ohmeda). After

completion experiments, the animal was euthanized by intravenous injection of Dolethal (CEVA Santé Animale, Libourne, France).

- *MRI and catheter*

The irrigated catheter was provided by Biosense Webster (MR compatible) Notch passive filters tuned to 64 MHz were inserted in the transmission line to protect the RF generator and to reduce electromagnetic interferences that may affect the image quality (Figure IV.12).

MR thermometry was performed by using the Proton Resonant Frequency (PRF) shift method with a single shot Echo Planar Imaging (EPI) sequence, with the following acquisition parameters: TE= 20 ms TR=457 ms (heart beats period for animal), accelerator factor = GRAPPA 2, 166.67 x 250 mm FOV, matrix 64 x 96, 60 ° flip angle, 3 adjacent slices of 6 mm thickness positioned in vertical orientation. Temperature images were calculated (PRF constant of 0.0094 ppm.°C⁻¹) and displayed with the software thermoguide (Image Guided Therapy, Pessac). MR thermometry on the sheep heart was realized under breath-hold in absence of motion correction algorithm and slice tracking for the compensation of the respiratory motion.



1: filters, 2: connector, 3: cable, 4: return electrode, 5: catheter, 6: agar gel (with
Figure IV.12: Experimental setup for catheter ablation under MR thermometry.

3. Results

a. On gel

- MR compatibility

The size of the artefact, using the MR-thermometry sequence, was 5 mm (about twice the actual size of the electrode tip, data not shown) without any active connection. This size of artefact is compatible with MR thermometry.

- Measure of the Impedance

The generator measured the tissues impedance to avoid overheating. However, modifications in the electrical pathway (filters, cables) may affect this measurement. To evaluate this effect, several impedances with known values ranging between $R=20$ to 220 ohms were put in contact with the catheter and the return electrode and the impedance measured on the generator was recorded. Representative values of heart tissue impedance were tested [25Ω - 225Ω] (D. Haines 2004).

The following graph (Figure IV.13) presents the results of the measured impedance by the generator as a function of the real impedance value (measured with classical ohm-meter and confirmed with the components values).

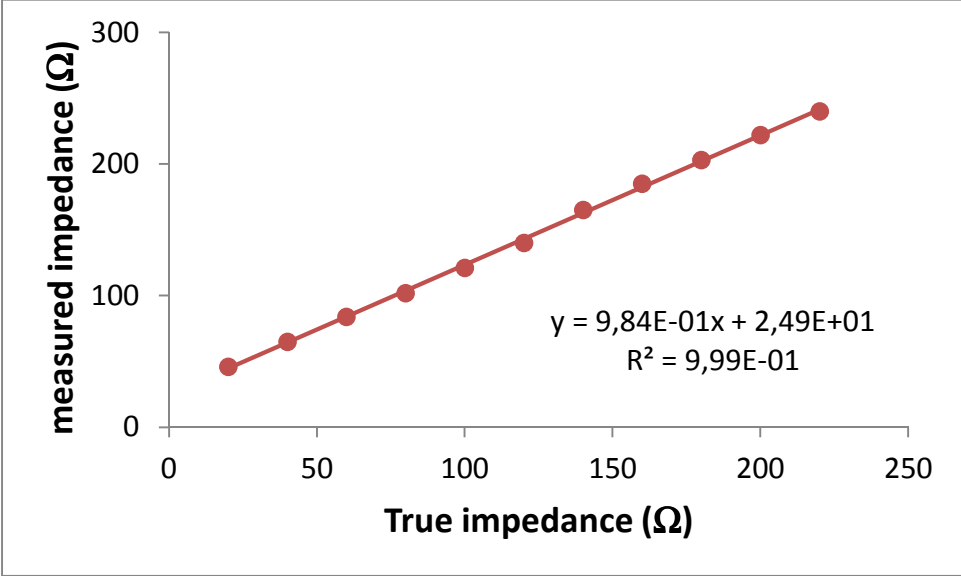


Figure IV.13: Impedance measured by the catheter via the generator as a function of true impedance measured by ohmmeter. Red circles are experimental data. Red linear curve is the fit.

A systematic offset of 20-25 Ω was observed over the range of the input resistances.

A linear fit of the measured data vs input data resulted in the following values:

$$R(\text{generator}) = 0.98.R(\text{actual}) + 24.90 ; R^2 = 0,99$$

- Signal to noise stability and temperature precision

The SNR was analysed and showed a value, about 115, sufficient to performed MR thermometry with excellent precision. This value stayed stable during radiofrequency ablation showing non disturbance from the active catheter. Temperature precision measured in a non heated area remained under 1°C for both conditions.

- RF heating and irrigated flow

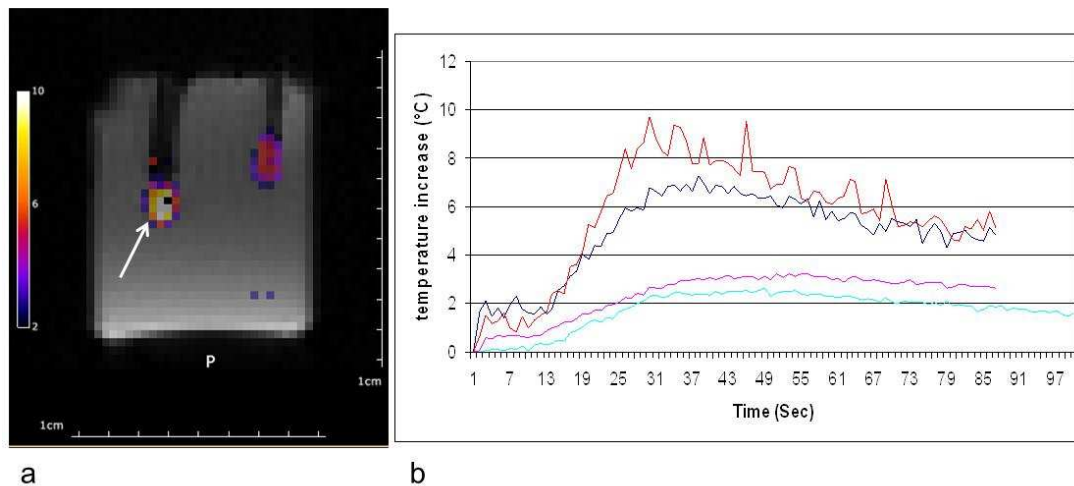


Figure IV.14: Influence of irrigation of the catheter on the temperature increase during RF heating by catheter. Temperature image, at the end of RF heating, overlaid on modulus images (a), the RF catheter was the wire at the left and the wire at the right is the return electrode. Temperature evolution at different flows (b): 0 mL/min (red and pink curves) and 1mL/min (blue curves), in a single pixel (dark blue and red curve) and the average over a ROI surrounding the catheter tip (light blue, pink). The white arrow (a) indicates the location of temperature measurement for the graph.

The impact on temperature behaviour, for different irrigated flows (0 mL/min and 1 mL/min), at identical power (10 W) and duration (20 s), was investigated (Figure IV.14). In the image (a) the RF catheter was located at the left. An increase of temperature was generated at the return electrode because the energy density was high compared to the pads used for clinical application. The maximal temperature increase, in a pixel located close to the catheter tip (3mm), was 9°C and 7°C (20% reduction) for 0 mL/min and 1 mL/min flows respectively. The mean temperature increase, into an area surrounding the catheter tip, showed similar

temperature behaviour although the difference between temperature increases was reduced because of the spatial averaging.

Additional data have been collected with higher flow ($F=30$ mL/min and 60 mL/min), showing that limited heating could be observed. However, the setup was very different as compared to *in vivo* conditions since the flow is directly sent to the gel and such values of flow induced the destruction of the gel and resulted in non-exploitable MR image quality. *In vivo* the fluid is diluted in the blood circulation and such effect is therefore not expected.

b. Animal in vivo

- Signal to noise stability and temperature precision

The signal to noise ratio remained stable over the procedure and equal to 50. The standard deviation of the temperature, measured in a non-heated area of heart, *in vivo* was about 1.5°C .

- RF heating

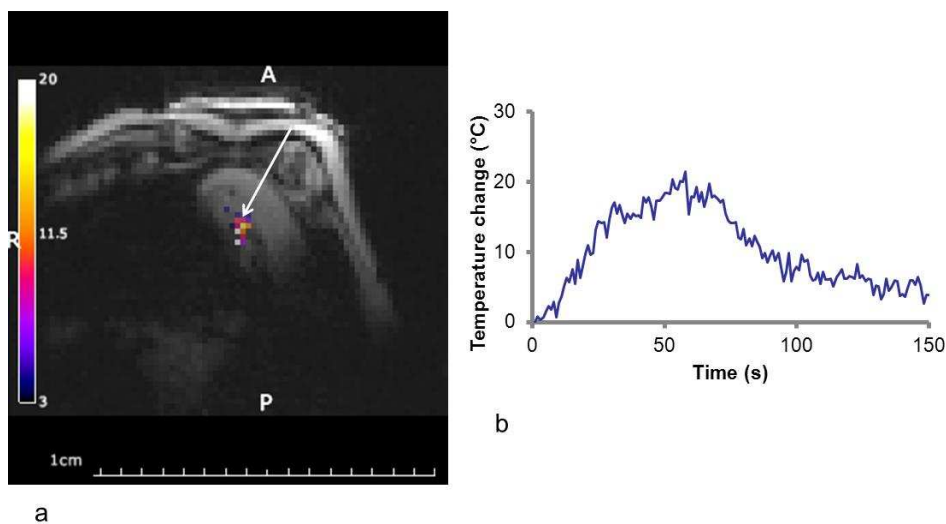


Figure IV.15: Temperature distribution after 1 min of 20W RF application, overlaid on the magnitude image (a). Temperature evolution at the hottest pixel in the myocardium (b). The white arrow (a) indicates the location of temperature measurement for the graph.

The cardiac cycle duration was 650 ms. The ablation was performed at a RF power of 20W during 60s with an irrigation flow of the catheter of 30 mL/min. The measured impedance of the tissue before the ablation was around 150 Ω resulting in 125 Ω after compensation of the offset. The temperature at the hottest pixel near the catheter increased progressively to reach 20°C at the end of heating (Figure IV.15). After the RF was turned off the tissues cooled because of perfusion and heat conduction.

4. Discussion

These results were in good agreement with results reported in a previous study (D. Senneville et al. 2012). The higher SNR, 50 compared to 20 can be explained by the use of a 32 channels cardiac. This gain of 2.5 in SNR should allow us to theoretically improve the spatial resolution keeping the same precision as the other study to reach a pixel size of 1.9 x 1.9 x 4.4 for example. Slice tracking could improve the management of the respiratory and in plane motion correction too (de Senneville et al. 2004 Rieke et al. 2007 Salomir et al. 2012).

6. Catheter antenna

1. Introduction

The aim of the study was to explore the possibility of using the catheter tip as MR antenna to increase the spatial resolution of the temperature images by increasing the SNR. Indeed, in catheter thermal ablation, the area of desired heating is usually ranged between 0 (at the contact) and 1 cm (septum thickness). This area is very small compared to usual field of view in thoracic MRI. Moreover, the sensitivity of the conventional loop antenna used to image decreases in $1/R^2$ with R the distance from the antenna. Despite the antenna is placed on the chest, the distance to the centre of the heart remains about 7 cm. Concept of loopless antenna was widely used and may allow a better detection of the signal, (Sathyanarayana & Bottomley 2009). For a loopless antenna, the sensitivity decreases in $1/R$ and the catheter antenna is directly at the contact of the heart. The maximal required distance between the antenna and the heart, in order to map the temperature is 1 cm (septum thickness). If we considered the same noise for both antenna and the same maximal sensitivity then, the SNR for the same sequence and the same spatial resolution would be increased by a factor of 49 when using the catheter tip as a MR antenna. This gain of SNR can be used to increase the spatial resolution by dividing the pixel size by 2.6 in each direction and the thickness by 7. The maximal spatial resolution used in experiments was $2.6 \times 2.6 \times 6 \text{ cm}^3$ (see § IV.5.2). The gain in SNR could theoretically provide a sub millimetre spatial resolution with the same precision on temperature images. High spatial resolution has been already described in the literature by using catheter antennas with a spatial resolution of 0.08 mm at an update rate of 2 images per second (Sathyanarayana & Bottomley 2009). The following study presents preliminary result, showing the feasibility to acquire images with a RF ablation catheter.

2. Material and method

The study was realized at 4.7 T on a Bruker scanner installed at the laboratory centre de Résonance Magnétique des Systèmes Biologiques (RMSB).

The sequence was a 3D GE flash with the following parameters: TE/TR = 2.2ms/500ms, 30 x 30 mm FOV, 48 x 48 acquisition matrix, 15° flip angle, 5 mm thickness positioned perpendicular to the wire.

Antenna was composed by a wire surrounded by a copper braid. In order to insulate the external cable, a thermo-sheathing was added to avoid short cut. For imaging purpose, the antenna was immersed in water.

3. Result

The Figure IV.16 shows the image obtained for this configuration. The signal of the water was detected in an area of 1cm diameter centred in the wire with a spatial resolution of 0.625 mm.

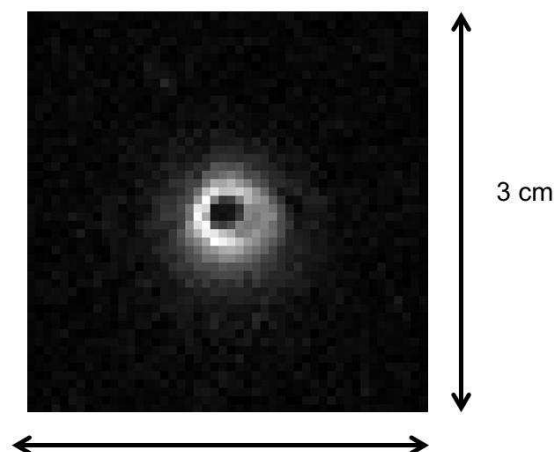


Figure IV.16: Catheter as a wire antenna. Modulus image obtained by a flash 3D sequence in a water tube at the tip of the wire. The orientation was perpendicular to the wire.

The excitation and the detection were ensured by the wire.

4. Discussion

This experiment showed the feasibility of imaging at submillimetric spatial resolution. However, a number of improvements need to be performed. The first improvement could be to separate excitation and detection to avoid overheating of the catheter and thus increase the safety of the patient. The excitation could be realised by the Q-body and the loopless antenna used only for the detection.

7. Discussion

This chapter showed the feasibility of catheter ablation in vivo on a sheep heart under MR thermometry and study the MR thermometry precision on the heart. Constraints of MR thermometry were studied. Sequences were acquired under breath-hold (respiratory motion) and prospective gating (heart contraction). Breath-hold limited sequence duration; slice tracking would certainly extend the possibility of real time monitoring but this functionality was not available at the moment of the experiment. The resulting temperature precision appeared better than those reported in the literature on the heart (D. Senneville et al. 2012) but lower than those expected by the simulation. $T2^*$ (40.2ms) value and SNR were estimated in the heart and used to estimate the temperature precision (0.8°C). The difference between simulation and measurement of the temperature precision could be explained by the absence of motion correction. Moreover, the higher SNR of the images, in our experiments, could be used to ensure a high temperature precision or to provide a better spatial resolution (1.9 x 1.9 x 4.4). Nevertheless, this improvement resulted in a moderate increase of spatial resolution

insufficient for precise mapping of temperature during RFA. Wire catheter antenna provided GE images with submillimetric spatial resolution (0.625mm) in an area of 1 cm around the wire, which should be useful for estimating lesion shape via a monitoring of the temperature during catheter ablation. However, MR thermometry with external coils remains a useful tool to visualise eventual collateral heating during the procedure. Further investigations could be developed to improve MR thermometry with catheter and external coils for the monitoring of thermal catheter ablation like in plane motion correction (D. Senneville et al. 2012). Moreover, the development of dedicated instrumentation, using embedded sensor in the catheter, may also improve 3D slice tracking for real time MR thermometry of cardiac RFA.

8. References

- Anderson, L. J. et al., 2001. Cardiovascular T2-star (T2*) magnetic resonance for the early diagnosis of myocardial iron overload. *European Heart Journal*, 22(23), p.2171-2179.
- Blanc, J.J. et al., 2008. Consensus document on antithrombotic therapy in the setting of electrophysiological procedures. *Europace*, 10(5), p.513-527.
- Chavhan, G.B. et al., 2009. Principles, Techniques, and Applications of T2*-based MR Imaging and Its Special Applications. *Radiographics*, 29(5), p.1433-1449.
- Haines, D., 2004. Biophysics of Ablation: *Journal of Cardiovascular Electrophysiology*, 15, p.S2–S11.
- Haines, D.E., 2011. The Yin and Yang of Convective Cooling in Radiofrequency Catheter Ablation. *Circulation: Arrhythmia and Electrophysiology*, 4(6), p.794-795.

- Heinrichs, U. et al., 2009. Myocardial T2* mapping free of distortion using susceptibility-weighted fast spin-echo imaging: A feasibility study at 1.5 T and 3.0 T. *Magnetic Resonance in Medicine*, 62(3), p.822-828.
- Holbrook, A.B. et al., 2010. Real-time MR thermometry for monitoring HIFU ablations of the liver. *Magnetic Resonance in Medicine*, 63(2), p.365-373.
- Ishihara, Y. et al., 1995. A precise and fast temperature mapping using water proton chemical shift. *Magnetic Resonance in Medicine*, 34(6), p.814–823.
- Kolandaivelu, A. et al., 2010. Noninvasive Assessment of Tissue Heating During Cardiac Radiofrequency Ablation Using MRI ThermographyClinical Perspective. *Circulation: Arrhythmia and Electrophysiology*, 3(5), p.521-529.
- Nakagawa, H. et al., 1995. Comparison of In Vivo Tissue Temperature Profile and Lesion Geometry for Radiofrequency Ablation With a Saline-Irrigated Electrode Versus Temperature Control in a Canine Thigh Muscle Preparation. *Circulation*, 91(8), p.2264-2273.
- Ou, P. et al., 2012. Cardiac T2* measurements in patients with iron overload: a comparison of imaging parameters and analysis techniques. *Magnetic Resonance Imaging*, 30(5), p.641-648.
- Positano, V. et al., 2007. Standardized T2* map of normal human heart in vivo to correct T2* segmental artefacts. *NMR in Biomedicine*, 20(6), p.578–590.
- Quesson, B. et al., 2011. Real-time volumetric MRI thermometry of focused ultrasound ablation in vivo: a feasibility study in pig liver and kidney. *NMR in Biomedicine*, 24(2), p.145-153.
- Quesson, B., de Zwart, J.A. & Moonen, C.T.W., 2000. Magnetic resonance temperature imaging for guidance of thermotherapy. *Journal of Magnetic Resonance Imaging*, 12(4), p.525-533.

- Ramazzotti, A. et al., 2009. Multicenter validation of the magnetic resonance t_2^* technique for segmental and global quantification of myocardial iron. *Journal of Magnetic Resonance Imaging*, 30(1), p.62–68.
- Reeder, S.B. et al., 1998. In Vivo Measurement of T_2^* and Field Inhomogeneity Maps in the Human Heart at 1.5 T. *Magnetic resonance in medicine : official journal of the Society of Magnetic Resonance in Medicine / Society of Magnetic Resonance in Medicine*, 39(6), p.988-998.
- Rieke, V. & Butts Pauly, K., 2008. MR thermometry. *Journal of Magnetic Resonance Imaging: JMRI*, 27(2), p.376-390.
- Rieke, V. et al., 2007. Referenceless MR Thermometry for Monitoring Thermal Ablation in the Prostate. *IEEE Transactions on Medical Imaging*, 26(6), p.813 -821.
- Roujol, S. et al., 2010. Real-time MR-thermometry and dosimetry for interventional guidance on abdominal organs. *Magnetic Resonance in Medicine*, 63(4), p.1080–1087.
- Salomir, R., 2001. Local hyperthermia by MRI-guided focused ultrasound.
- Salomir, R. et al., 2012. Reference-Free PRFS MR-Thermometry Using Near-Harmonic 2-D Reconstruction of the Background Phase. *IEEE Transactions on Medical Imaging*, 31(2), p.287 -301.
- Sathyanarayana, S. & Bottomley, P.A., 2009. MRI endoscopy using intrinsically localized probes. *Medical Physics*, 36(3), p.908.
- Scaglione, M. et al., 2012. Impact of ablation catheter irrigation design on silent cerebral embolism after radiofrequency catheter ablation of atrial fibrillation: results from a pilot study. *Journal of cardiovascular electrophysiology*, 23(8), p.801-805.

- Senneville, D. et al., 2012. Feasibility of fast MR-thermometry during cardiac radiofrequency ablation. *NMR in Biomedicine*, 25(4), p.556-562.
- Senneville, D. et al., 2004. Atlas-based motion correction for online MR temperature mapping. In *2004 International Conference on Image Processing, 2004. ICIP '04.* 2004 International Conference on Image Processing, 2004. ICIP '04. p. 2571 - 2574 Vol. 4.
- Seror, O. et al., 2008. Real time monitoring of radiofrequency ablation based on MR thermometry and thermal dose in the pig liver in vivo. *European Radiology*, 18(2), p.408-416.
- Skrumeda, L.L. & Mehra, R., 1998. Comparison of Standard and Irrigated Radiofrequency Ablation in the Canine Ventricle. *Journal of Cardiovascular Electrophysiology*, 9(11), p.1196–1205.
- Tsuchiya, T. et al., 2007. Atrial Fibrillation Ablation with Esophageal Cooling with a Cooled Water-Irrigated Intraesophageal Balloon: A Pilot Study. *Journal of Cardiovascular Electrophysiology*, 18(2), p.145–150.
- Westwood, M. et al., 2003. A single breath-hold multiecho T2* cardiovascular magnetic resonance technique for diagnosis of myocardial iron overload. *Journal of Magnetic Resonance Imaging*, 18(1), p.33–39.

V. GENERAL CONCLUSIONS

The presented studies show new methods for MR guided thermal ablation by using non invasive (HIFU) and mini-invasive (RFA) thermotherapies. Different methods have been developed to increase the safety and the efficiency of thermal ablations.

The first part investigated a Bubble Enhanced Heating (BEH) to increase lesion size *ex vivo* and *in vivo* in pig liver. The threshold of BEH was determined *ex vivo* by using MR-ARFI and corresponded to approximately 50 μm of displacement amplitude. When exploiting the BEH effect, the maximum temperature rise was increased by 50% and the size in the transverse direction by almost a factor 2. The origin of this phenomenon was not investigated in this study. Acoustic cavitation (Inaba et al. 2011 Hynynen 1991) or boiling (Khokhlova et al. 2009) may generate such effect. However, the measurement of displacement at the focal point by MR-ARFI, in light of the study of Sapin de Brosse (Sapin-de Brosses et al. 2011) indicate that burst pulse effect should not be attributed to irreversible thermal effect, since the amplitude of displacement increased after BEH. To better investigate the precise physical phenomenon (Khokhlova et al. 2009), a transducer operating in receive mode may be included in the experimental setup. However, independently of the effect, BEH remains dependent on a threshold acoustic intensity. In order to apply this method to other organs which require large ablation volume, tissues specific thresholds of BEH need to be determined. In this perspective, MR-ARFI sequence may be optimized to reduce the acquisition time for *in vivo* measurement, by using parallel imaging techniques or rapid gradient echo based acquisitions (Vincent Auboiroux et al. s.d.) with alternated bipolar gradients or spin echo-echo planar imaging (Kaye et al. 2011) with shifting of the readout echo. Another interesting potential application of BEH is the exploitation of the persistence in time of the effect., since more sophisticated sonications could be planed where a number of

selected locations may be pre-defined and targeted with short burst sonications at sufficient acoustic power in order to delineate the desired outer limit of the sonication field (shielding effect, (Zderic et al. 2008)).

Nevertheless, HIFU sonications performed in organs located in the rib cage remains challenging because of bones that constituted the subject of the second part of this manuscript.

The method presented in the manuscript to avoid excessive heating near the ribs was a binarized apodization law that consisted in switching off transducer elements located in front of rib. An update of this law appeared necessary for electronic deflection of 7 mm right or left to the natural focal point. In this part, experiments were only performed in gel, and *ex vivo* and *in vivo* experiments could not be investigated. In order to update the binarized apodization law very quickly, it could be interesting, prior HIFU sonication, to mesh the possible area of electronic deflection every millimetres and to calculate the binarized apodization law for each focal point location. This technique could be further improved by development of automatic or semi automatic algorithm for the segmentation of bones avoiding potential bias due to manually segmentation. Moreover, the criterion for deactivating an element (set to 50% coverage of a transducer element) may also be optimized in order to maximize the acoustic intensity at the focus. Slice tracking and real time beam steering could be combined with such approach, using for example the navigator. This practical solution opens possibilities to investigate the technical feasibility of cardiac thermal ablation by using non invasive HIFU sonications. However, management of the complex cardiac structure and motion of the heart (respiratory motion and cardiac contraction) is mandatory, which was initiated in the last chapter of the manuscript for real time monitoring of .

The monitoring of RFA in the heart by using MR thermometry was study in the last part of the manuscript. In order to estimate the temperature precision, the $T2^*$ was investigated and found equal to 40.2 ms. A better estimation could be achieved by using displaced U-FLARE

because the range of sampling time values for the $T2^*$ exponential decrease could be increased. The estimated temperature precision was lower than those experimentally measured on temperature images on the heart. This difference could be explained by the lack of in plane motion correction (B. D. de Senneville et al. 2004) (Rieke et al. 2007) (R. Salomir et al. 2012). Feasibility of RFA performed in a sheep heart under MR thermometry was also performed and was in good agreement previous study (D. Senneville et al. 2012). New features will be implemented such as slice tracking to allow continuous temperature monitoring in free breathing. Moreover, the higher SNR observed on magnitude images in our experiments may be exploited to improve the spatial resolution of MR-temperature images. Therefore, MR thermometry could also provide access to quantitative estimate of potential catheter heating induced by absorption of the RF pulse emitted by the body MR antenna (Haines 2011) of the scanner. Moreover, development of the catheter instrumentation will be required (through collaborations with several companies) to exploit all the capabilities of the different sensors embedded on the catheter tip (temperature, electrical activity, ablation, tracking coils,...). Furthermore, the use of the catheter as an MR antenna can be used to increase the spatial resolution by exploiting the increase in SNR as compared to conventional body surface coils. Under these conditions, heating protocols may be optimized for the different locations of the heart, taking into account the tissue thickness, local perfusion, electrical viability, flow rate in the cavities, etc... Such developments may also open perspective for the development of dedicated algorithms for automatic control of energy delivery based on real-time feedback of energy delivery from quantitative and rapid MR temperature images.

Each new technological and methodological development will have to integrate patient safety and will be guided toward translation into the clinics through the IHU-LIRYC institute.

- Auboiroux, Vincent et al., ARFI prepared MRgHIFU in liver: Simultaneous mapping of ARFI displacement and temperature elevation, using a fast GRE EPI sequence. *Magnetic Resonance in Medicine*.
- Haines, D.E., 2011. The Yin and Yang of Convective Cooling in Radiofrequency Catheter Ablation. *Circulation: Arrhythmia and Electrophysiology*, 4(6), p.794-795.
- Hynynen, K., 1991. The threshold for thermally significant cavitation in dog's thigh muscle in vivo. *Ultrasound in Medicine & Biology*, 17(2), p.157-169.
- Inaba, Y. et al., 2011. Ultrasonic coagulation of large tissue region by generating multiple cavitation clouds in direction perpendicular to ultrasound propagation. *Japanese Journal of Applied Physics*, 50(07HF13).
- Kaye, E.A., Chen, J. & Pauly, Kim Butts, 2011. Rapid MR-ARFI method for focal spot localization during focused ultrasound therapy. *Magnetic Resonance in Medicine*, 65(3), p.738-743.
- Khokhlova, T.D. et al., 2009. Magnetic resonance imaging of boiling induced by high intensity focused ultrasound. *Journal of the Acoustical Society of America*, 125(4), p.2420-2431.
- Rieke, V. et al., 2007. Referenceless MR Thermometry for Monitoring Thermal Ablation in the Prostate. *IEEE Transactions on Medical Imaging*, 26(6), p.813 -821.
- Salomir, R. et al., 2012. Reference-Free PRFS MR-Thermometry Using Near-Harmonic 2-D Reconstruction of the Background Phase. *IEEE Transactions on Medical Imaging*, 31(2), p.287 -301.

Sapin-de Brosse, E., Pernot, M. & Tanter, M., 2011. The link between tissue elasticity and thermal dose in vivo. *Physics in Medicine and Biology*, 56(24), p.7755-7765.

de Senneville, B.D. et al., 2004. Atlas-based motion correction for online MR temperature mapping. In *2004 International Conference on Image Processing, 2004. ICIP '04.* 2004 International Conference on Image Processing, 2004. ICIP '04. p. 2571 - 2574 Vol. 4.

Senneville, D. et al., 2012. Feasibility of fast MR-thermometry during cardiac radiofrequency ablation. *NMR in Biomedicine*, 25(4), p.556-562.

Zderic, V. et al., 2008. Prevention of post-focal thermal damage by formation of bubbles at the focus during high intensity focused ultrasound therapy. *Medical Physics*, 35(10), p.4292.

VI. PUBLICATIONS LIST

Scientific conferences

Delphine Elbes, Benjamin Robert, Max O. Köhler, Mickaël Tanter, Chrit Moonen, and Bruno Quesson, **Detection and exploitation of acoustic cavitation for enhancement of MR guided High Intensity Focused Ultrasound heating in ex vivo liver**, 19th annual meeting of International Society for Magnetic Resonance in Medicine, Montréal, Canada, 2011

Delphine Elbes, Benjamin Robert, Max O. Köhler, Mickaël Tanter, and Bruno Quesson, **Detection and exploitation of acoustic cavitation for enhancement of MR guided High Intensity Focused Ultrasound heating in ex vivo liver**, Symposium of International Society for Therapeutic Ultrasound, New York, USA, 2011

Aurélien Emilien, Jenny Benois-Pineau, Delphine Elbes, Bruno Quesson.

Adaptive rejection of outliers for robust motion compensation in cardiac MR thermometry, International Symposium on Biomedical Imaging (ISBI), 2013, in submission

Publications

Preclinical Study of in vivo MR-guided Enhanced Ultrasound Heating in Pig Liver

Delphine Elbes, MD Quentin Denost, Christophe Laurent, Hervé Trillaud, Anne Rullier, Bruno Quesson in submission *Ultrasound in Medicine and Biology*

Magnetic resonance imaging for the exploitation of bubble enhanced heating by High Intensity Focused Ultrasound. A feasibility study in ex vivo liver.

Delphine Elbes, Quentin Denost, Benjamin Robert, Max O. Köhler, Michaël Tanter, Quesson Bruno in submission